Doctoral thesis

Engineering of a bacteriophytochrome-derived reversibly switchable fluorescent protein for the application in super-resolution microscopy in the near-infrared window

Dissertation
to acquire the doctoral degree in mathematics and natural sciences
'Doctor of Philosophy'
at the Georg-August-Universität Göttingen

in the doctoral degree program "Biomolecules- Structure,function and dynamics' at the Göttingen Graduate School for Neurosciences, Biophysics and Molecular Biosciences

submitted by

Daniel Stumpf

from Heppenheim

Göttingen, 2022

Thesis committee:

Prof. Dr. Stefan Jakobs (1st Referee)
High Resolution microscopy of the cell
Clinic of Neurology, University Medical Center, Göttingen
Mitochondrial Structure and Dynamics Group
Department of Nanobiophotonics
Max-Planck-Institute for Multidisciplinary Sciences

Prof. Dr. Dirk Schwarzer (2nd referee)
Department of Dynamics at Surfaces
Max-Planck-Institute for Multidisciplinary Sciences

Prof. Dr. Jörg Enderlein
Third Institute of Physics (Biophysics)
Georg August University Göttingen

Members of the examination board:

apl. Prof. Dr. Alexander Egner
Department of Optical Nanoscopy
Institute for Nanobiophotonics Göttingen e.V.

Dr. Melina Schuh
Department of Meiosis
Max Planck Institute for Multidisciplinary Sciences

Dr. Sonja Lorenz
Ubiquitin Signaling Specificity
Max Planck Institute for Multidisciplinary Sciences

Date of the oral examination: June 9th, 2022

Abstract

The developments of fluorescence microscopy techniques has advanced our understanding of biological systems on a cellular level. In recent years, several super-resolution microscopy techniques overcame the diffraction barrier thereby allowing unprecedented insights in the subcellular structures down to the molecular level. Reversible saturable optical linear fluorescence transition (RESOLFT) microscopy, as one of these techniques, allows for the formation of super-resolved images by utilizing low light intensities in the kW/cm^2 range, which makes it a suitable tool for live cell super-resolution imaging. The RESOLFT concept relies on-switching fluorophores between a fluorescent on- and non-fluorescent off-state. To date, most RESOLFT applications depend on reversibly switchable fluorescent proteins (RSFP), which are excited and switched by light in the visible region of the electromagnetic spectrum.

In order to transfer RESOLFT to the near-infrared (NIR) region of the electromagnetic spectrum, which exhibits reduced scattering and phototoxicity, a new class of RSFPs is required. Bacteriophytochromes as NIR-photoreceptors in bacteria act as suitable templates for engineering a NIR-RSFP.

In this work, the monomeric bacteriophytochrome-derived PhotostablE Nir rEversibly switchable fLuOrescent ProteEin (PENELOPE) was engineered using site-directed and random mutagenesis. PENELOPE exhibits a strong photostability, fast off-switching and allows RESOLFT imaging in the NIR window for the first time. NIR-RESOLFT microscopy was performed by using a single wavelength. This was enabled by harnessing the remarkable ability of PENELOPE to thermally relax to the on-state within milliseconds after off-switching. This allowed the substitution of the conventional on-switching step with a thermal relaxation step, which additionally reduced the applied light doses during imaging. Furthermore, RESOLFT microscopy was successfully performed in fixed mammalian cells using a genetically encoded RSFP for the first time. The implementation of a time-saving pixel hop scan approach in conjunction with a novel proposed switching state model for PENELOPE, ushers PENELOPE into low light dose NIR super-resolution microscopy.

Table of Contents

1 Introduction

1.1 Fluorescence Microscopy

The exploration of biological environments on the intracellular level is fundamentally linked to the development of the first compound microscope in the late 16th century by Dutch father and son team Hans Martens and Zacharias Janssen [1]. With the publication of his book "Micrographia" in 1667, English natural scientist Robert Hooke demonstrated the powerful improvements made to existing lens systems allowing magnification improvements of up to 270x [2]. Improving the quality of crucial microscope compounds allowed visualization of subcellular structures in brightfield microscopy. Inherent limitations of brightfield microscopy like low contrast of features gave rise for the development of a supplementary class of microscopes circumventing these limitations in the beginning of the 20th century. This new class of microscopes relied on another light-driven principle: fluorescence.
Fluorescence is a subtype of photoluminescence, which is described as a quantum mechanical process becoming visible by optical radiation during the relaxation of a molecule from an excited (higher energy) S1 state to its (lower energy) S0 ground state. Molecules exhibiting the potential to fluoresce are called fluorophores [3]. Fluorophores absorb and can be excited to the S1 state by defined regions of the electromagnetic spectrum (Figure 1.1).

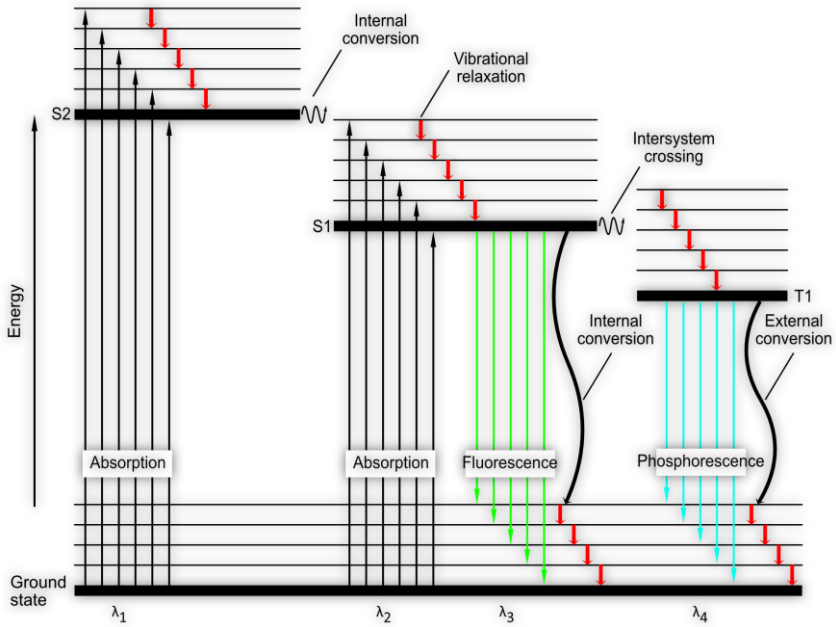

Figure 1.1: Jablonski diagram of energy state transitions in fluorescent molecules. *Absorption of a photon with λ1 or λ2 transfers a molecule from the ground state S0 into higher energetic states S1 or S2, respectively. Internal conversion allows electron transition from higher order energetic states into lower order energetic states without the emission of a photon. Direct S1 to S0 electron transition results in fluorescence with the wavelength λ3. Non-radiative processes starting in the S1 state include internal conversion to the S0 ground state as well as intersystem crossing into a long-lived triplet state T1. Electron transition from T1 to S0 occurs as a radiative process via phosphorescence with a wavelength λ4 as well as a non-radiative process via external conversion. Modified after [4] .*

The required energy difference to transfer an electron within the fluorophore from S0 to S1 is equal to the energy of the absorbed photon [5] (see Eq. 1).

$$E_p = E_1 - E_0 \qquad (Eq. 1)$$

Emitted photons exhibit a red-shifted wavelength in comparison to the excitation photon. This is due to the vibrational loss of energy within the S1 state, which is referred to as Stokes shift [6] . The average elapsed time between the excitation of the fluorophore and the emission of a photon is referred to as excited state fluorescence lifetime (τ) and follows an exponential decay (see Eq. 2).

$$I(t) = I_0 e^{-t/\tau} \qquad (Eq. 2)$$

The ratio of emitted photons to absorbed photons of the same fluorophore is known as the fluorescence quantum yield (ϕ) (see Eq. 3).

$$\phi = \frac{\#\text{emitted photons}}{\#\text{absorbed photons}} \qquad (Eq. 3)$$

Multiplying the fluorescence quantum yield with the fluorophore-specific extinction coefficient (ε), which is described as the capacity for light absorption at a specific wavelength, results in the molecular brightness (MB) (see Eq. 4).

$$MB = \varepsilon \cdot \phi \qquad (Eq. 4)$$

Fluorescence microscopy overcomes the contrast limit of brightfield microscopy by only detecting signals from cellular structures labeled with fluorescent molecules. In contrast to brightfield microscopy, fluorescence microscopy requires additional optical elements, light sources and detection systems allowing for sample excitation, light separation and photon detection. Harnessing the wavelength shift of the Stokes fluorescence, only emitted photons are detected whereas excitation photons are blocked by optical filters [7] . In epifluorescence widefield microscopy, planes above and below the focal z-plane are also illuminated by out-of-focus light and contribute photons to the final image. Depending on the labeling density, this impedes the formation of a sharp image exhibiting detailed structures (Figure 1.2a).

This contribution of out-of-focus light was reduced with the invention of the confocal fluorescence microscope. Using a high magnifying and high aperture objective lens, the excitation spot can be reduced to approximately half the size of the wavelength in the lateral plane. Out-of-focus fluorescence is prevented from entering the detector by installing a pinhole in front of the detector [8]. In contrary to the usually utilized camera systems in widefield fluorescence microscopy, confocal fluorescence microscopes detect photons via

photomultiplier tubes (PMT) or avalanche photodiodes (APD) to reconstruct the image pixel by pixel [9] (Figure 1.2b).

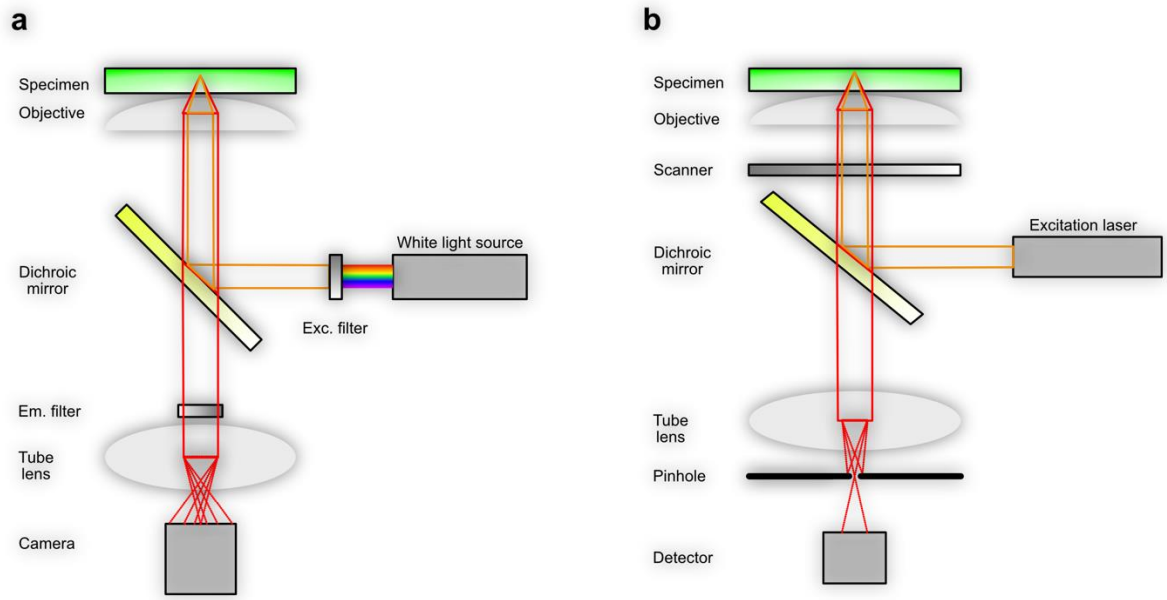

Figure 1.2: Schematic representation of widefield and confocal fluorescence microscopy. *(A) Widefield fluorescence microscopy. A white light source emits in the ultraviolet (UV) and visible (VIS) spectrum and is targeted on an excitation filter (Exc. Filter). The filter separates the required wavelengths, which are reflected from a dichroic mirror into the objective and focused into the specimen. The fluorescence from all sample layers is collected by the objective, passed through the dichroic mirror and detected on the camera. (B) Confocal laser scanning microscopy. A coherent single wavelength excitation laser is directed on different locations within the sample via a scanning device. The fluorescence from single layers is focused onto the detector while out-of-focus light is blocked by the pinhole.*

Challenges regarding weak contrast can arise from insufficient labeling, poor dye photophysics and sample autofluorescence. While insufficient labeling and dye photophysics can be mostly overcome by chemically modifying the respective label, sample autofluorescence is an inherent problem of the cellular environment. Autofluorescence can originate from a variety of molecules exhibiting different moieties and localizations. The spectral range of autofluorescence emitting molecules covers UV-light excitable coenzyme Nicotinamide adenine dinucleotide phosphate NAD(P)H to the green-to-red light-excitable oxygen-transport metalloprotein hemoglobin in red blood cells [10], [11] (Figure 1.3).

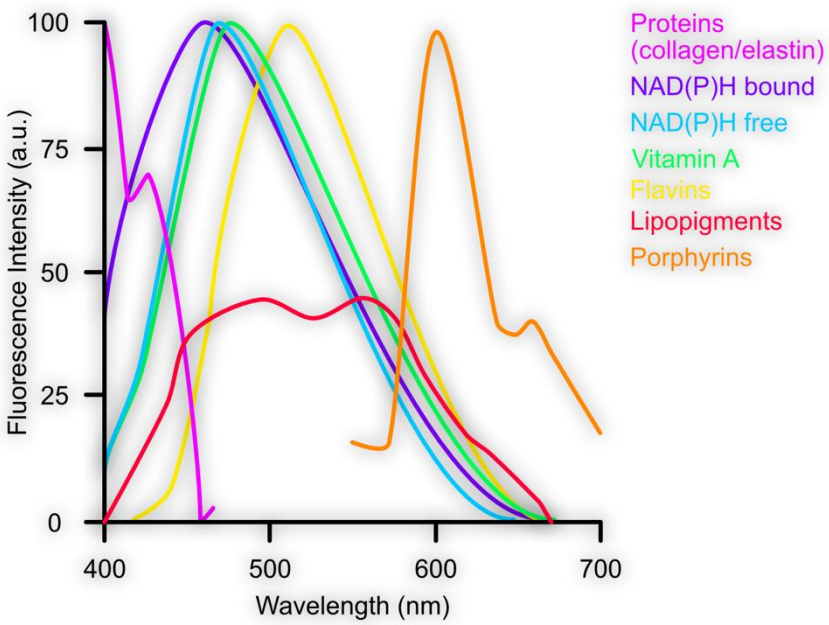

Figure 1.3: Fluorescence signal contribution of autofluorescing molecules in biological specimen. *Spectral profiles were detected in solution from purified tissues and subsequently normalized to the maximum emission peak. Modified after ([12]).*

The initial technical developments of microscopes in general, which led to the optimization of these imaging systems mainly focused on improving optical elements. For instance, on objectives and lenses in order to achieve a smaller focal spot of light. Over time, optical systems achieved the theoretical minimum size of the focal spot of light which was first described by Ernst Abbe in 1873 [13] and amounts for the lateral spot size (see Eq. 5.1) to:

$$r_{lat} = \frac{\lambda}{2n \cdot \sin \alpha} \qquad (Eq. 5.1)$$

and for the axial spot size (see Eq. 5.2) to:

$$r_{ax} = \frac{\lambda}{n \cdot \sin^2 \alpha} \qquad (Eq. 5.2)$$

with λ as the wavelength of light, n the refractive index of the immersion medium, and α the half-angle of the aperture of the objective lens.

These sizes describe the extent of the focal spot of a light microscope, which is referred to as point spread function (PSF). The PSF describes the image formation of an idealized point-like object by the optical system in three dimensions. In accordance with equations 5.1 and 5.2, this PSF represents a point-like signal in the lateral plane but an elliptical shape in the axial plane [14].
The product of optical parameters n and sin(α) is also known as the numerical aperture (NA), which is a dimensionless factor and correlates with the ability of the objective to collect light

and its obtainable resolution. In conjunction with the NA, the excitation wavelength defines the size of the PSF [15] (Figure 1.4a,b).

Following up on the emitted fluorescence of an excited sub-resolution point-like emitter in the lateral plane, the ring-shaped maximum intensity peak is enclosed by further ring-shaped intensity maxima and minima. This pattern of intensity maxima and minima is referred to as Airy pattern whereas the distance between the intensity peaks of the central sphere and first ring is known as the Airy disc (Figure 1.4c). The size of the Airy disc is limited by the inherent diffraction of light, called the diffraction limit. The Airy disc size is a prerequisite for the determination whether two objects can be resolved [16]. The minimum distance between two light sources that may be resolved into distinct objects is generally referred to as the Rayleigh criterion [15] (Figure 1.4d).

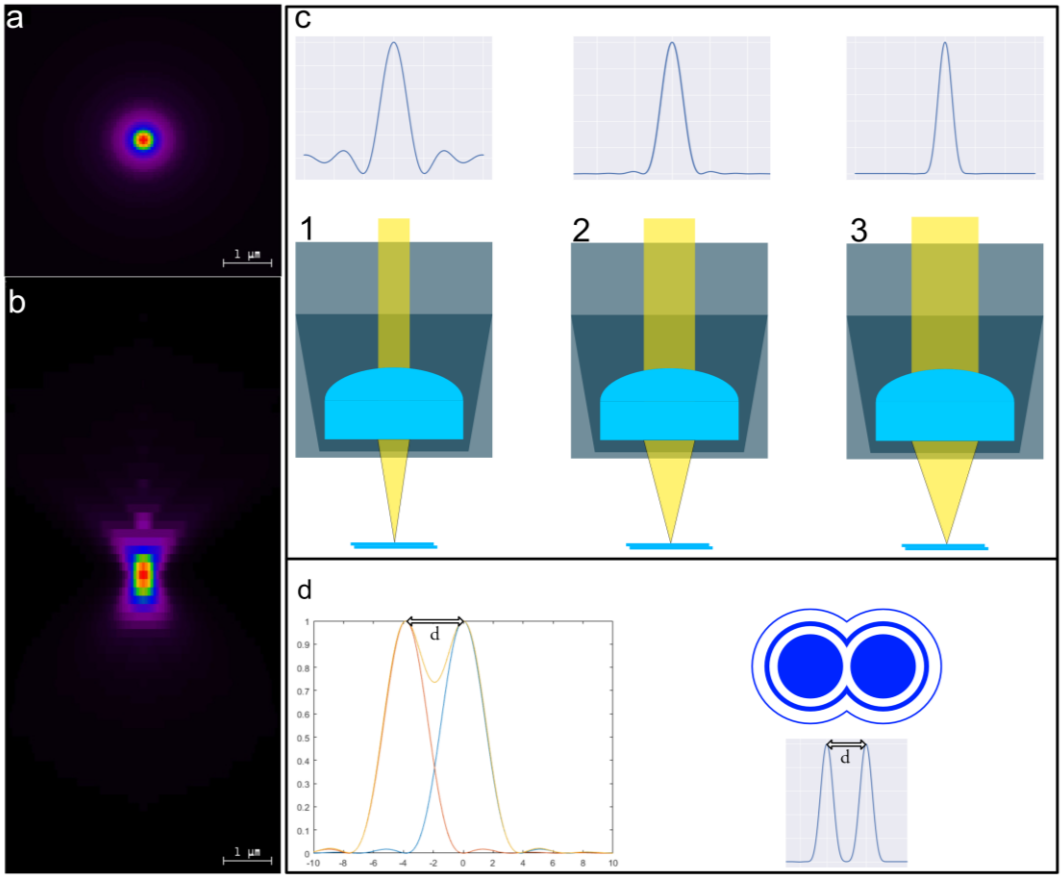

Figure 1.4: Principles of resolution determination. *(a,b) Simulated two-dimensional PSF maximum intensity projections for a confocal microscope with a high NA objective in xy and xz, respectively. The simulations were created with the Nyquist rate and PSF calculator of Scientific Volume imaging (Netherlands). (c) Influence of NA on Airy disc formation. With increasing NA and light cone angle from depictions 1 to 3, the Airy disc size decreases (d) Depiction of two hypothetical Airy discs in close proximity as two- and three-dimensional sketch (right) as well as plotted against the intensity (left). The Rayleigh criterion is fulfilled as the zeroth order maxima do not overlap and can be resolved as separate entities. Illustration adapted from [17].*

According to the Rayleigh criterion, two objects are just resolvable when the distance d between the Airy disc maximum intensity of object A overlaps with the first minimum of the Airy pattern of object B. For the lateral plane d_{lat} (see Eq. 6.1), this is described with:

$$d_{lat} = 0.61 \cdot \frac{\lambda}{\mathrm{NA}} \qquad (Eq. 6.1)$$

and for the axial plane (see Eq. 6.2) when the distance (d_{ax}) is:

$$d_{ax} = \frac{2\mathrm{n} \cdot \lambda}{\mathrm{NA}^2} \qquad (Eq. 6.2)$$

For a 1.4 NA oil objective and an emission wavelength of 488 nm, the achievable lateral PSF resolution would be ~160 nm and the minimum distance between two discernible structures according to the Rayleigh criterion would be ~200 nm.

Transferring the conceptional restrains of PSF size and obtainable resolution to the application in cell microscopy, it emerges that many cellular structures and interaction sites are impossible to observe in detail due to their size below the diffraction limit.

1.2 Super-resolution microscopy - Microscopy below the diffraction limit

More than 100 years after the resolution limit was described by Ernst Abbe for the first time, initial theoretical frameworks in order to circumvent the resolution limit were proposed.
One of the first systems which achieved resolution improvements within the lateral dimension was the 4Pi-microscope. By utilizing two opposing objective lenses, laser light is focused onto a common focal area and is superimposed. The resulting constructive interference of the laser light reduces the PSF size along the optic axis. Assuming an ideal equal distance of the objectives from the focal point, emitted fluorescence can also be collected simultaneously, thereby creating again interference, and be collected on the detector [18] .

In the mid 90s of the 20th century, Structured Illumination Microscopy (SIM) showed a lateral resolution improvement by a factor of two, which was expanded to the axial resolution in the year 2008. Harnessing the increasing availability of computing power, SIM relies in principle on transferring the widefield recordings of serial images recorded with transposed structured illumination patterns into high frequency information, in the form of the Fourier Transform, which can ultimately be restored in the final image [19] . The previously mentioned increase in computing power, spatial illumination and post-processing for image reconstruction were accelerated to allow video framerates, with less than 250 ms delay between measurement and reconstructed image display [20].

Despite shifting the diffraction limit, 4Pi-microscopy and SIM, as two very prominent members of the super-resolution microscopy family, are conceptionally unable to achieve resolutions below ~100nm [21]. The adaptations for these methods were conducted on the arrangement of the optical elements or the illumination and image processing. In contrast, super-resolution microscopy methods, which can, in theory, achieve molecular resolution harness discernible states of emitting molecules. Super-resolution microscopy methods can be divided into two groups: Coordinate-stochastic microscopy and coordinate-targeted microscopy.

1.2.1 Coordinate-stochastic microscopy

Coordinate-stochastic super-resolution microscopy, also referred to as single molecule localization microscopy (SMLM) relies on the temporally resolved detection of single, spatially separated fluorescent emitters. Illumination occurs on a widefield microscopy setup and emitted photons are detected with a camera. In conventional widefield fluorescence microscopy, constitutively fluorescent fluorophores are used in order to receive a sufficient number of photons per activation event. In most labeled cellular structures, the resulting PSF simultaneously excites adjacent fluorophores and creates the diffraction limited image [22]. In prominent coordinate-targeted methods as STochastic Optical Reconstruction Microscopy (STORM) [23], Direct Stochastic Optical Reconstruction Microscopy (dSTORM) [24], (Fluorescence) Photo-Activation Localization Microscopy ((f)PALM) [25] and Ground State Depletion microscopy followed by Individual Molecule return (GSDIM) [26], fluorophores are prohibited to constitutively fluoresce either by a reversible chemical reaction that interferes with fluorescence emission [23] or enabling stochastic fluorescence emission of photochromatic fluorescent proteins [27]. Allowing only a subset of fluorophores to emit photons for a single image formation increases the probability for detecting emission events of single fluorophores. This single image formation process is repeated many times in order allow all fluorescent emitters to contribute photons [23]. These diffraction-limited events can then be mathematically fitted to determine the intensity maximum, which corresponds to the position of the fluorophore (Figure 1.5). The localization precision (see Eq. 7) ultimately depends on the Full Width Half Maximum (FWHM) of the PSF and the number of collected photons (N) [28].

$$\Delta_{loc} \propto \frac{\mathrm{FWHM}}{\sqrt{\mathrm{N}}} \qquad (Eq.7)$$

For this reason, coordinate-stochastic methods are in theory able to resolve molecular resolutions, provided that the maximum number of photons per molecule, referred to as photon budget, is sufficient[29] [30]. Furthermore, the localization precision is not equivalent to the optical resolution due to setup and sample dependent parameters like drift and labeling density [31], which ultimately allows for a lateral resolution between 10-50 nm under experimental conditions [32] . In contrast to the probe-based widefield approach to

achieve super-resolution in coordinate-stochastic microscopy, a hardware-based approach is utilized in coordinate-targeted microscopy.

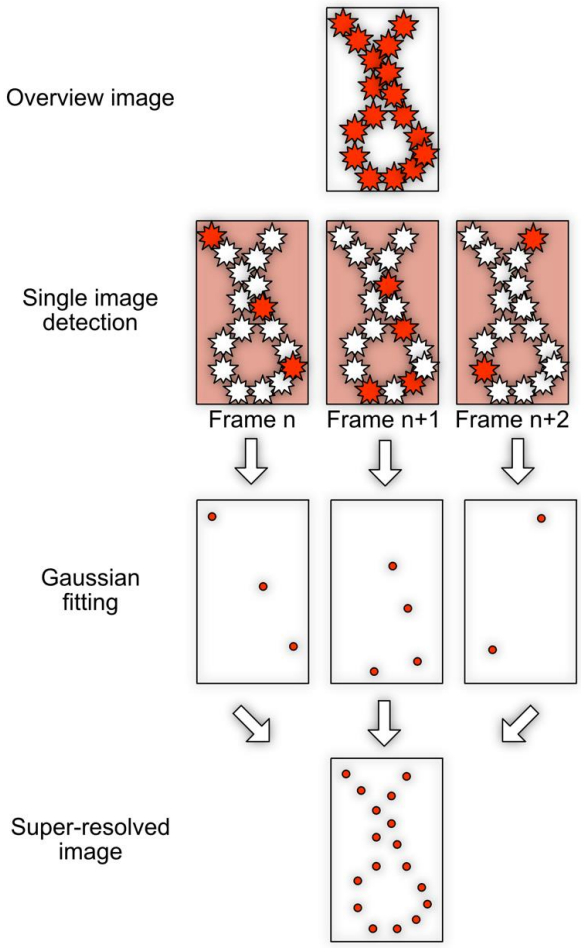

Figure 1.5: Principle of coordinate-stochastic super-resolution imaging. *Upper image: Diffraction limited overview image of labelled structure. Second row: Multiple images are recorded, while only a subset of fluorophores is emitting during the formation of a single image. Third row: A Gaussian function fit is applied and the centroid position is calculated. Repeated emission of the fluorophore allows the combination of centroid positions and yields in a super-resolved emission spot. Fourth row: Combining centroid positions of all detected images results in a super-resoled image of the target structure.*

1.2.2 Coordinate-targeted microscopy

Coordinate-targeted microscopy also relies on discernible fluorescent states of fluorophores but does not require single spatially and temporarily distinct emitters. Coordinate-targeted methods achieve the fluorophore transition from active to inactive fluorescent emitters by applying spatial light patterns to a fluorophore ensemble [33]. The overall concept that describes the necessary state transitions of the fluorophores and the respective microscope family is termed REversible Saturable OpticaL Fluorescence Transitions (RESOLFT) microscopy [34]. Within this family, different imaging modes are usually termed based on the fluorescence transition mechanism that they rely on.

In its simplest implementation, super-resolved images are ultimately generated by superimposing two focal spots, one of them with a central intensity zero and another with a central intensity maximum. In most applications, the central intensity minimum pattern is resembled by torus shaped laser light, often referred to as "doughnut", whereas the central intensity maximum pattern follows a Gaussian shaped laser beam. The doughnut's purpose is the suppression of fluorescence emission in the ensemble periphery while allowing the center fluorophores to emit photons via spontaneous fluorescence emission when excited with the Gaussian laser [35]. Assuming a simple fluorescence state model, in which a fluorescent state *A* can be transitioned into a non-fluorescent state *B* and vice versa (Figure 1.6a), the intensity-dependent state transition rate constant k_{AB} (see Eq. 8) allows to calculate the light intensity required to transition from one state into the other [36].

$$k_{AB} = \sigma \cdot I \qquad (Eq. 8)$$

with σ describing the transition cross section and I the intensity of the light which drives the transition.

A light intensity *I* allowing for equal population of the states *A* and *B* is referred to as saturation intensity I_{sat}. When $I >> I_{sat}$, illuminated molecules are predominantly transitioned into the non-fluorescent state *B*. The fluorescent state transition is a non-linear process, which enables the generation of a sub-diffraction sized spot comprising of molecules predominantly residing in the fluorescent state with its maximum distribution towards the center [37] (Figure 1.6b).

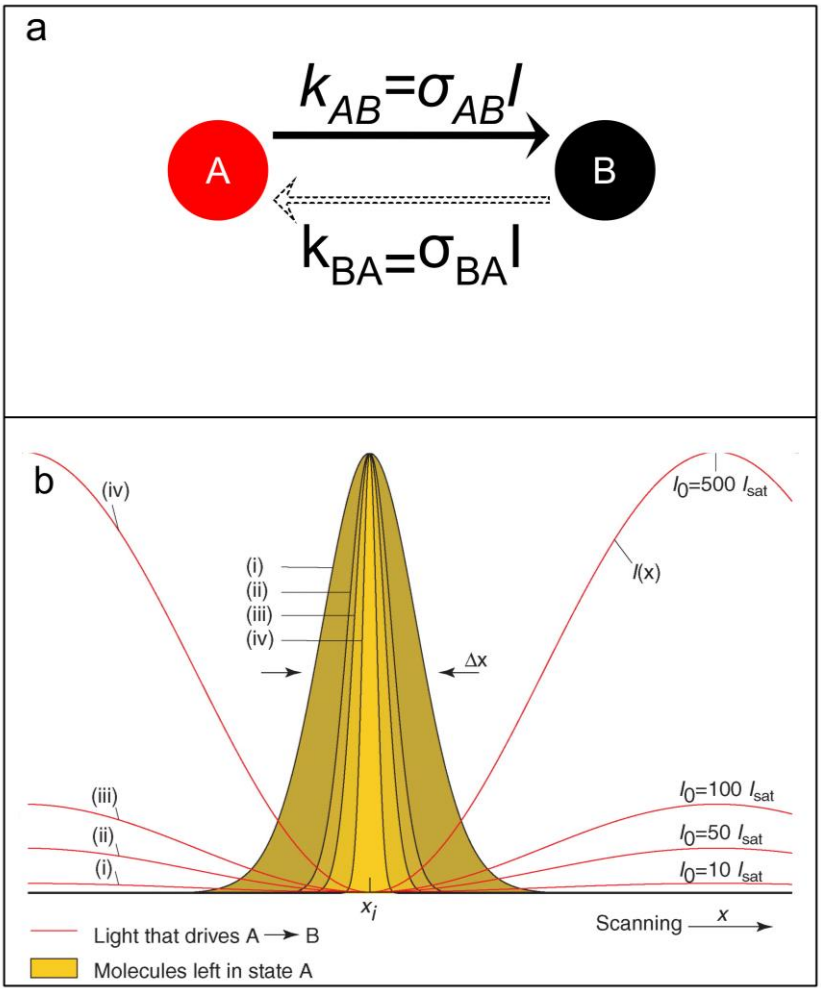

Figure 1.6: Principle of coordinate-targeted super-resolution imaging. *(a) Light-driven two-state transition model of a fluorophore. State A represents. The rate constants k_{AB}/k_{BA} are dependent on the light intensity I and the absorption cross section σ. (b) One-dimensional depiction of the influence of the light intensity $I>>I_{sat}$ on the fluorophores remaining in the fluorescent state. Panel adapted from [38].*

This concept extends the previously introduced diffraction limit by Ernst Abbe with a term allowing a decreased effective excitation area (see Eq. 9):

$$\Delta d = \frac{\lambda}{2n \cdot \sin\alpha \sqrt{1 + \frac{I}{I_{sat}}}} \qquad (Eq. 9)$$

In theory, the minimal resolvable distance Δd is unlimited and does only depend on the ratio ζ of applied doughnut light intensity to the saturation intensity of the state transition (see Eq. 10):

$$\zeta = I/I_{sat} \qquad (Eq. 10)$$

The wide range of accessible fluorophores allows for several ways to harness the transition between discernible fluorescent and non-fluorescent states.

Recently, the conceptual strengths of coordinate-stochastic and coordinate-targeted super-resolution microscopy techniques have been merged in the development of MINimal photon FLUXes (MINFLUX) microscopy [39]. In this method, a single stochastically activated emitter is targeted by a doughnut-shaped excitation laser with a central zero-intensity area. Triangulation of the laser on the position of the emitter results in varying fluorescence traces depending on the distance between the central zero intensity area and the fluorescence emitter. These traces in conjunction with the information on the intensity distribution of the excitation laser are used to calculate the exact position of the emitter and allow molecular resolution of down to 1nm [40, 41]. Methods which solely rely on the coordinate-targeted super-resolution microscopy method will be presented in the following section.

1.2.3 Stimulated Emission Depletion microscopy - STED

In STimulated Emission Depletion (STED) microscopy, fluorescence emission suppression is accomplished by transferring excited electrons from the S1 state into the S0 state via stimulated emission. In this process, light of a specific wavelength, which is red shifted compared to the spontaneous fluorescence emission photons, interacts with the excited molecule in the S1 state and will allow the return of the molecule to the ground state by emitting a photon with the same energy as the interacting light. Since the stimulated emission photons (referred to as the STED laser light) are focused to a doughnut distribution, periphery fluorescence is effectively depleted and does not contribute to the fluorescence photon detection [42] (Figure 1.7). For most dyes, the stimulated emission rate is small due to their inefficient stimulated emission cross-section [43].

For this reason, in conjunction with the short excited state lifetime, high intensities (~MW/cm^2 - GW/cm^2) of the STED laser are required to allow stimulated emission rates above the spontaneous fluorescence emission. These high intensities may in turn entail photobleaching of the chromophore [44] along with photodamage of live specimen [45].

1.2.4 RESOLFT microscopy with photoswitchable fluorescent proteins and dyes

In RESOLFT microscopy with Reversibly Switchable Fluorescent Proteins (RSFPs) or photoswitchable dyes, discernible long-lived fluorescent and non-fluorescent states of the respective fluorophores allow utilizing lower laser intensities (~kW/cm^2) of the doughnut-shaped laser [46]. An alternative requirement for harnessing low laser intensities is a high switching cross-section of the different fluorescent states of the respective fluorophore.

A detailed introduction into the required fluorophore characteristics necessary for application in RESOLFT microscopy as well as mechanistic insights into light-switchable chromophore photophysics can be found in section 1.3.4.
RESOLFT microscopy has been established as a point-scanning as well as a parallelized approach. In contrast to STED microscopy, in point-scanning RESOLFT microscopy illumination steps are applied gradually and often require a previous transition of the fluorophore ensemble to a fluorescent state with a Gaussian shaped activation laser. The subsequent illumination step involves the doughnut-shaped laser light to switch fluorophores in the periphery off and only allowing fluorophores near the intensity minimum to reside in the activated fluorescent state. A Gaussian shaped readout laser beam then excites the residing active fluorophores and a super-resolved image is generated [47] (Figure 1.7). In parallelized RESOLFT, an off-switching pattern can be created by intersecting two orthogonal and incoherent standing waves (ISC). For $I >> I_{sat}$, a circular symmetry of the minimum around the zero is achieved, resulting in a doughnut-shaped pattern. In 2013, Chmyrov et al. showed that over a large field of view of 120 µm x 100 µm up to 116,000 'intensity zeros' can be generated in parallel. The imaging sequence involves a uniform on-switching illumination, followed by the off-switching ISC pattern and a uniform readout illumination. After every cycle, the readout emission is detected on a camera. This sequence is repeated until every position has been probed. The final RESOLFT image is generated by keeping only the signal close to the 'intensity zeros' in the recorded stack of camera images [48]. Additional methods to achieve parallelized off-switch patterns include the utilization of multi-foci-pattern creating microlens arrays or binary linear phase gratings [49, 50].

The application possibilities for RESOLFT microscopy are mainly centered around living cells due to the low light intensities which should prevent the sample from photodamage. In order to maintain this low-interfering environment, genetically encoded fluorescent proteins exhibiting distinctive fluorescent and non-fluorescent states appear as ideal markers.

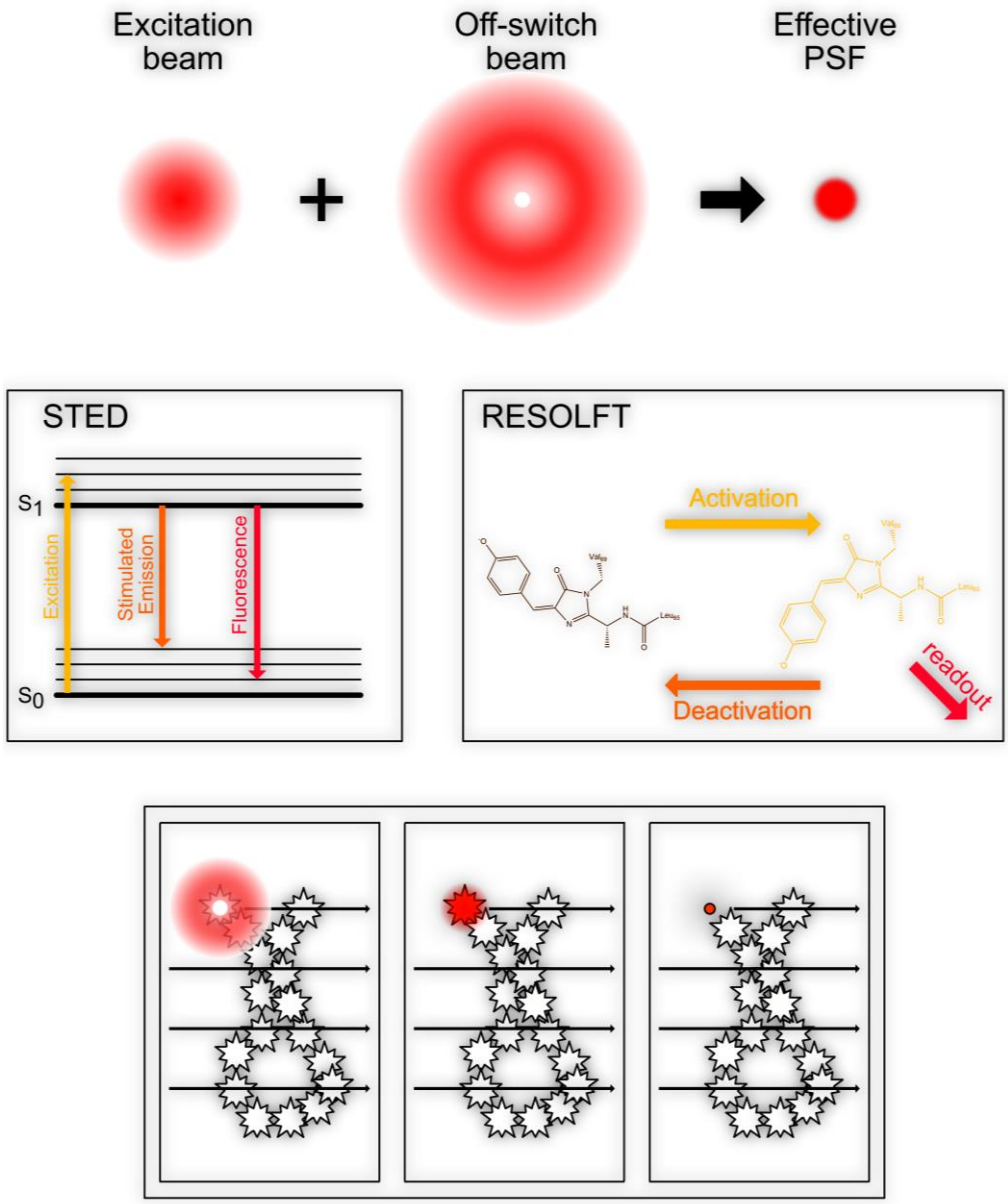

Figure 1.7: Principles of STED microscopy and RESOLFT microscopy with RSFPs. *The superposition of a Gaussian-shaped excitation beam with a doughnut-shaped deexcitation beam results in a smaller effective PSF. In STED, excitation and doughnut STED beam are applied onto the sample at the same time due to short fluorescence lifetimes of the fluorophores. In RESOLFT, the excitation beam follows upon the deexcitation doughnut-shaped beam. With reversibly switchable fluorescent proteins, a Gaussian-shaped on-switching laser can transfer molecules back into the on-state. In both cases, the sample is scanned and a super-resolved image is generated.*

1.3 Fluorescent proteins

In order to study cellular structures in live cells in a fluorescence microscope, low-interfering tagging of proteins of interest is a key requirement for fluorescent markers.
Target structures labeled with antibodies or organic dyes can require previous treatment with permeabilization reagents or fixatives, limiting the application for live cell experiments. Live cell protein tags such as SNAP-tag or live cell dyes such as MitoTracker for instance, bear the potential for background fluorescence or unspecific binding to cell membranes via hydrophobic interactions [51] [52].
With the discovery of the Green Fluorescent Protein (GFP) from *Aequorea Victoria* in 1962 by *Shimomura et al.* [53], the observation of genetically encoded fluorescent proteins (FPs) fused to target proteins enables easy application of live cell fluorescence microscopy [54].

1.3.1 The Green Fluorescent Protein - GFP

Sequence analysis and quantitative protein purification revealed a 238 amino acid long sequence and a total molecular weight of ~27 kDa for GFP. Features of the protein quartery structure were independently solved by x-ray crystallography and subsequently published in 1996 and revealed a β-barrel consisting of eleven β-sheets with a centrally located α-helix harboring the chromophore (Figure 1.8) [55, 56]. The chromophore is autocatalytically formed by a serine-tyrosine-glycine tripeptide at amino acid positions 65 to 67. The formation of the covalently bound chromophore 4-(p-hydroxybenzylidene)imidazolidin-5-one (HBI) requires molecular oxygen in order to catalyze the posttranslational cyclization of the chromophore to allow for fluorescence [57].

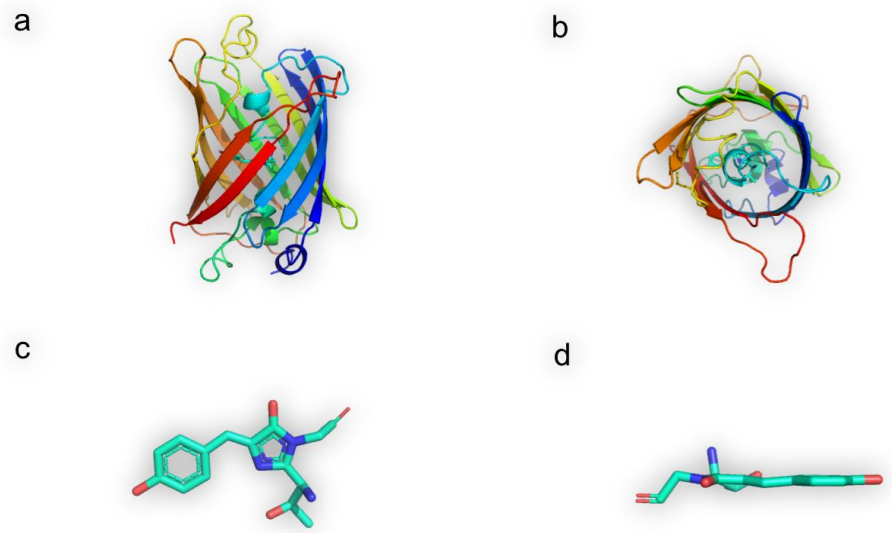

Figure 1.8: Crystal structure of GFP. *a) and b) show the side and top view of GFP in cartoon representation, respectively. The chromophore is depicted in the stick representation and can be seen in the center of the barrel structure. c) and d) show the top and side view of the GFP chromophore respectively, including the hydroxyphenyl ring which is linked via a methine bridge to the imidazilinone ring. [PDB ID: 1EMA [55]]*

1.3.2 GFP-like fluorescent proteins

Following the discovery of wild-type GFP, further FP variants were reported. These fluorescent proteins did not solely emerge by molecular engineering of wild-type GFP but also originated from a range of diverse host organisms such as coral anemones [58] or stone corals [59]. These FPs share, despite sequence dissimilarities, fundamental structural similarities. They include the chromophore enclosing β-barrel along with the autocatalytic formation of the chromophore. Due to these similarities, these proteins are grouped as GFP-like fluorescent protein. With these new players, the visible (VIS) range up to the low regimes of the near-infrared (NIR) range of the electromagnetic spectrum was able to be covered by fluorescent proteins [60], [61]. Increasing efforts in structure determination in conjunction with protein engineering also allowed for further FP parameters to be addressed. These parameters comprise requirements beneficial for general fluorescence microscopy such as brightness [62], but also requirements for specialized applications within fluorescence microscopy. One such specialized application is RESOLFT microscopy with RSFPs.

1.3.3 Reversibly Switchable Fluorescent Proteins - RSFPs

FPs which can be transitioned between two distinct forms by the absorption of light in which both forms exhibit different absorption spectra are referred to as photochromic FPs [63]. Fluorescent proteins harboring chromophores which allow this transition to be reversible are referred to as reversibly switchable fluorescent proteins (RSFPs). In general, RSFPs display a fluorescent state (on-state) and a non-fluorescent state (off-state) [64].
One of the first thoroughly documented photoswitchable fluorescent proteins was asFP595 from the sea anemone *Anemonia sulcata* in 2003. asFP595 could be switched from its off-state, with an absorption maximum of 568nm, to its on-state with green light while simultaneously emitting fluorescence. The reversible transition towards the off-state occurs eventually by thermal relaxation but can be also triggered by irradiation with blue light [65]. Counteracting these benign optical properties was the tetrameric behavior of asFP595, which ultimately limited its use as a genetic marker for fluorescence microscopy.

The first monomeric RSFP Dronpa, which wild-type predecessor 22G was extracted from the stony coral *Echinophyllia sp. SC22*, was published only one year after asFP595 [59]. Dronpa did not only show monomeric behavior but also showed adequate brightness. In comparison to asFP595, Dronpa emits fluorescence while switched to the off-state under blue light irradiation. Reversible photoswitching into the on-state occurs under UV-light irradiation. RSFPs displaying the switching of Dronpa are termed negative switching RSFPs whereas RSFPs exhibiting the switching of asFP595 are termed positive switching RSFPs [66].

1.3.4 RSFP chromophore photophysics and mechanics

Despite high sequence similarities between RSFPs and their constitutively fluorescent predecessors, the chromophore's composition, spatial positioning and movement capacity show diverging behaviors compared to chromophores of constitutively fluorescent proteins [67]. X-ray crystallography data of RSFPs in their respective on- and off-states suggests conformational changes of the chromophore orientation in conjunction with chromophore protonation/deprotonation events after light illumination [68]. For the majority of negative switching RSFPs, the on-state resembles a cis-conformation of the chromophore, which isomerizes into a trans-conformation when being off-switched [69] (Figure 1.9). This isomerization occurs downstream the methine bridge and allows the p-hydroxyphenyl ring to rotate (Figure 1.9). Because this isomerization is a sterically demanding process, the volume-conserving "hula-twist" in which the double bond and the adjacent single bond rotate at the same time to reduce volume changes during the photoreaction has been proposed [65, 70]. This phenomenon was observed in protein crystals, exhibiting a more confined and rigid environment than in solution. For this reason, ring rotation as well as "hula-twist" are both potential mechanistic pathways. However, both mechanisms require the translocation of close-proximity amino acids in the chromophore environment.

Besides conformational changes, many characterized RSFPs display changes of the protonation-state when switched between a fluorescent on-state and a non-fluorescent off-state [71]. The temporal dependence of conformational changes and protonation/deprotonation is still a matter of debate and might vary between different RSFPs. In most negative switching RSFPs, the chromophore is protonated in the off-state which leads to a blue-shift of the absorbance peak resulting in an effective fluorescence decrease at the previous absorption wavelength. Molecular Dynamics simulations propose an increase in chromophore torsion, which leads to a reduced fluorescence quantum yield [65] [72].

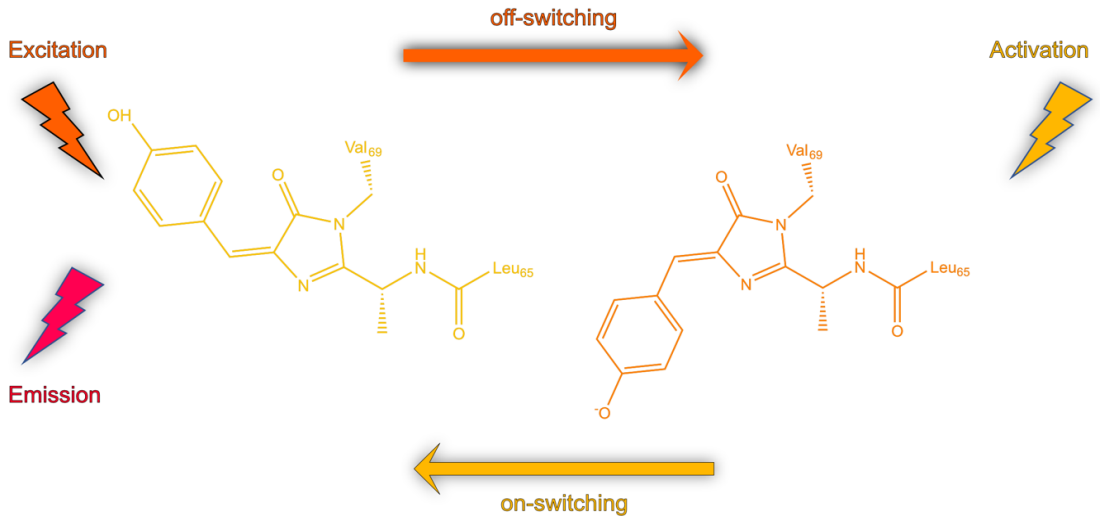

Figure 1.9: Fluorescent state transition of a negative switching GFP-based RSFP. *The excitation wavelength leads to the red-shifted emission of light and induces in a competing process the isomerization from the chromophores' fluorescent cis configuration (yellow) to the non-fluorescent trans-configuration (orange). Illumination with light of a corresponding activation wavelength reverts this transition and therefore allows for repeated emission and state transitions.*

These mechanistic pathways are the driving forces required for general RSFP photoswitching. For the application in super-resolution microscopy, especially RESOLFT microscopy, further RSFP characteristics are of interest in order to allow for improved spatial and temporal resolution.

1.3.5 RSFPs in super-resolution microscopy

In order to perform super-resolution microscopy with RSFPs, one basic biochemical parameter, which is crucial for conventional fluorescence microscopy, is the oligomerization tendency. As previously mentioned, monomeric behavior with only low oligomerization tendencies is required to allow for low aggregation with target and surrounding proteins, conserving natural cellular structures [73].

The image formation process is ultimately limited by five key RSFP-specific photophysical parameters. These parameters will be introduced based on negatively switching RSFPs in an ensemble. The fluorescence brightness of RSFPs refers to the number of detected photons as a function of applied laser intensity and number of emitting RSFPs. For negative switching RSFPs, the fluorescence brightness decreases over time under continuous illumination until it reaches the minimum residual fluorescence. The underlying rate constant for this transfer from the fluorescent on-state to the non-fluorescent off-state is in general dependent on the applied laser intensity. In RESOLFT microscopy, RSFPs require to be switched back into the fluorescent on-state after readout. This on-switching rate constant is also laser intensity dependent and requires for negative switching RSFPs a blue-shifted wavelength compared to the off-switching wavelength. The process of transferring RSFPs into the on- and off-states with the respective laser wavelength is

repeated several times for a single frame for each molecule while recording a full image. Over time, a fraction of the ensemble proteins is photobleached and cannot be transferred to the on-state again, thereby contributing to a decrease of the ratio between fluorescence intensity and minimum residual fluorescence. In addition, expression levels, RSFP maturation time, oligomerization tendencies, pH stability, spectral characteristics and blinking are further crucial parameters that need to be taken into account for the evaluation of RSFPs for RESOLFT microscopy [46, 74].

GFP-like FPs exhibit remarkable features allowing for their use in conventional fluorescence microscopy as well as super-resolution microscopy. However, the previously mentioned overall structural similarity of the chromophore limits the use of GFP-like FPs to the VIS spectral region. The beneficial red-shifted NIR spectral region, demonstrating reduced sample autofluorescence, scattering and absorption of hemoglobin and oxyhemoglobin (Figure 1.10), cannot be reached using GFP-like FPs [75]. In addition, NIR light is favored towards UV/VIS light as it exhibits a lower photon energy. A lower photon energy causes a decreased probability for potential phototoxic effects and is therefore beneficial for long-term live cell imaging [76]. Naturally occurring NIR-light sensors, called phytochromes, bear the potential for engineering conventional FPs as well as RSFPs which can be excited in the NIR region.

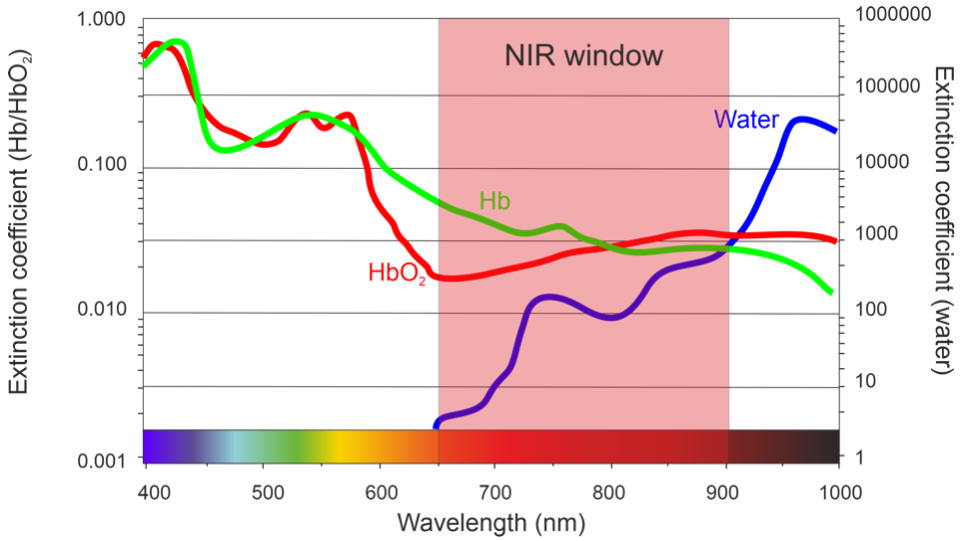

Figure 1.10: Extinction coefficients of hemoglobin (Hb), oxyhemoglobin (HbO_2) and water in the visible and NIR spectral regime. *Modified after [77].*

1.4 Phytochromes

Phytochromes occur in plants, fungi and bacteria and serve as red/far-red-light sensing photoreceptors. Red/far-red-light sensing takes place after the incorporation of an external chromophore. In plants, phytochromes are controlling diverse components of plant development such as seed germination, chlorophyll synthesis and flowering timing [78]. In bacteria, phytochromes are referred to as bacteriophytochromes and act as photo-sensing intracellular signal transducers, which amongst others affect virulence functions, iron metabolism, and transition from a sessile to a free-swimming motile lifestyle [79].

Phytochromes share a common structure, which is comprised of the N-terminal photosensory core module (PCM) and the C-terminal regulatory region. For bacteriophytochromes the PCM contains a PAS (Per-ARNT-Sim), GAF (cGMP phosphodiesterase/adenylate cyclase/FhlA) and PHY (phytochrome specific) domain (Figure 1.11), whereas the regulatory domain includes a histidine kinase [80]. Within the PCM, the PAS and GAF domain are furthermore termed the chromophore-binding domain (CBD). The number and order of these domains within the PCM and C-terminal regulatory region varies in different hosts and can be expanded by response regulators or N-terminal extensions [81]. As mentioned in the previous paragraph, phytochromes require an external chromophore for red/far-red light sensing. The chromophore, a linear tetrapyrrole, is covalently bound by a cysteine in the PCM and is embedded inside the GAF domain on all occasions [82]. Phytochromes of bacteria, cyanobacteria and plants bind the linearized tetrapyrroles BV (BV), phycocyanobilin (PCB) or phytochromobilin (PΦB), respectively [83, 84],[85]. Bacterial Phytochromes are also termed bacteriophytochromes.

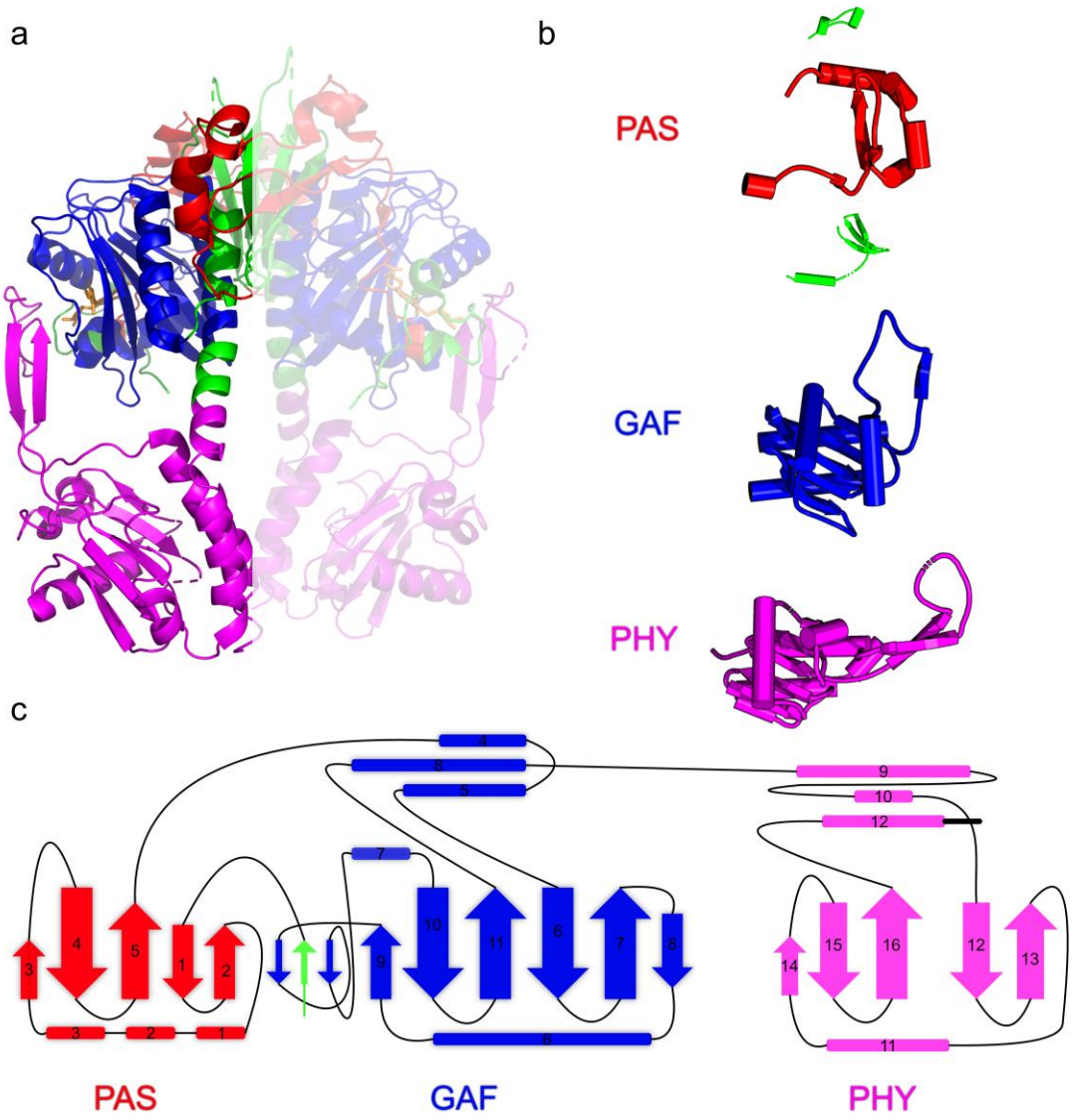

Figure 1.11: Structural compartments of a bacteriophytochrome.*(a) Crystal structure of the dimeric photosensory core module of Deinococcus Radiodurans in its dark form [PDB ID: 4O0P[86]]. (b) Cartoon depiction of single domains, including the N-terminal domain in green, the PAS domain in red, GAF domain in blue and the PHY domain in magenta. Helices are displayed as cyclinders. (c) Schematic representation of the secondary structure of a bacteriophytochrome, following the color code used in (b).*

Linear tetrapyrroles are a product of porphyrin degradation. In plants, the cyclic progenitor of PΦB is chlorophyll, whereas for bacterial BV it is the iron-ion coordinating heme complex [84]. Since 90% of the total iron in bacterial cells is not associated with heme, degradation processes like those occurring in eukaryotes are hypothesized [87]. The degradation to BV involves the oxidative cleavage of heme, which is catalyzed by the enzyme heme oxygenase. In mammals, the conversion of heme to BV, iron and CO by heme oxygenase requires five electrons provided by the reductase system and three molecules of oxygen [88]. The resulting BV is then further reduced by the enzyme BV reductase into Bilirubin (BR), which can ultimately be conjugated to glucuronic acid and excreted through bile and urine [89]. The tendency for membrane-permeability of BV is still a matter of debate [90] [91], which raises the question whether uptake of exogenous BV or excretion of excessive intracellular BV in mammalian cells is mediated by transporter proteins. Among

the initially presented phytochrome classes, bacteriophytochromes show the highest affinity for BV incorporation. In conjunction with their comparatively small size and initial weak fluorescence, this phytochrome class exhibits a system advantage for NIR-FP development over other phytochromes [92] and will therefore be further analyzed in the following section.

1.4.1 Bacteriophytochromes

The covalent thioether binding of BV to the bacteriophytochrome via a cysteine residue in the PAS domain forms the red/far-red light sensing holoprotein [93]. This PAS-domain consists of a five-stranded antiparallel β-sheet which is interconnected to a six-stranded β -sheet of the GAF-domain, coordinating chromophore positioning. With three additional α-helices, the GAF-domain is forming a pocket around the chromophore, resulting in the chromophore binding domain (CBD) [94, 95]. The CBD contains the highly conserved DIP motif, which directly interacts with the chromophore (Figure 1.12a). The DIP motif is comprised of the amino acids Aspartate, Isoleucine and Proline at positions 207-209. Hydrophobic interactions between I208 with propionate side chains of the BV C-ring as well as P209 with propionate side chains of the B-ring stabilize the chromophore [95]. High-resolution crystal structures revealed a distanced proximity of the D-ring to the chromophore binding pocket comprising amino acids and therefore allows for increased spatial flexibility of the D-ring [85]. Furthermore, the CBD features a figure-of-eight knot, which corresponds to the threading of the N-terminal end through a loop formed by two C-terminal α-helices of the GAF-domain (Figure 1.12b,c,d) [96]. The function of this ubiquitously found structural element in bacteriophytochromes has not been determined yet. Theories involve an increased probability of correct folding into the native state and minimized energy losses upon chromophore isomerization during photoconversion [97] as well as stabilized positioning of the cysteine residue for efficient chromophore binding [98]. In solution and crystals, the CBD is prone to form dimers which affect the photocycle by lowering the energy barrier for dark reversion [99].

Adjacent to the CBD and part of the Photosensory Core Module (PCM) is the PHY domain. The PHY domain is linked to the GAF domain by an α-helix, which forms a cavity in the dimer center of certain bacteriophytochromes [100]. The PHY domain harbors the so-called Phy-tongue. Depending on the conformational state of the bacteriophytochrome, the PHY-tongue can adapt a β-sheet conformation in the Pr-state and an α -helical secondary structure in the Pfr-state. This, in length variable, structure interacts with the previously introduced DIP motif of the CBD [101]. In *Deinococcus radiodurans* bacteriophytochrome (DrBphP), a salt-bridge is formed between R466 and D207 in the Pr-state, stabilizing the β-sheet conformation [102]. Red-light illumination breaks this salt bridge, releases the tongue and allows for the interaction between D207 and S468 in the Pfr-state [100]. The Pfr-state is ultimately stabilized by F469 by preventing thermal relaxation [103]. This refolding mechanism is crucial for the Pr-Pfr photocycle in wildtype bacteriophytochromes.

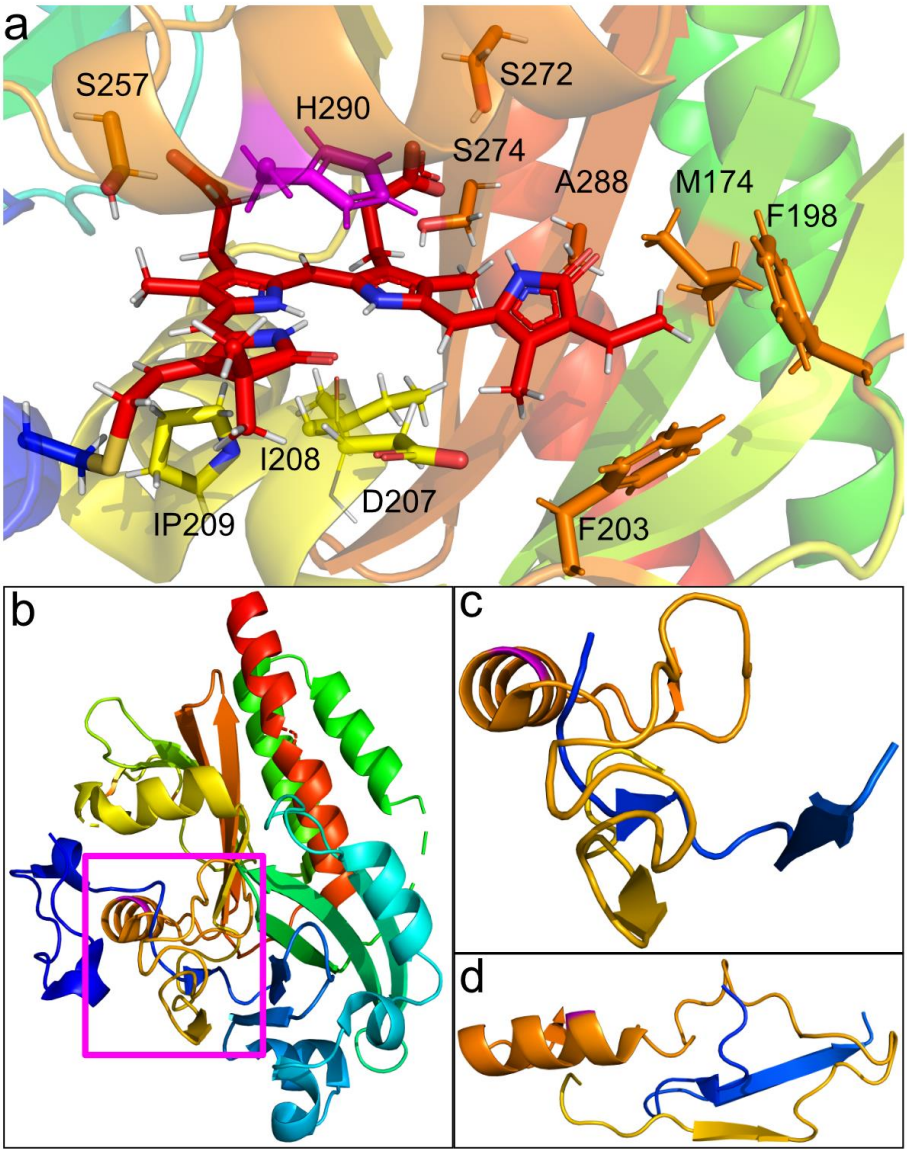

Figure 1.12: Chromophore binding pocket and figure-of-eight knot in the Deinococcus radiodurans CBD. *(a) Amino acids in the immediate surrounding of the chromophore. Depicted stick-style amino acids include general close-proximity amino acids of the GAF domain (orange) and the DIP motif (yellow). (b) The monomeric Deinococcus radiodurans CBD with the figure-of-eight knot highlighted in the magenta-colored square. (c) Front view of the figure-of-eight knot. (d) Side view of the figure-of-eight knot. [PDB ID: 3S7O [104]]*

1.4.2 Pfr/Pr photocycle in bacteriophytochromes

The bacteriophytochrome holoprotein displays a complex photocycle with two spectroscopically discernible metastable states. Canonical bacteriophytochromes can be converted between a red light-absorbing Pr-state and a far-red light- absorbing Pfr-state. For canonical bacteriophytochromes representing the majority of known bacteriophytochromes, the Pr-state is the energetically favored state [105]. Bacteriophytochromes exhibiting the Pfr-state as the resting state are referred to as bathy bacteriophytochromes [106]. The interconversion between these two states can be targeted by red/far-red light or thermal relaxation in the dark.

Pr and Pfr-states are represented by the BV D-ring configurations 5Zsyn, 10Zsyn, 15Zanti (ZZZssa) and 5Zsyn, 10Zsyn, 15Eanti (ZZEssa), respectively [107] [108]. The Z-to-E and E-to-Z isomerization is caused by the rotation of the C15–C16 methine-bridge between ring C and D [109].

Besides the metastable Pr and Pfr-state, bacteriophytochromes pass multiple intermediate states in order to transfer to the respective opposing state (Figure 1.13). The definition of a distinct intermediate state is not trivial; however, the consensus suggests the presence of short-lived (µs) photoexcited Lumi-states and long-lived (ms) protonation/deprotonation-driven as well as conformational changes-driven meta-states [110]. As depicted in Figure 1.13, the excited states Lumi-R and Lumi-F are formed within a picosecond range. It is suggested that Lumi-R exhibits a more long-lived formation time of compared to Lumi-F with [111, 112]. Both states attribute for the Z-to-E isomerization and E-to-Z isomerization of the BV D-ring, respectively [113]. The switching quantum yield for Pr-Lumi-R/Pfr-Lumi-F accounts for less than 15% [114]. In a *Stigmatella aurantiaca* bacteriophytochrome, a decay channel from Lumi-R to Pr with a switching quantum yield of 20-30% has been observed, which is likely to correspond to a back flip of the BV D-ring [115]. UV-VIS and Resonance Raman spectroscopic analysis revealed the deprotonation and reprotonation events on a millisecond time range of meta-states Meta-Ra and Meta-Rc [116]. For Meta-F, deprotonation/reprotonation events have not been observed. Instead, changes of the hydrogen-network in the direct chromophore environment are supposed to lead to the formation of the Pr-state on a microsecond range [117] [118]. An additional pathway involves so-called dark reversion, which is a temperature-dependent relaxation from the Pfr-state to the Pr-state in a dark environment. The duration of this dark reversion is species-dependent and can range from minutes to hours. Additional factors include pH, reducing agents and concentrations of metal ions [119]. Interestingly, bacteriophytochromes lacking the PHY domain exhibit a 100 times faster thermal relaxation to the Pr-state than phytochrome PCMs [120].

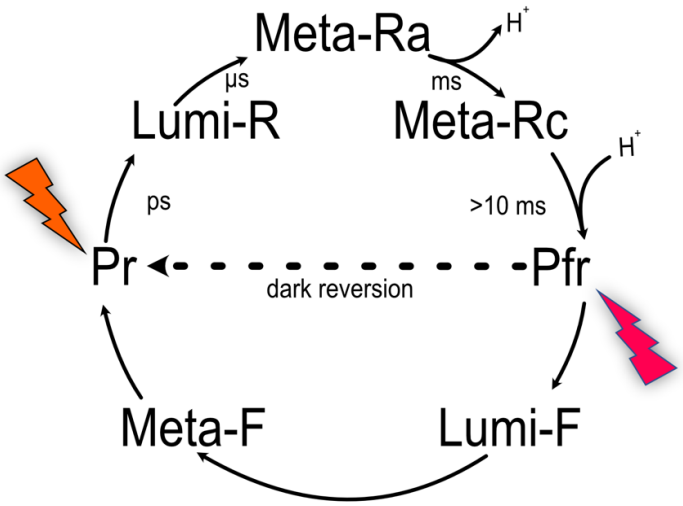

***Figure 1.13: Schematic display of the phytochrome photo cycle**. Orange and red symbols indicate illumination with light of ~700nm and 750nm, respectively. Illustration was modified after Wagner et al. [116].*

1.4.3 Bacteriophytochrome-derived FPs

Following up on the spectral limitations of GFP-like FPs, the bacteriophytochromes' inherent ability to sense NIR light made them suitable templates for the development of NIR FPs (Figure 1.14). Initial approaches aimed to suppress the inherent photocycle of bacteriophytochromes to enable constitutive fluorescence. The first engineered bacteriophytochrome-derived FP that allowed imaging of mammalian cells, Infrared Fluorescent Protein 1.4 (IFP1.4), was published in 2009 [90] and allowed excitation/emission of 684/708nm respectively with a quantum yield of 0.07. IFP1.4 consists of the CBD of the *Deinococcus radiodurans* bacteriophytochrome (DrBphP), lacking the PHY-domain as well as the C-terminal histidine kinase related domain (HKRD). The deletion of these two domains impedes a) the transduction of excited state energy into non-radiative decays and b) oligomerization tendencies by reducing potential oligomerization interfaces. However, an additional L311K mutation was required for monomerization of IFP1.4 [90]. In the following years, further NIR-FPs based on DrBphP like Wi-Phy [104] and SNIFP [121] were engineered. Furthermore, the *Radiodurans palustris* bacteriophytochrome (RpBphP) [122] was extensively mutated, which resulted in multiple FPs covering excitation maxima between 642 and 702nm [75, 123, 124]

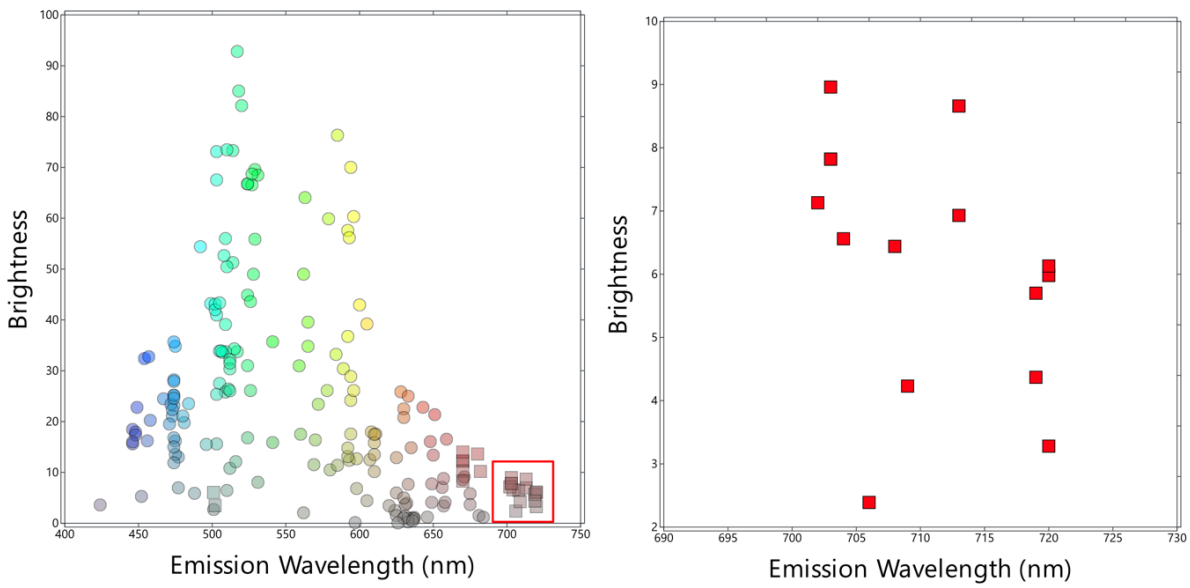

Figure 1.14: Fluorescent protein distribution across the VIS and NIR spectral regime. *Left: The molecular brightness of monomeric FPs is plotted against the emission wavelength. GFP-like FPs are depicted as circles whereas bacteriophytochrome-derived FPs are shown as squares. Right: Zoom-in to the red-highlighted region of the left image. The image clarifies the potential of bacteriophytochrome-derived FPs as there is only a limited number with comparatively low molecular brightness accessible. Values were taken from fpbase.org [125].*

Most bacteriophytochrome-derived FPs only consist of the CBD in order to lower the probability for the interaction with non-target proteins. The typical molecular weight of these CBD-consisting FPs is ~35 kDa. The bacteriophytochrome-derived FP GAF-FP only consists of the 19kDa GAF-domain which contains an inserted cysteine residue to allow for the chromophore binding [126]. This size advantage is counteracted by a spectral blueshift with excitation/emission maxima at 635/670nm, respectively, and thereby preventing its use in the NIR window. Similar properties are found for the *Nostoc punctiforme* cyanobacteriophytochrome-derived mIRFP670nano [127]. The bacteriophytochrome-derived FPs IRFP670, mIRFP670 and emIRFP670 consist of the CBD with an additional cysteine residue in the GAF-domain. It is reported that the additional cysteine residue allows for the formation of GAF- or PAS-GAF-covalently bound BV [98]. The increased QY indicates an additional stabilization of the chromophore at the expense of a 20-30nm blue-shifted excitation/emission maximum [128].

As discussed earlier, bacteriophytochrome-derived FPs have predominantly been engineered to constitutively fluoresce. The photoactivatable near-infrared fluorescent proteins 1 and 2 (PAIRFP1/PAIRFP2), which were derived from the bathy *Agrobacterium tumefaciens* bacteriophytochrome AtBphP2 and published by Piatkevich et al., in 2013 [129] have been an exception. These initially weakly fluorescent FPs can be photoactivated with far-red light and subsequently fluoresce when excited with 660nm light. Low-temperature ultraviolet-visible spectroscopy suggests a photocycle with

similar intermediate states as found in the wildtype bacteriophytochrome while simultaneously disabling the Pr-Pfr photoconversion and decreasing dark reversion rates.

In 2016, Yang et al. published the application of the non-fluorescent reversibly switchable RpBphP1 in Photoacoustic Tomography (PAT) [130]. In this PAT approach, the inherent photochromism of wildtype-bacteriophytochromes was harnessed to remove background signal, enhance detection sensitivity, increase penetration depth and improve spatial resolution.
In the same year, a microfluidic screening system for bacteriophytochrome-derived RSFPs was published by Lychagov et al. [131]. This system utilized diffractive optics for a multiple-beam illumination, allowing real-time analysis and subsequent cell sorting of promising candidates. However, this work focused more on the development and parameter optimization of a widely applicable high-throughput screening system for RSFPs than the application of the system to develop a suitable RSFP for the application in fluorescence microscopy. These examples show the versatility of bacteriophytochrome-derived FPs and the potential to develop photochromic FPs operating in the NIR window for wide-ranging applications in fluorescence microscopy.

To this point, the inherent photochromism of bacteriophytochrome-derived FPs was predominantly suppressed to generate bright constitutively NIR fluorescent proteins. Bacteriophytochrome-derived FPs for STED super-resolution microscopy like SNIFP and emIRFP703 were engineered to reside in the fluorescent Pr-state by impeding the wildtype-bacteriophytochrome photocycle. In conjunction with the inherently high extinction coefficient of bacteriophytochrome-derived FPs, this lead to an increased molecular brightness. In general, this was accomplished by restraining the flexibility of the BV D-ring, resulting in a reduction of non-radiative decays. The re-establishment of the inherent photochromism of bacteriophytochromes in a NIR-FP could lay the foundation to harness the wide range of super-resolution microscopy applications in the NIR window.

1.5 Aim of thesis

The aim of this thesis is the engineering of a bacteriophytochrome-derived RSFP and its application in NIR low laser power RESOLFT super-resolution microscopy. For this, a successor of the bacteriophytochrome-derived constitutively fluorescent protein Wi-Phy is chosen as a template. The extensive mutagenesis of this template resulted in a library of promising candidates, which were screened for key parameters required for RESOLFT microscopy. The enhancement of these key parameters in conjunction with the retention of the bacteriophytochrome-inherent photocycle were thoroughly analyzed. This screening process resulted in a final variant with novel and remarkable features. The successful application in live- and fixed-cell NIR RESOLFT microscopy demonstrates the enhanced performance of this variant and the high potential for bacteriophytochrome-derived FPs in super-resolution microscopy in the NIR spectral window.

2 Results

This work focuses on the design of the first applicable bacteriophytchrome-derived reversibly switchable fluorescent protein (BpRSFPs) and its usage in super-resolution microscopy within the NIR window. The development is carried out via directed and random PCR-based mutagenesis and is subsequently evaluated using an automated screening microscope. Promising candidates were furthermore spectrally and biochemically analyzed and finally expressed as fluorescent markers of target structures for RESOLFT imaging in mammalian cells. In the first section of this chapter, the effects of key mutations on crucial RSFP parameters as well as general spatial rearrangements in chromophore proximity are investigated.

2.1 Template choice, mutagenesis strategy and screening assay

Previously reported bacteriophytochrome-derived fluorescent proteins were engineered to suppress the natural photocycle of bacteriophytochromes in order to allow constitutive fluorescence of the Pr-state [104, 132]. Here, a template based on the constitutively fluorescent protein Wi-Phy [104] required the restoration of the Pr to Pfr/Pfr to Pr photocycle without losing its fluorescence properties. Wi-Phy itself originated from the chromophore-binding domain (CBD) of the full length *Deinococcus radiodurans* bacteriophytochrome. The foundation for this was laid by Dr. Maria Kamper, who generated a truncated form of Wi-Phy, named Wi-Phy-derived protein variant 50 (W3.50), consisting of the PAS-GAF domain of Wi-Phy. This truncated variant furthermore exhibited a F263Y mutation, preseumably allowing for the partial Pr to Pfr and Pfr to Pr photocycle at the expense of decreased fluorescence. In addition, three monomerization mutations F145S/L311E/L314E were introduced to provide suitable tagging in mammalian cells (Figure 2.1). Mutations E25Q and G270R were introduced to further enhance the BpRSFP. E25Q resulted in an improved residual fluorescence and G270R in an increased cellular fluorescence [133]. The final mutant was chosen as a template for this project due to its fast switching and high fluorescence brightness.

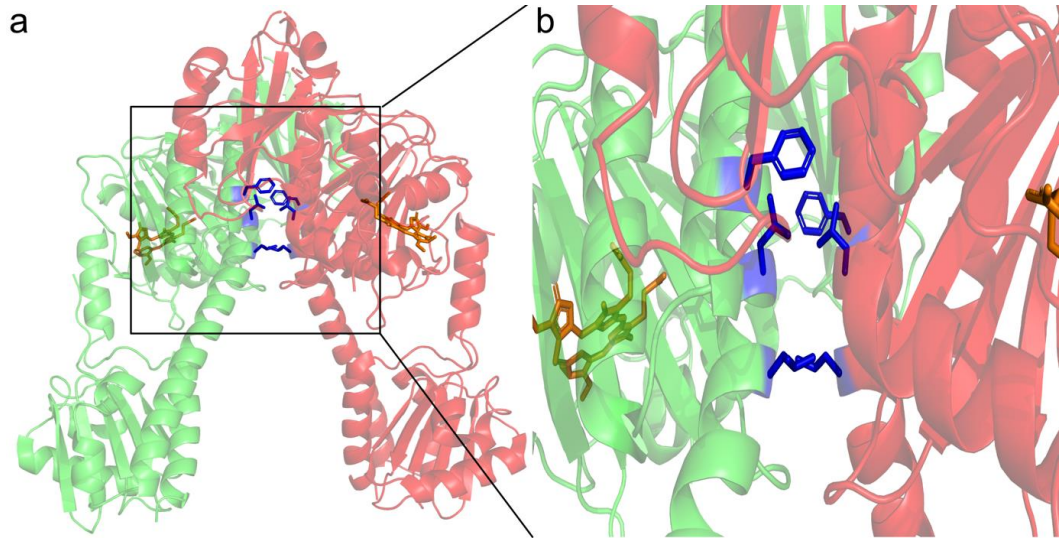

Figure 2.1: Dimerization interface of the Deinococcus radiodurans CBD. *(a) Crystal structure of the Deinococcus radiodurans homodimer with single chains colored in red and green, external chromophore BV in orange and the three dimerization causing hydrophobic amino acids F145,L311 and L314. (B) Zoom-in to the interaction site causing dimerization. [PDB ID:4O0P [134]]*

In the early stage of this project, directed mutagenesis of amino acids in close proximity to the BV chromophore was performed to increase fluorescence brightness and enhance switching between Pr- and Pfr-states. Bacterial *E. coli* cells were transformed with an expression plasmid containing the mutated gene for bacteriophytochrome expression. The cells were analyzed using an automated screening microscope. Excitation of the overexpressed bacteriophytochrome with a 660 nm laser resulted in fluorescence emission and furthermore switched the protein into the non-fluorescent Pfr-state. Switching from the non-fluorescent Pfr-state to the fluorescent on-state was achieved by illumination with 785 nm laser light, which showed negligibly low fluorescence emission. Hence, the bacteriophytochrome-derived FPs displayed in this thesis therefore belong to the group of the negative switching RSFPs.

The locations for rational mutagenesis were chosen based on crystal structures 3s7q [104], 4z1w [135] and 45q0h [100] from the protein data base (PDB). These structures resemble Wi-Phy, Wi-Phy2 and the *D.radiodurans* CBD, respectively. Within the first rounds of directed mutagenesis, amino acid positions within close proximity to the BV D-ring were chosen. The D-ring flexibility determines the transition probability of the chromophore from the fluorescent Pr-state to the non-fluorescent Pfr-state. On the other hand, increased rigidity of the D-ring in the Pr-state allows for increased fluorescence quantum yield and hence for improved fluorescence brightness.

The starting template W3.50 exhibited a sufficient brightness in comparison to previously engineered switchable bacteriophytochromes. Besides, W3.50 exhibited an off-switching half time of 80 µs, which can only be reached by GFP-like RSFPs at high laser intensities [47]. This came at the expense of a high fluorescent background of 12 % when switched to the off-state. Furthermore, repeated illumination sequences revealed a brightness decrease

of 25 % after the initial illumination protocol with 660 nm. This initial brightness could not be recovered over additional illumination sequence repeats. W3.50 additionally exhibited an instable Pfr-state, which relaxed partially to the fluorescent Pr-state without illumination within a 20 ms period. This was revealed by the application of the general illumination protocol. The general illumination protocol consisted of a 20 ms on-switching step with the 785 nm laser, a 5 ms readout and off-switching step with the 660 nm laser, a 20 ms illumination break and a subsequent 5ms readout and off-switching step with the 660 nm laser.

As introduced in section 1.3.5, potential candidates were evaluated in terms of five key parameters measured at the automated screening microscope:

1) **Fluorescence brightness:** Maximum fluorescence emission in the FP protein ensemble, when probed with 660nm illumination.
2) **Residual fluorescence**: Minimum fluorescence emission reached after 660 nm illumination as a fraction of the inital brightness.
3) **Off-switching half time**: Time required for fluorescence emission to decrease to 50 % of initial brightness upon illumination with 660 nm light.
4) **Switching fatigue:** Ratio between fluorescence brightness after 1000 on-switching/off-switching cycles and fluorescence brightness at cycle 1.
5) **Off-state to on-state transition time**: Time required for fluorescence emission to reach 50% of fluorescence brightness upon illumination with 785 nm or by thermal relaxation without applying any laser light.

A schematic representation of these key parameters in a switching curve is displayed in Figure 2.2.

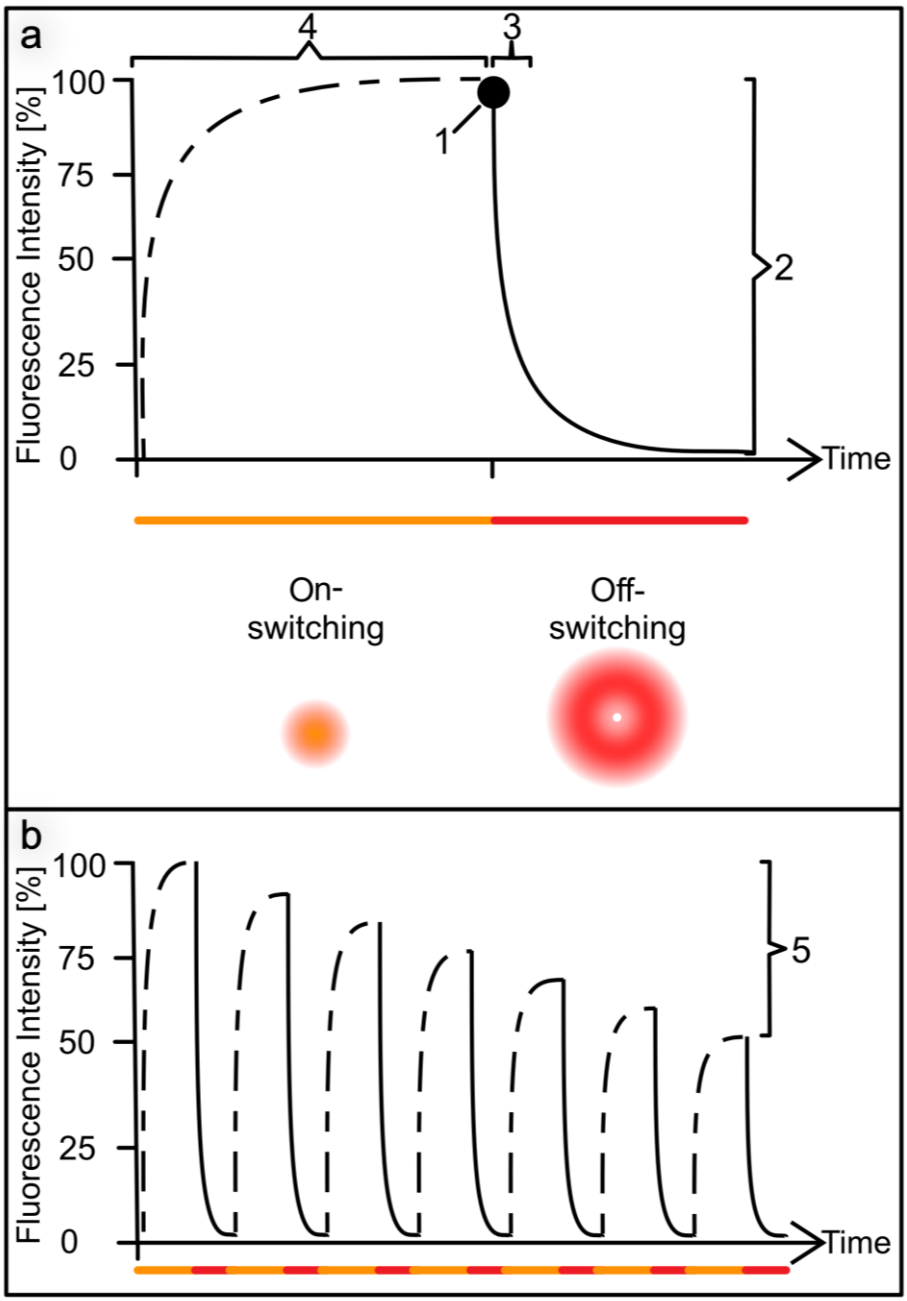

Figure 2.2 General switching scheme of a negative switching RSFP. *Dashed lines indicate on-switching/thermal relaxation to the on-state and do not result in fluorescence. Drawn through lines represent fluorescent signal (a) Depiction of a single fluorescence trace. Key parameters are represented by numbers. 1) Fluorescence brightness. 2) Residual fluorescence. 3) Switching halftime. 4) Off-state to on-state transition time. (b) Depiction of sequential fluorescent traces. 5) Switching fatigue.*

2.2 Identified mutations with beneficial properties for RESOLFT imaging

The following section will focus on amino acid mutations, which were significantly improving RESOLFT key parameters or affected the general photoswitching of bacteriophytochrome-derived RSFPs. The sum of these mutations resulted in the final variant of the protein, which was later applied in RESOLFT super-resolution microscopy.

The first introduced site-directed key mutation was M174F, which placed a hydrophobic phenylalanine in axial proximity to the BV D-ring in the Pr-state (Figure 2.3a). Characterization of the variant 10 (V10) carrying this mutation with the automated screening setup showed increased fluorescence brightness together with repeated attaining of the initial fluorescence brightness in following illumination sequences (Figure 2.4b). The residual fluorescence and off-switching kinetics were unaffected. These results endorsed additional mutagenesis steps on V10.

As previously observed in W3.50, V10 exhibited a thermal relaxation from the non-fluorescent Pfr-state to the fluorescent Pr-state. In theory, light-driven metastable on and off-states are beneficial for fluorophores used in RESOLFT microscopy in order to control the switching kinetics in both directions as a function of the applied light intensity. However, the conventional on-switching step could be exchanged with a thermal relaxation step. In the context of RSFPs, thermal relaxation describes the gradual state transition from a non-fluorescent state A to a fluorescent state B or vice versa. In the case of the BpRSFPs presented in this work, the non-fluorescent state thermally relaxes to the fluorescent state. This workaround is acceptable as long as the thermal relaxation occurs on a sufficiently short timescale but is also still sufficiently suppressed by typical off-switching light levels.

In the following round of site-directed mutagenesis, the alanine at position 288 was substituted for a valine (A288V), resulting in variant 30 (V30) (Figure 2.3b). Both amino acids show nonpolar/hydrophobic properties. The valine's additional hydrophobic methyl group extends towards the BV D-ring in the Pr-state and could pose steric as well as hydrophobic interactions. The A288V mutation of V30 resulted in a futher fluorescence increase of 33 % while maintaining a residual fluorescence of 12.5 %. Furthermore, this mutation increased the thermal relaxation speed kinetics from the Pfr- to the Pr-state and eventually reached 75 % of the initial on-switched fluorescence brightness after a relaxation period of 20 ms (Figure 2.4c).

The positions 174 and 288 were mutated against further amino acids. This did not improve the general switching parameters of the resulting variants. Besides positions 174 and 288, site-directed mutagenesis against random amino acids was performed on positions 24, 186, 196, 201. 203, 257, 259 322 and 324. These amino acid substitutions happened to be in close proximity to all rings of BV. In addition, truncations N-terminus and C-terminus were truncated. For N-term truncation, two amino acids were deleted stepwise from the

N-terminus and exchanged against a methionine start codon. Five rounds were performed to allow for a total deletion of 10 N-terminus amino acids. Stepwise N-terminus truncation only had marginal effects on fluorescence brightness and off-switching kinetics.

For C-terminus truncation, a stop-codon was stepwise inserted every two amino acids in front of the previous stop codon. Five rounds resulted in a total truncation of 10 C-terminal amino acids. Stepwise C-terminus truncation improved fluorescence brightness but simultaneously resulted in increased residual fluorescence. These observations proved the truncation of N-and C-terminus as ineffective.

After additional rounds of site-directed mutageneses did not result in significantly improved RESOLFT switching parameters, random mutagenesis was performed on V30. In eight rounds of random mutagenesis, the focus shifted from rating the five key parameters equally to prioritizing decreasing the residual fluorescence while maintaining the remaining key RESOLFT parameters. Over the course of random mutagenesis, ~ 8.000 mutants were screened, of which 100 exhibited promising or interesting features (see appendix Figure 5.2 for exemplary characterized variants).

After eight rounds of mutagenesis, variant 100 (V100) was identified as the most promising candidate. V100 exhibited a low residual fluorescence of 6 % while maintaining the thermal relaxation and off-switching kinetics of V30 (Figure 2.4d). However, V100 also showed a fluorescence decrease of 30 %, similar to the fluorescence brightness of V10. This reduced brightness was regarded as acceptable since early-stage observations of V10 as an expression construct with cytoskeletal proteins vimentin and keratin in confocal mode showed suitable cellular fluorescence brightness for imaging.

V100 exhibited the mutations G46V, R265W and T227A (Figure 2.3c). G46V is located in a loop structure of the PAS domain, but does not directly interfere with the chromophore, as the amino acid residue is located in a 34 Å distance to the chromophore. Positions 265 and 227 are located in an unstructured loop and a helix structure within the GAF domain, respectively. Based on the crystal structure of IFP2.0 (PDB ID: 4cqh), the main chains of both positions are located in close proximity, but facing away from the chromophore. Previously introduced template mutations might be responsible for an altered orientation of these amino acids or vice versa. The substitution of glycine to valine, both nonpolar amino acids exhibiting an aliphatic side chain, does not represent a major change in biochemical properties. However, steric alterations could affect surrounding amino acids and thereby influence the chromophore environment. The positively charged arginine with its hydrophilic and basic reacting guanidine group at position 265 was exchanged against the aromatic tryptophan containing an indole side chain. Both amino acids possess a comparatively long side chain. For position 227, the polar threonine was substituted with the nonpolar alanine. A sequence alignment with the wildtype *Deinococcus radiodurans* CBD, WiPhy and IFP2.0 is displayed in the appendix (Figure 5.1)

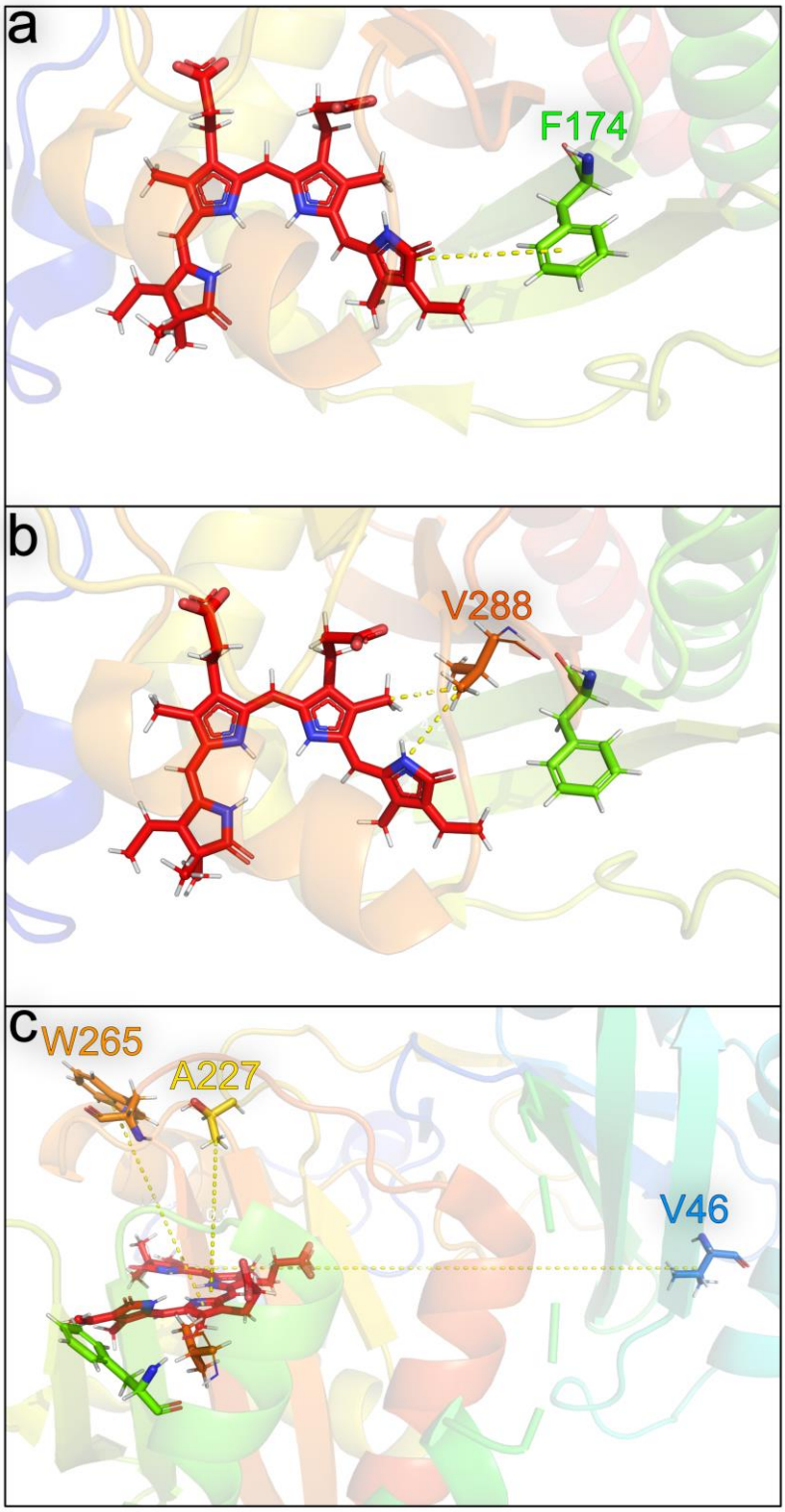

Figure 2.3: Mutagenesis of W3.50. *(a) Mutation introduced in V10 with W3.50 as a template. Indicated distance: 7.7 Å (b) Mutations introduced in V30 with V10 as a template. Indicated distance: upper: 3.5 Å. lower:4.2 Å. (c) Mutations introduced in V100 with V30 as a template. Indicated distance: left: 11.9 Å. middle:14.6 Å. right:34 Å. PDB ID: 4q0j [100].*

In summary, the final protein variant V100 contains five mutations compared to its template W3.50. These mutations are G46V/ M174F/T227A/R265W /A288V (Figure 2.3).

2.3 Detailed characterization of V100 switching parameters in comparison to predecessor variants

In the following, a comparison of the introduced variants V10, V30 and V100 together with their template W3.50 includes a sequence alignment, time-resolved fluorescence traces in *E. coli* and a depiction of the key parameters is shown.
As previously discussed, V100 exhibits the most promising features regarding its potential utilization in RESOLFT microscopy. The screening and characterization process revealed improved switching characteristics in the near-infrared window in conjunction with a photostable behavior. For this reason, V100 is referred to as PhotostablE Nir rEversibly switchabLe fluOrescent ProtEin or PENELOPE. In the following, the evolution of RESOLFT-related switching parameters in W3.50, V10, V30 and PENELOPE are compared and characterized in detail.

2.3.1 General screening protocol in *E. coli*

A general illumination protocol for screening was created for the automated screening microscope. The general illumination protocol approximated an illumination scheme, which could be applied in a later RESOLFT microscopy imaging protocol. This protocol was designed for a millisecond range, as this would allow RESOLFT microscopy imaging with suitable dwell-times. Figure 2.4 depicts exemplary raw data of the fluorescence traces of the four variants plotted over time. The general illumination protocol consisted of the following illumination step order. A 20 ms on-switching step with the 785 nm laser (12.3 mW) was followed by a 5 ms readout and off-switching step with the 660 nm laser (9.36 mW). After this step, a 20ms illumination break and a subsequent 5 ms readout and off-switching step with the 660 nm laser (9.36 mW) was applied.
The 20 ms illumination with 785 nm light was chosen to allow switching of the proteins from a Pr/Pfr equilibrium-state to the fluorescent Pr-state. During this on-switching step with a long wavelength, only minimal fluorescence emission can be detected, which can be barely discriminated from the noise of the PMT. In previous experiments, a favorable transition into the fluorescent Pr-state was observed. Ensemble proteins were switched to the non-fluorescent state using 660 nm laser light for 5 ms. This allowed for detection of fluorescence brightness, minimum residual fluorescence and the off-switching halftime. After reaching the non-fluorescent Pfr-state, the 20 ms illumination break was applied. As previously indicated in section 2.2, BpRSFP show a weak metastability of the non-fluorescent Pfr-state which thermally relaxes to the fluorescent Pr-state. Leveling the thermal relaxation time to the 20 ms on-switching time allowed for evaluation of the thermal relaxation kinetics contribution during the on-switching step. The subsequent 660 nm illumination for 5 ms again enabled detection of fluorescence brightness, minimum residual fluorescence and the off-switching halftime. This general illumination protocol was repeated

five times in order to visualize potential illumination-driven alterations of fluorescent states or transition kinetics.

For W3.50, a difference in transitioning between the on-switched equilibrium state and the on-switched Pfr-state can be observed (Figure 2.4a). While the fluorescence brightness of the on-switched equilibrium state equals the maximum fluorescence, following on-state fluorescence brightness peaks only accompany for ~ 67-74 % of this value. This effect was counteracted with the development of V10 (Figure 2.4b). Comparison of the on-switched equilibrium state and the on-switched Pfr-state revealed an almost steady response towards the 785 nm on-switching step. For V30 (Figure 2.4c) and PENELOPE (Figure 2.4d), the cycle-dependent fluorescence decrease was reversed and allowed a fluorescence increase between the on-switched equilibrium state and the on-switched Pfr-state of 5 % for V30 and 11 % for PENELOPE. This is a prerequisite for successful RESOLFT microscopy.

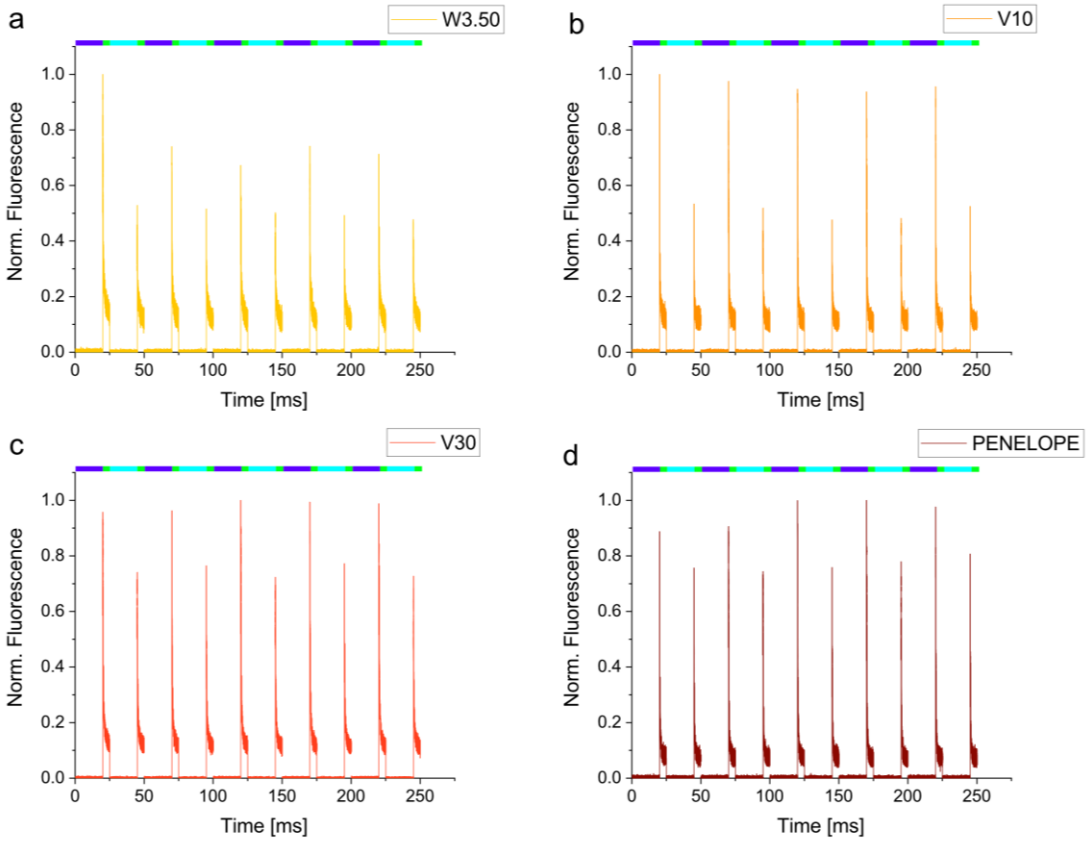

Figure 2.4: Multicycle fluorescence traces of the starting template W3.50 and its variants V10, V30 and PENELOPE. *Representative fluorescence traces (a) W3.50, (b) V10, (c) V30 and (d) PENELOPE. Fluorescence traces were normalized to the respective maximum signal. The different switching steps are indicated with a color code above the fluorescence traces. On-switching is represented by violett, off-switching by green and thermal relaxation by cyan. On-switching was performed for 20 ms with a power of 14.32 mW and off-switching was performed for 5 ms with a power of 10.67 mW. Every on-switch/off-switch sequence was followd by a sequence which exchanged the on-switch with a 20 ms illumination break to allow for thermal relaxation. Every sequence was repeated 5 times.*

A detailed depiction of single off-switching fluorescence traces is shown in Figure 2.5. The traces are equivalent to the third switching cycle and are normalized to its respective fluorescence brightness. Figure 2.5a shows a detailed view on single off-switching events indicated in Figure 2.4. Figure 2.5b displays the first 1000 µs of the off-switching curves. Off-switching fluorescence traces were subsequently used as source data for the determination of fluorescence brightness, residual fluorescence and off-switching halftime of the fluorescent Pr-state.

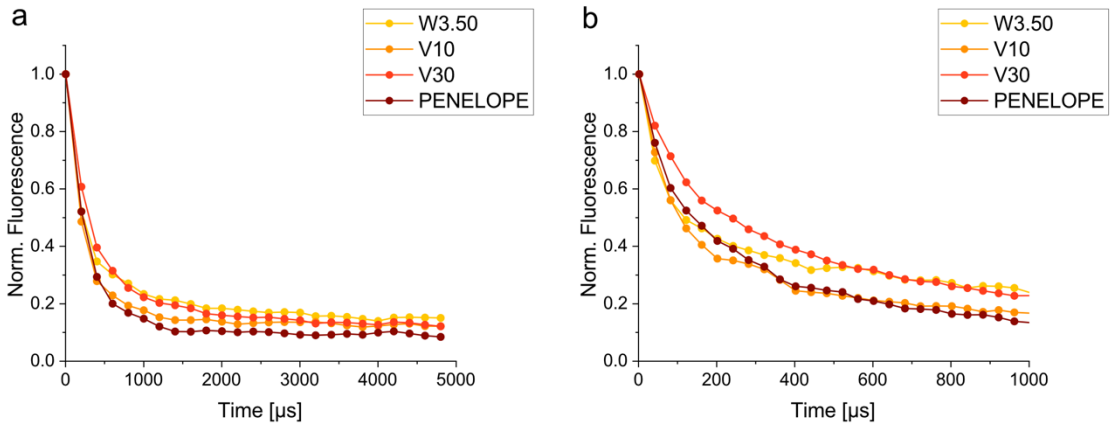

Figure 2.5: Single fluorescence traces of the off-switching step of the starting template W3.50 and its variants V10, V30 and PENELOPE. *(a) Representative fluorescence traces of the off-switching step for W3.50, V10, V30 and PENELOPE. Fluorescence traces were normalized to its respective starting point. On-switching was previously performed for 20 ms with a power of 14.32 mW and off-switching was performed for 5 ms with a power of 10.67 mW. (b) shows a zoom-in on the first 1000 µs of (a) to demonstrate distinction of early events in fluorescent traces. The displayed traces were previously sampled with a sample time of 40 µs and subsequently smoothed to allow distinction of fluorescence traces.*

2.3.2 Fluorescence brightness of the on-state

In negative switching RSFPs, the fluorescence brightness can be observed by detecting the initial fluorescence emission of the RSFP fluorescent Pr-state. With extended illumination, a fraction of the ensemble proteins transitions to the off-state and cannot contribute to the fluorescence emission. In the case of fast-switching RSFPs, the temporal resolution is therefore crucial to allow the detection of all photons of the initial fluorescence emission.
Since BpRSFPs exhibit a rapid off-switching mechanism, a sampling rate of 2 µs was chosen to allow detection of the peak fluorescence. Measurement analysis is presented in Figure 2.6 and revealed a strong linear tendency($R^2 = 0.99$) of the fluorescence emission in dependence of the applied laser intensity. For all observed powers, V30 exhibited the highest fluorescence brightness. Comparative analysis revealed a brightness increase by a factor of 3.01 of V30 compared toW3.50. PENELOPE marked the second highest increase with 2.6.

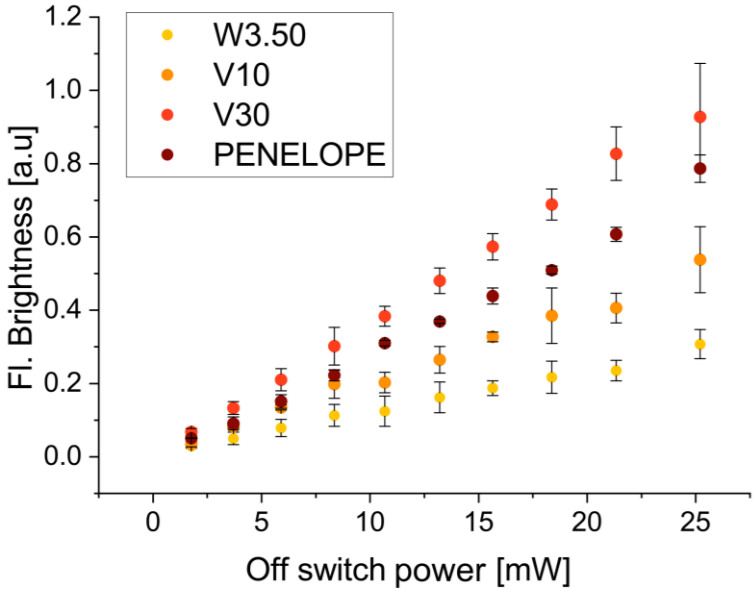

Figure 2.6: Power-dependent fluorescence brightness distribution. *Data points depict the initial fluorescence brightness of the third off-switching cycle. Proteins were previously on-switched with 785 nm laser light for 20 ms with a power of 14.32 mW. Data presents averaged values and respective standard deviation of 5 colonies. The maximum fluorescence brightness reflects the detection maximum of the PMT.*

2.3.3 Residual fluorescence of the off-state

A prerequisite for RESOLFT microscopy is the distinction between the fluorescent on-state and the non-fluorescent off-state of the chromophore. In reality, GFP-like RSFPs are limited to a minimum residual fluorescence of ~1%. However, super-resolved RESOLFT images have also been recorded with RSFPs exhibiting a residual fluorescence of 3.5 % up to 5 %. For RESOLFT microscopy to be worthwhile, a general limit of residual fluorescence is considered ~ 10 % [136].

In the automated screening system, subsequent to 785nm on-switching or thermal relaxation of BpRSFPs, the residual fluorescence was determined by illuminating bacterial colonies with 660 nm light. Since the presented BpRSFPs have a negative switching mode, the off-switching is accompanied by fluorescence emission, which allows for the visualization of the off-switching curve.

In Figure 2.7, the residual fluorescence of the presented BpRSFPs does not follow a coninuous linear trend of the fluorescence brightness due to an early saturation at 8.35 mW. The minimum residual fluorescence of 6.08 ± 0.29 % within the plateau is observed at 25.2 mW power intensity for PENELOPE. The earlier discussed general 10 % residual fluorescence threshold is approximated at low laser intensity levels of 5.9 mW with a residual fluorescence of 9.86 ± 1.8 %. For W3.50, V10 and V30, minimum residual fluorescence was observed at 18.37 mW, 25.2 mW each. The minimum residual fluorescence accounts for 12.3 3± 1.2 %, 13.56 ± 1.41 % and 9.42 ± 0.45 %, respectively.

Low 660 nm illumination up to 5.9 mW results in a linear dependence of residual fluorescence as a function of applied laser intensity for V30 and PENELOPE. W3.50 and V10 do not show a clear linear dependency at low laser powers. This might be caused by high residual fluorescence fluctuations at low illumination powers.

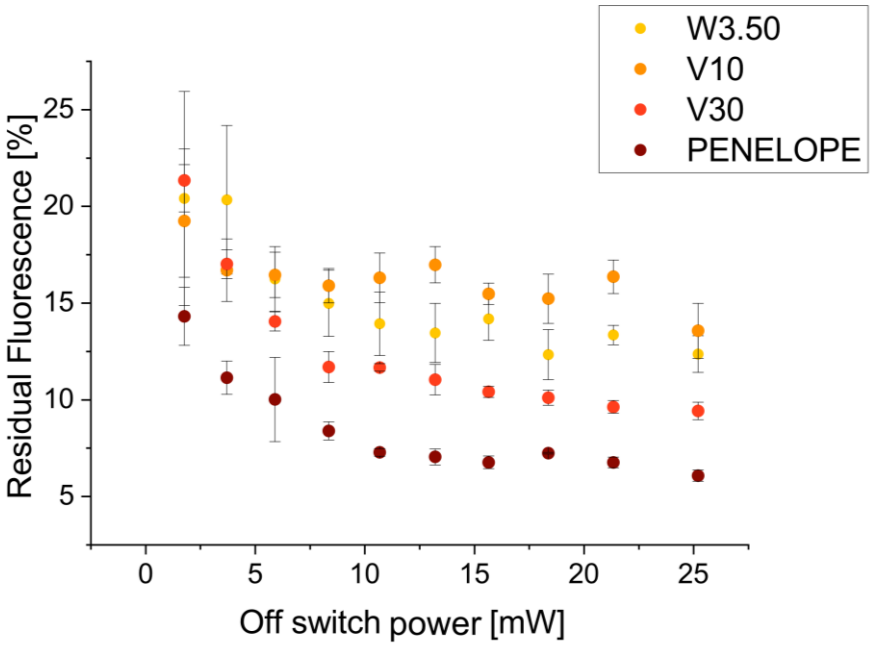

Figure 2.7: Power-dependent residual fluorescence distribution. Data points depict the residual fluorescence of the third off-switching cycle. *Datapoints taken into account for analysis consist of an average of the last 10 data points of the off-switching curve. Proteins were previously on-switched with 785 nm laser light for 20 ms with a power of 14.32mW. Data presents averaged values and respective standard deviation of 5 colonies.*

2.3.4 Off-switching half time

While a low residual fluorescence is fundamental for RESOLFT microscopy, fast switching kinetics are not a prerequisite but advantageous for RESOLFT image formation. However, a fast transition between the fluorescent and non-fluorescent state and vice versa reduces the pixel dwell time. This allows for rapid image formation, thus reducing the risk for recording motion artifacts in live specimen.

All presented variants in Figure 2.8 exhibited fast off-switching halftimes in the low µs range at low laser intensities. For the lowest laser intensity of 1.76 mW, V30 showed the slowest off-switching halftime with 185±46 µs. For the same power, W3.50 displayed a switching halftime of 55 ± 32 µs. The lowest values observed for W3.50, V10, V30 and PENELOPE are 65 ± 17 µs, 70 ± 11 µs, 126 ± 9 µs and 86 ± 4 µs, respectively. However, the insufficient residual fluorescence of W3.50 and V10 counteract this advantageous switching property. With increasing laser intensity, a saturation of the off-switching half time was measured, resulting in decelerated off-switching for V30 and only slightly increased off-switching for PENELOPE.

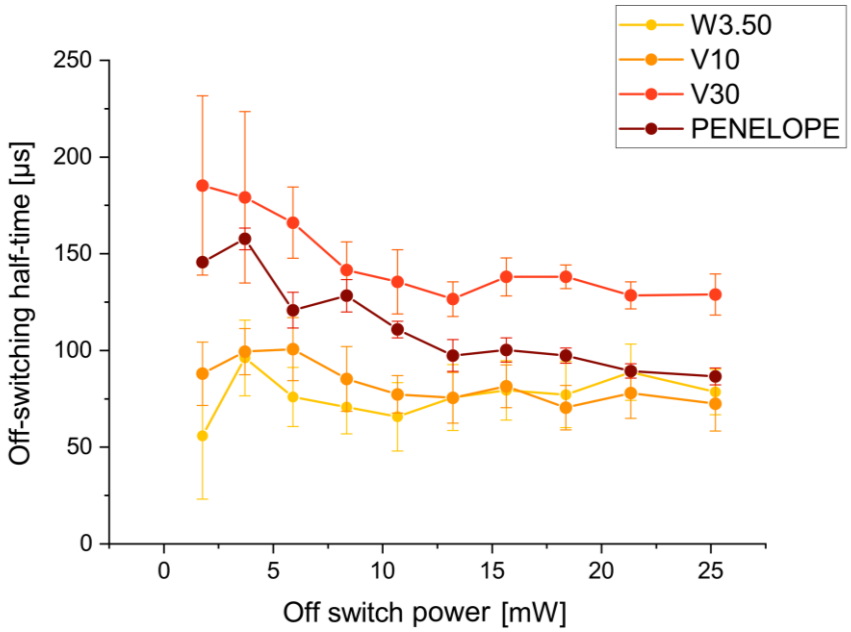

Figure 2.8: Power-dependent off-switching half time distribution. *Data points depict the off-switching half time of the third off-switching cycle. The presented data account for the points in time at which fluorescence signal between the start- and endpoint reached 50%. Proteins were previously on-switched with 785 nm laser light for 20 ms with a power of 14.32 mW. Data presents averaged values and respective standard deviation of 5 colonies.*

2.3.5 Light-dependent and light- independent transition from the Off-state to the On-state

In RESOLFT microscopy with GFP-like negative switching RSFPs, the so-called 'on-switching' step transfers the off-switched protein ensemble back into the on-state. This process does not or only barely emit photons and can therefore only be observed by probing the proteins, which transitioned back into the on-state, with a short off-switching pulse. For most negative switching GFP-like RSFPs, the on-switching wavelength is in the UV- or blue-light spectrum. Furthermore, the on-switching step shows faster kinetics compared to the off-switching step.

For BpRSFPs, the spectral shift of the on-switching step as well as its kinetics compared to the off-switching step, respectively, showed opposed patterns. The transition to the on-state was facilitated by the red-shifted wavelength of 785 nm. The 785 nm on-switching step was shown to be significantly slower than the 660 nm off-switching step. In Figure 2.9a,b, the effect of the on-switching time at maximum intensities is plotted against the fluorescence brightness and achievable residual fluorescence, respectively. Both values were extracted from the off-switching curve, which was detected subsequently to the respective on-switching step.

At maximum intensities of 14.32 mW of the 785 nm laser, the fastest response can be observed for V10. Within 20 ms, fluorescence brightness increased by a factor of 5.36 compared to fluorescence brightness detected after 1 ms. The residual fluorescence after 20 ms accounted for 15.9 5 ± 0.5 %. For V30, fluorescence brightness increased by a factor of 3.57 while obtaining a residual fluorescence of 10.35 ± 1 %. For PENELOPE and W3.50,

the fluorescence brightness was enhanced by a factor of 2.5 and 3.19 while the residual fluorescence equaled 16.6 ± 0.9 % and 9.2 ± 1.2 %.

In contrast to GFP-like RSFPs, the non-fluorescent off-state of BpRSFPs is not metastable and reverts into the fluorescent on-state also via thermal relaxation. The thermal relaxation inherently occurs simultaneously to the 785 nm induced on-switching. Figure 2.9b,d depict the effect of prolonged thermal relaxation time on fluorescence brightness and achievable residual fluorescence. The on-switching step was substituted by a thermal relaxation step in the acquisition protocol. This was implemented by switching off the 785nm laser. In Figure 2.9b, variants W3.50 and V30 show similar kinetics regarding the brightness increase as presented in Figure 2.9a. V10 and PENELOPE show different kinetics compared to the on-switch dependent fluorescence brightness in Figure 2.9a. While the thermal relaxation of V10 within 20 ms only results in a factor 3.09 increase of fluorescence brightness, PENELOPE fluorescence brightness is increased by a factor of 4.31. For RESOLFT microscopy, this will result in a reduced pixel dwell-time, which allows for faster imaging. Focusing on residual fluorescence in Figure 2.9d, a residual fluorescence increase can be observed for W3.50, V10 and V30 to 21.4 ± 2.2 %, 21.9 ± 1.5 % and 12.0 ± 0.9 % compared to the residual fluorescence shown in Figure 2.9c. For PENELOPE, a further reduction of the residual fluorescence to 8.5 ± 0.6 % is observed.

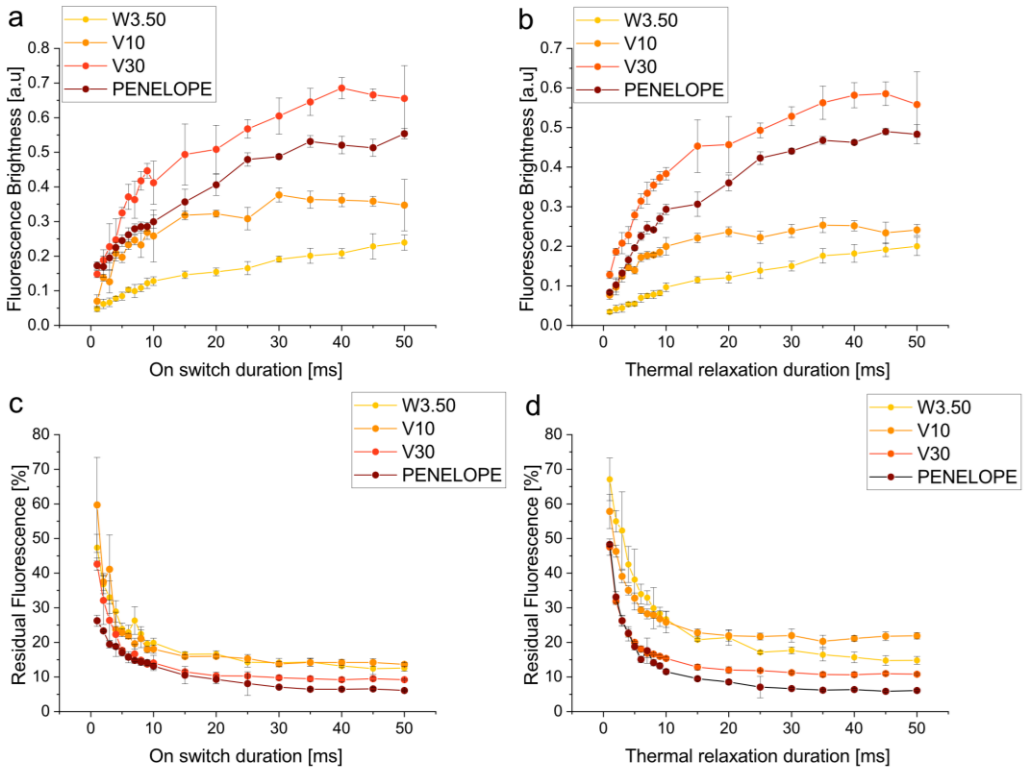

Figure 2.9: Comparison of off-state to on-state kinetics and achievable residual fluorescence as a function of applied maximum on-switch laser power and thermal relaxation. *(a) Fluorecence brightness distribution as a function of previous 785 nm on-switch duration at a maximum power of 14.32 mW. (b) Fluorescence brightness distribution as a function of a previous thermal relaxation duration without any irradiation (b). (c) Achievable residual fluorescence as a function of previously applied 785 nm on-switch duration at a maximum power of 14.32 mW. (d) Fluorescence brightness distribution as a function of a previousthermal relaxation step without any irradiation. Readout of data points was performed with the 660 nm off-switching laser for 5 ms with a power of 10.67 mW. Data presents averaged values and respective standard deviation of 5 colonies.*

2.3.6 Resistance to switching fatigue

In point-scanning RESOLFT microscopy, sample fluorophores are repeatedly switched by different illuminations during the formation of a single image. This leads to gradual photobleaching of a subset of fluorophores, which ultimately cannot contribute to the super-resolved image formation. A quantitative metric for this is the switching fatigue, which can be described as the number of performed switching cycles before the fluorescence brightness reaches 50%. At the time of the implementation of the switching fatigue experiment, utilization of the thermal relaxation step in RESOLFT microscopy proved already successful. For this reason, this experiment was conducted with a thermal relaxation step instead of a 785nm-induced on-switching step. In addition, it was assumed that this would result in an improved resistance to switching fatigue.

The switching fatigue was determined by repeating 1000 full switching cycles. These cycles consisted of a 20 ms thermal relaxation step, followed, by a 3 ms off-switching step with a power of 10.67 mW. The results are presented in Figure 2.10a,b, where Figure 2.10b is a zoom-in to the initial 200 cycles of Figure 2.10a. Due to the previously discussed initial loss

of fluorescence brightness in W3.50 (section 2.3.1), a steep decrease of 32% was observed over 40 cycles. W3.50 furthermore exhibited the strongest switching fatigue with 213 cycles. Variants V10, V30 and PENELOPE showed a stable cycle-dependent decrease and reached 50% initial brightness after 406, 539 and 434 cycles, respectively. In addition, power-dependent switching fatigue was exemplarily analyzed for PENELOPE by performing the off-switching step with four different laser powers (Figure 2.10a,b). The laser powers covered intensities 1.91 mW, 3.92 mW, 16.71 mW and 26.42 mW. For the lowest laser power, 1.91 mW, 50 % on-state fluorescence intensity was reached after 972 cycles. For increasing laser intensities, 50% on-state fluorescence intensity was reached after 594, 302 and 201 cycles, respectively. Similar resistance switching fatigue can be assumed for variants V10 and V30.

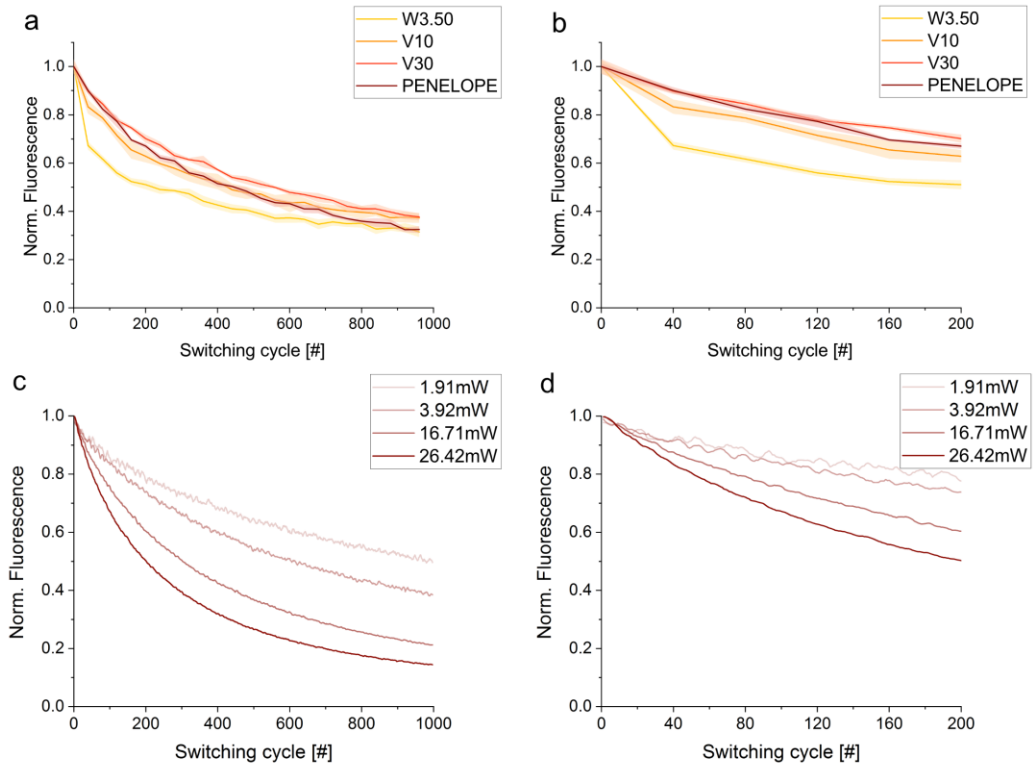

Figure 2.10: Switching fatigue in bacterial colonies.*Proteins were switched off with 660 nm for 3 ms and a power of 10.67 mW after a 20 ms thermal relaxation step for 1000 cycles. The displayed traces were previously sampled with a sample rate of 40 and subsequently smoothed to allow sufficient distinction of fluorescence traces. The standard deviation is indicated by the surrounding higher transparency area. (b) zoom-in to the first 200 cycles of (a). (c) power-dependency of the switching fatigue exemplaray for PENELOPE. Again, proteins were switched off with 660 nm for 3 ms and with varying powers after a 20 ms thermal relaxation step for 1000 cycles. (d) zoom-in to the first 200 cycles of (c). Fluorescence traces were smoothed with a 5 points window size Savitzky-Golay filter.*

***Table 2.1: RESOLFT key parameter comparison of generated bacteriophytochrome-derived RSFPs**. Demonstrated data depict the most suitable determined values for RESOLFT microscopy.*

Parameter	W3.50	V10	V30	PENELOPE
Fluorescence brightness [a.u]	0.30 ± 0.03	0.53 ± 0.09	0.92 ± 0.14	0.78 ± 0.03
Residual fluorecence [%]	12.33 ± 1.29	13.56 ± 1.41	9.42 ± 0.45	6.08 ± 0.28
Off-switching half time [µs]	65.71 ± 17.6	70.39 ± 11.5	126.59 ± 8.94	86.61 ± 4.4
Fluorescence brightness after 20 ms on-switch [a.u]	0.15 ± 0.01	0.32 ± 0.01	0.50 ± 0.06	0.40 ± 0.03
Fluorescence brightness after 20 ms thermal relaxation [a.u]	0.12 ± 0.01	0.23 ± 0.01	0.45 ± 0.07	0.36 ± 0.01
Switching fatigue resistance [#cycles]	213	406	593	434

2.4 Biophysical characterization of the final variant PENELOPE in vitro

The comparative characterization of BpRSFPs engineered over the course of this thesis revealed interesting properties for all observed variants. The possibility to perform fast switching between discernible ensemble on- and off-states highlights their potential for the application in super-resolution microscopy. For RESOLFT microscopy, PENELOPE exhibited the most promising properties, including the lowest residual fluorescence, increased thermal relaxation kinetics, fast off-switching and high switching fatigue.

Besides the switching kinetics analysis in bacteria, spectral properties of PENELOPE were analyzed in vitro using biophysical measurements. These measurements allow analyzing quantifiable amounts of protein in the micromolar range. For biophysical measurements, PENELOPE was purified from BV synthesizing bacterial colonies and suspended in Tris-NaCl buffer. Purification and subsequent SDS-PAGE ensured that solely PENELOPE contributed to detected signal in biophysical measurements. Investigated biophysical parameters include spectroscopic, fluorescence lifetime and fluorescence quantum yield measurements as well as SDS PAGE and size exclusion chromatography for the determination of oligomeric states of PENELOPE.

2.4.1 Spectral properties of PENELOPE

In order to verify the optical properties of PENELOPE and ensure its continuant switching in the NIR-spectral window, absorption as well as excitation/emission spectra were recorded. Due to its photochromic nature, the fluorescent and non-fluorescent states were addressed and spectrally investigated.

In Figure 2.11a, absorption spectra of the fluorescent on-state and the non-fluorescent off-state are depicted. The 10 µM protein solution was equilibrated over night at room temperature in the dark. Prior to the measurement, PENELOPE was switched in solution to the fluorescent on-state with 780 nm light. For the transition to the off-state, PENELOPE was switched in solution to the non-fluorescent off-state with 660 nm light. All spectra showed three distinct peaks at ~280 nm, ~380 nm and 690 nm. Both absorption spectra traces were normalized to the absorption peak at 280 nm, which is the absorption of aromatic amino acids. The Soret band at around 380 nm is a porphyrin molecule characteristic and is caused by the $\pi - \pi*$ transition of the BV chromophore. The 689 nm absorption peak of the on-state chromophore is known as the Q-band and is also caused by the absorption of BV. In the off-state, the chromophore absorption maximum at 688 nm within the Q-band decreases by ~50 %, while a redshifted absorbing band forms extending until 790 nm. In addition, the Soret band absorption is also slightly increased and shows a bathochromic shift of 5 nm. The difference spectrum in Figure 2.11b clarifies the occurring absorption changes between the fluorescent on-state and the non-fluorescent off-state. In previous absorption spectroscopy experiments, a strong resemblance of the on- and equilibrium state was observed, which is why Figure 2.11a only shows the on- and off-state.

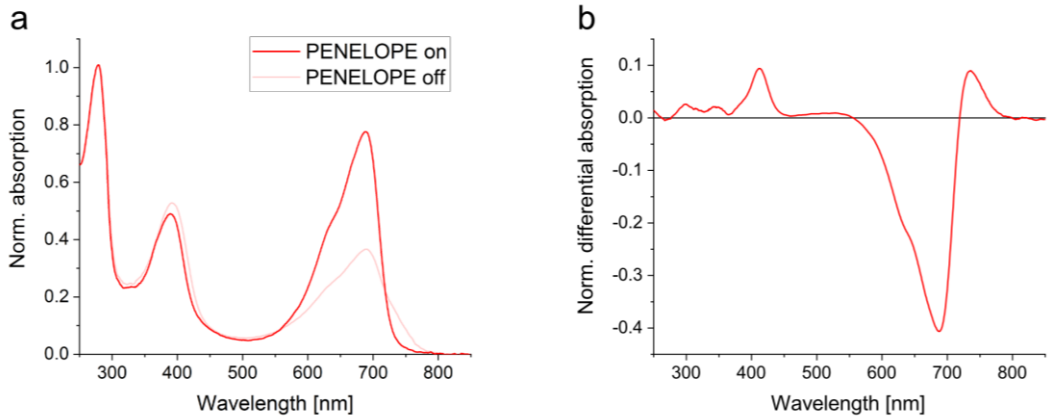

Figure 2.11: Absorption spectra of final switchig states and difference spectrum of PENELOPE. *Purified protein was switched in a cuvette with 785 nm light for on-switching and 660 nm light for off-switching and absorption spectra displayed in (a) were recorded. Spectra were normalized to the absorption of aromatic amino acids at 280 nm. The difference spectrum shown in (b) was generated by subtracting the absorption spectrum of the on-switched protein solution from the absorption spectrum of the off-switched protein solution.*

Figure 2.12a illustrates the off-switching kinetics of PENELOPE in vitro. Due to its fast off-switching kinetics, low light intensities of 1.11 kW/cm^2 were chosen. The starting point was chosen to be the equilibrium state without an additional on-switching step. The low laser intensities allowed a gradual off-switching and subsequent detection on a second timescale after each switching step. After 180 s, no further off-switching was achieved. Figure 2.12b depicts the on-switching kinetics of PENELOPE in vitro. For this, the previously off-switched protein solution was switched on again with high 780 nm intensities of 18.7 kW/cm^2. Despite these high laser powers, on-switching was gradually performed for up to 360 s until a saturation was reached. The high metastability of the gradual off-switching was unexpected as it did not support the observations made in 2.3.5 in bacterial cells. These differences are likely to be explained by differently occurring dark states. These differences are likely to be caused by the different focal spot intensities applied as well as alternate time ranges observed compared to bacterial cells.

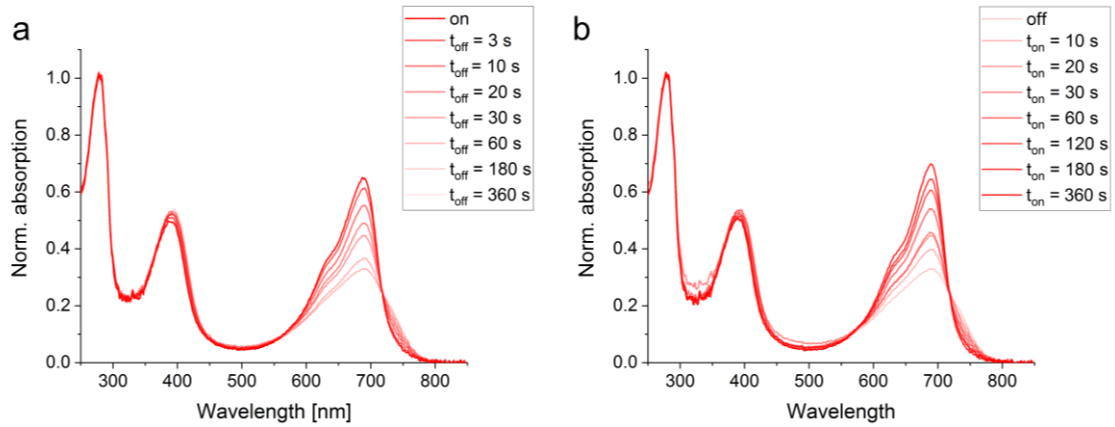

Figure 2.12: Absorption spectra of intermediate switchig states from the on to off-switching and off to on-switching of PENELOPE. *Purified protein was switched in a cuvette with 50 µW 660 nm light (a) for off-switching and with 1 mW 785 nm light (b) for on-switching. Absorption spectra of the intermediate states were immediately recorded. Spectra were normalized to the absorption of aromatic amino acids at 280 nm.*

In order to investigate the occurrence of thermal relaxation of PENELOPE in vitro, off-switched protein solution was analyzed on an hour-timescale without light illumination. The results are shown in Figure 2.13a. The protein solution was first transitioned into the on-state for 5 min using 780 nm light before transitioning it to the off-state for 5 min using 660 nm light. The spectra were spectrally analyzed after the completion of every switching step. Over the course of 90 min, thermal relaxation was observed. This thermal relaxation in the minute-range indicates a fundamentally different population of off-states than observed in bacteria.

Fluorescence excitation and emission spectra are shown in Figure 2.13b. The fluorescence excitation maximum is found at 688 nm, whereas the emission maximum is 712 nm. Figure **2.13**b shows the excitation and emission spectra of the equilibrium-, on- and off-state. In contrast to GFP-like RSFPs, the lowest residual fluorescence state still amounts to more than 40% of the excitation and emission signal, respectively. This phenomenon could be

explained by insufficient off-switching caused by spectral cross-talk leading to a simultaneous on-switching while switching off. This would ultimately result in an equilibrium. Furthermore, the spectral traces show that the equilibrated form of PENELOPE resembles the on-state to a large extent.

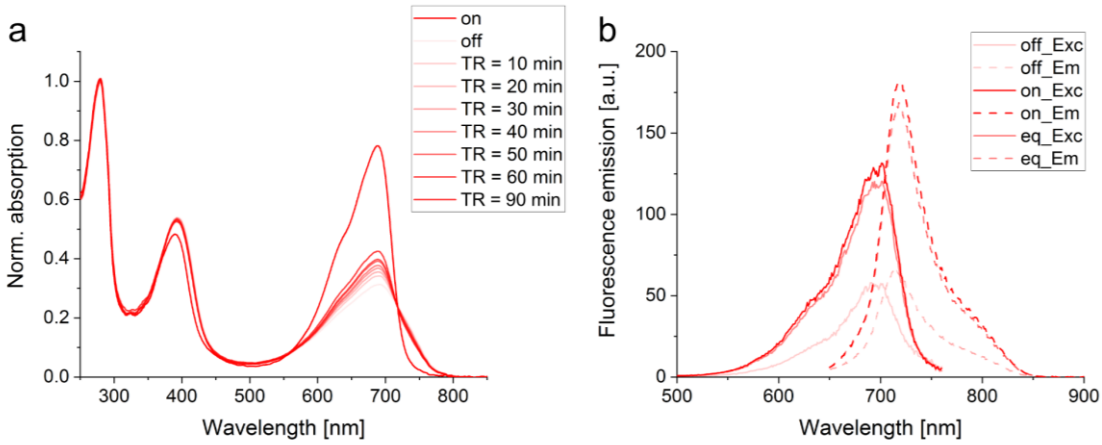

Figure 2.13: Absorption spectra of intermediate thermal relaxation-states and excitation/emission spectra of switching states of PENELOPE. *(a) Purified protein was switched from the on-state to the off-state in a cuvette for 5 min with 1.11 kW/cm² 660 nm light. Absorption spectra of the thermally relaxed intermediate states (TR) were immediately recorded after 10 min of thermal relaxation, for 1 h. A final probe detection was performed after 90 min. Spectra were normalized to the absorption of aromatic amino acids at 280 nm. Thermal relaxation is abbreviated as TR. (b) Excitation and emission spectra were recorded at pH 7.5 with detection at 780 nm or excitation at 640 nm, respectively. Initial measurements were performed on the equilibrated sample.*

2.4.2 pH-dependent spectral properties of PENELOPE

Fluorescent proteins for live cell imaging require a strong pH stability in order to allow imaging of all potential cellular structures and organelles. While lysosomes and endosomes contain an acidic environment with a pH ~4.7 [137] and pH ~5.5 [138], respectively, mitochondria exhibit neutral and low basic pH of 7 in the intermembrane space and pH 8 in the mitochondrial matrix [139]. The pH stability of PENELOPE was investigated by observing its absorption spectra and fluorescence emission in dependence of the surrounding pH. For this, a PENELOPE stock solution was added to buffers ranging from pH 3 to pH 9 resulting in a molar concentration of 20 µM protein. The measurements were performed in technical triplicates.

In Figure 2.14a, pH-dependent absorption spectra from pH 5.5 to pH 10 are shown. The pH environment affects the absorption of the Soret band as well as the Q-band. In the acidic environment of pH 5.5, the Soret peak absorption is at its minimum whereas the Q-band absorption reached its maximum. With increasing pH-values, the Soret peak absorption increases while the Q-band absorption decreases. Both bands reach an equally high absorption at pH7. For pH-values below 5.5, the Soret peak and Q-band vanished while the 280 nm peak increased. This would indicate the destruction of the chromophore at these

pH-values, which was not the case for the pH-dependent fluorescence emission spectra shown in Figure 2.14b. Fluorescence emission response to the excitation with 660 nm light was observed from pH 3 to pH 10. Fluorescence emission was detected from pH 4.5 up to pH 9.5, reaching a peak emission at pH 5.5. pH-dependent fluorescence emission data allowed pK_a-value determination. The rapid fluorescence increase between pH 4 to pH 5.5 and the slow decrease between pH 5.5 to pH 10 did not allow fitting with a single function. Therefore, the pK_a-values pK_{a1} and pK_{a2} were determined using two different fitting functions. For pK_{a1}-value determination, a monophasic dose response function (see Eq. 11.1) was chosen which resulted in a pK_{a1}-value of 4.59. For the determination of pK_{a2}, values ranging from pH 5.5 to pH 10 were fitted with a biphasic dose response function and resulted in a pK_{a2}-value of 7.83 (see Eq.11.2). Covering the range from pH 4.59 to pH 7.83 in terms of pH-dependent fluorescence emission allows PENELOPE suitable tagging of all cellular structures and organelles. The corresponding equation for the monophasic dose response is:

$$f(pH) = A_1 + \frac{A_2 - A_1}{1 + 10^{(LOGx0 - x)p}} \qquad (Eq.\,11.1)$$

with A_1 as the bottom asymptote, A_2 as the top asymptote, LOGx0 as the center and p as the hill slope.

The corresponding equation for the binophasic dose response is:

$$f(pH) = A_1 + (A_2 - A_1)\left[\frac{p}{1 + 10^{(LOGx01 - x)h_1}} + \frac{1 - p}{1 + 10^{(LOGx02) - x)h_2}}\right] \qquad (Eq.\,11.2)$$

with A1 as the bottom value, A2 as the top value, LOGx01 as the 1st EC50 value, LOGx02 as the 2nd EC50 value, h1 as slope 1, h2 as slope 2 and p as the proportion.

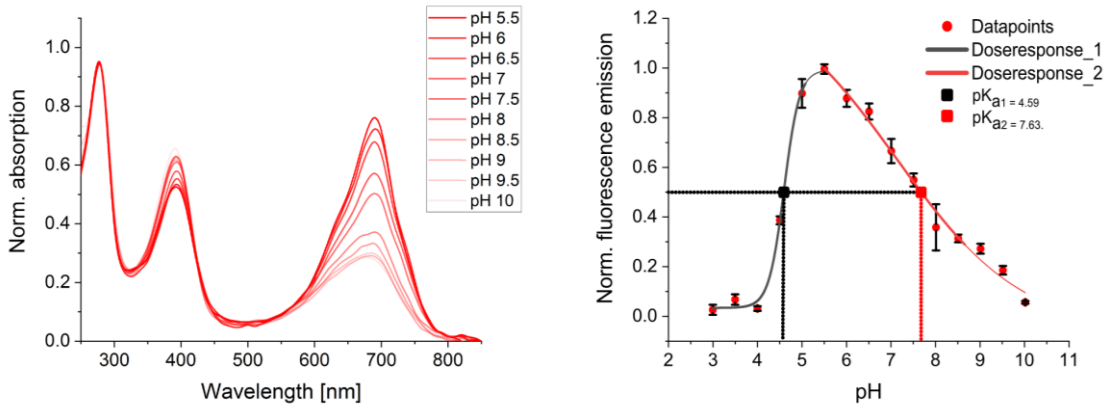

Figure 2.14: pH-dependent absorption and fluorescence emission spectra. *(a) Equilibrium absorption spectra depicted were measured over a range from pH3 to pH10. Absorption spectra for pH values 3 to 5 were excluded from the analysis*

due to an exceedingly high signal at 280 nm. Fluorescence emission in (b) was measured with a 650/19 nm excitation and a 700/19 nm detection filter and results are depicted as a function of pH.

2.4.3 Extinction coefficient, fluorescence quantum yield and lifetime

Besides the spectral behavior of fluorescent proteins, values representing the extinction coefficient, fluorescence quantum yield and lifetime derive the applicability of fluorescent proteins for fluorescence microscopy imaging. The extinction coefficient as a quantity for light absorption at a given wavelength was determined for the on- and off-state of PENELOPE. Based on the respective absorption spectra, the extinction coefficient of PENELOPE was amounted to $\varepsilon_{670\ nm}$ = 65271 M^{-1} cm^{-1} in the on-state. The extinction coefficient was calculated in comparison to mIRFP703. The fluorescence quantum yield (QY) was verified using two different approaches. In the first experimental approach, QYs of all absorbing species within the sample are detected with a commercially available Quantaurus QY system. This includes absorbing but non-fluorescent species, which are represented by misfolded or off-state proteins, which are likely to occur in, equilibrated RSFP protein solutions. The second experimental approach was conducted by Dr. Alexey Chizhik in a custom-built nanocavity system [140, 141] . This approach neglected absorbing but non-emitting species, resulting in ultimately higher QY values. Furthermore, the utilized volumes for the nanocavity method were significantly smaller and allowed to be switched with LEDs in between measurements. The Quantaurus-QY measurement resulted in a QY of 0.02. The nanocavity measurement resulted in QY values of the equilibrium-, on- and off-state and resulted in QYs of 0.09, 0.11 and 0.05 respectively. The molecular brightness as the product of EC and QY divided by 1000 is 7.81. Furthermore, the nanocavity method allowed determination of the fluorescence lifetime of the discernible states. These were 690ps and 570ps, for the on- and off-state, respectively. However, taking the possibility of the detection of mixed populations into account, these values should be rather seen as estimates than fix values.

2.4.4 Oligomerization tendencies of PENELOPE

Fluorescent proteins exhibiting oligomeric tendencies at already low concentrations interfere with its use in fluorescence microscopy due to interference with the protein of interest and the resulting formation of artifacts. In order to validate the applicability of PENELOPE as an adequate fusion tag, its tendency to oligomerize was investigated using semi-native polyacrylamide gel electrophoresis (PAGE) and size exclusion chromatography (SEC).

Seminative PAGE is supposed to allow for multimeric stable protein interactions of secondary structures. Low sodium dodecyl sulfate (SDS) concentrations in the buffer can however conceal weak protein interactions. For seminative PAGE, 4 µg of purified PENELOPE protein solution were added per lane. In addition, a molecular marker was run on the same PAGE as PENELOPE. Figure 2.15b shows the fluorescence image of the

seminative PAGE in the red, whereas Figure 2.15c shows the same gel with a Coomassie staining.

Size exclusion chromatography (SEC) was performed to identify weaker interactions, which were shielded by the use of low SDS concentrations in the seminative PAGE. SEC of standardized molecular markers prior to the sample run of PENELOPE allowed making a definite statement about the molecular size of PENELOPE. Furthermore, SEC was performed in a cold room at 6°C to display potential weak interactions of the proteins. The applied sample volume per run consisted of 300 µl of 20 µM protein sample each. The elution traces for PENELOPE and GFP-like controls mEGFP and dTomato in Figure 2.15a show the maximum peak at elution volumes 15.5 mL, 16 ml and 14 ml, respectively. These elution volumes equal molecular weights of 33.5 kDa, 26.7 kDa and 55.3 kDa, respectively, which closely resemble the molecular weights in literature (34 kDa, 27 kDa and 54 kDa, respectively). For PENELOPE, an early shoulder at 13.8 mL was visible, hinting towards a small subfraction displaying dimeric tendencies at low temperatures. Given the small volume of this subfraction along with the low temperatures at which the experiment was performed, a monomeric behavior of PENELOPE in live-cell microscopy applications can be expected. Post-elution peak traces exhibit detectable disturbances. After the experiment, a contraction of the utilized SEC-column was observed. This contraction resulted in a gap between the injection valve and the agarose-dextran gel network, which presumably lead to sample swirls before entering the gel network.

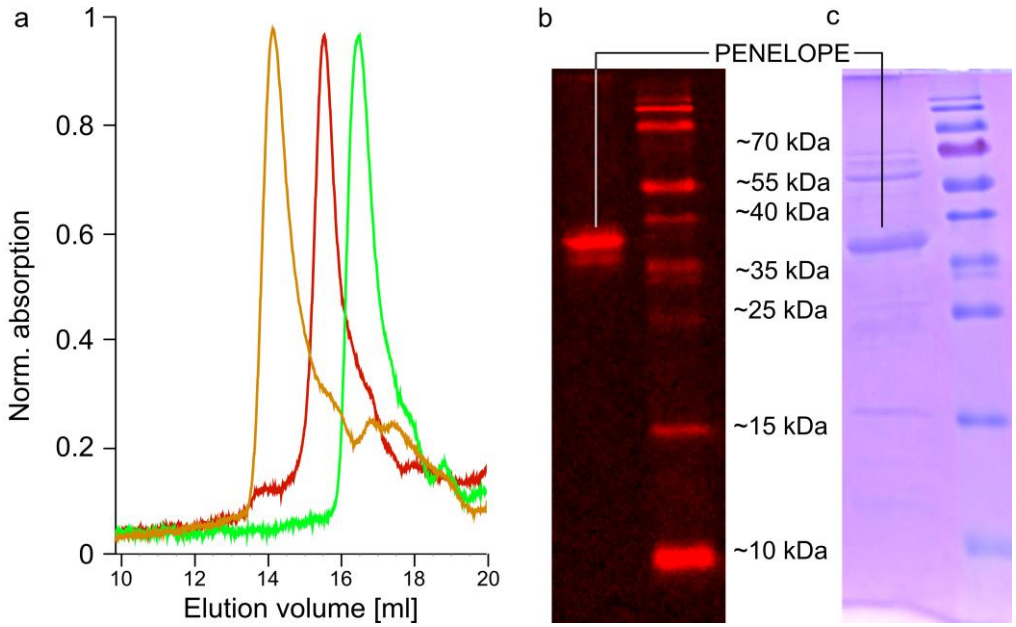

Figure 2.15: Size exclusion chromatography and seminative polyacrymalide gel electrophoresis. *(a) Protein absorption at 280 nm was detected after size exclusion chromatography (SEC) of protein samples with 10 µM concentration. SEC was performed at 6°C. dTomato and mEGFP were used as dimeric and monomeric GFP markers. (b) Fluorescence image of PENELOPE in a seminative PAGE. (c) shows the same gel as presented in (b) after fluorescence emission with a coomassie blue staining. PageRuler prestained DNA lader was used as a molecular weight marker.*

Spectroscopic analysis revealed a high complexity of the absorption-states of PENELOPE. These could be caused by spectral cross-talk, which could be circumvented by trying to address respective states with more hypochromic and bathochromic wavelengths. However, the wide range of pH-values, in which PENELOPE maintains its fluorescence in conjunction with its monomeric behavior strengthens its potential for the application in (super-resolution) microscopy.

2.5 PENELOPE in fluorescence microscopy

Following up on the biophysical characterization of PENELOPE in vitro, this section will focus on the final application of PENELOPE as a suitable fusion tag for confocal and RESOLFT super-resolution microscopy in mammalian cells. For this, prior addition of 25 µM BV to the cell-containing medium was required to enable increased cellular brightness of PENELOPE. All images displayed are raw data except if stated otherwise.

2.5.1 Confocal imaging of transiently transfected cells

In order to assess the applicability of PENELOPE for NIR live-cell microscopy, several fusion tags targeting diverse cellular structures were cloned and expressed in human HeLa cells (Figure 2.16). Before imaging, micromolar concentrations of BV were added to ensure sufficient saturation of PENELOPE with the exogenous chromophore.
Cytoskeletal structures visualized comprise of PENELOPE fused to vimentin, cytokeratin18, tubulin, microtubule ends EB3 and the Lifeact-targeted β-actin. The nucleus was visualized by cloning PENELOPE as a fusion construct with Nup50 as part of the nuclear pore complex. Chromatin labeling was achieved via a H2B fusion construct with H2B being one of the five major histone proteins interacting with DNA. Furthermore, PENELOPE was successfully targeted towards the mitochondrial matrix, peroxisomes, lysosomes, vesicles and peroxisomes. Transient transfection inherently does not allow the homogenously distributed uptake of plasmid DNA. This resulted in a subpopulation of transfected cells exhibiting overexpression artifacts. Images displayed in Figure 2.16 show cellular structures with expected localization and brightness distribution. As indicated in section 2.4.2, PENELOPE allowed the successful imaging of cellular organelles with varying pH conditions. PENELOPE was able to fluoresce in the basic environment of mitochondria as well as in the acidic pH of lysosomes. The low cellular fluorescence of PENELOPE proofed to be challenging when imaging sparsely labeled cellular structures. This is due to limited signal detection as a consequence of the low molecular brightness. Densely labeled structures such as cytoskeletal vimentin and keratin resulted in sufficient signal detection. Confocal images revealed an aggregation tendency of proteins in cells displaying uncommonly bright structures, which indicate aberrant overexpression artifacts.
In addition to imaging transiently transfected cells, a stably expressing cytokeratin18-Bxb1 landing pad cell line was generated. This cell line showed the expected subcellular

localization without interfering with cell morphology or growth, indicating the biocompatibility of PENELOPE as a genomically integrated fusion tag. Moreover, this cell line allowed for the development of a high resolution and reproducible RESOLFT imaging protocol. This is due to repeatedly achieved homogenous expression levels in a high number of cells, which cannot be ensured in transiently transfected cells.

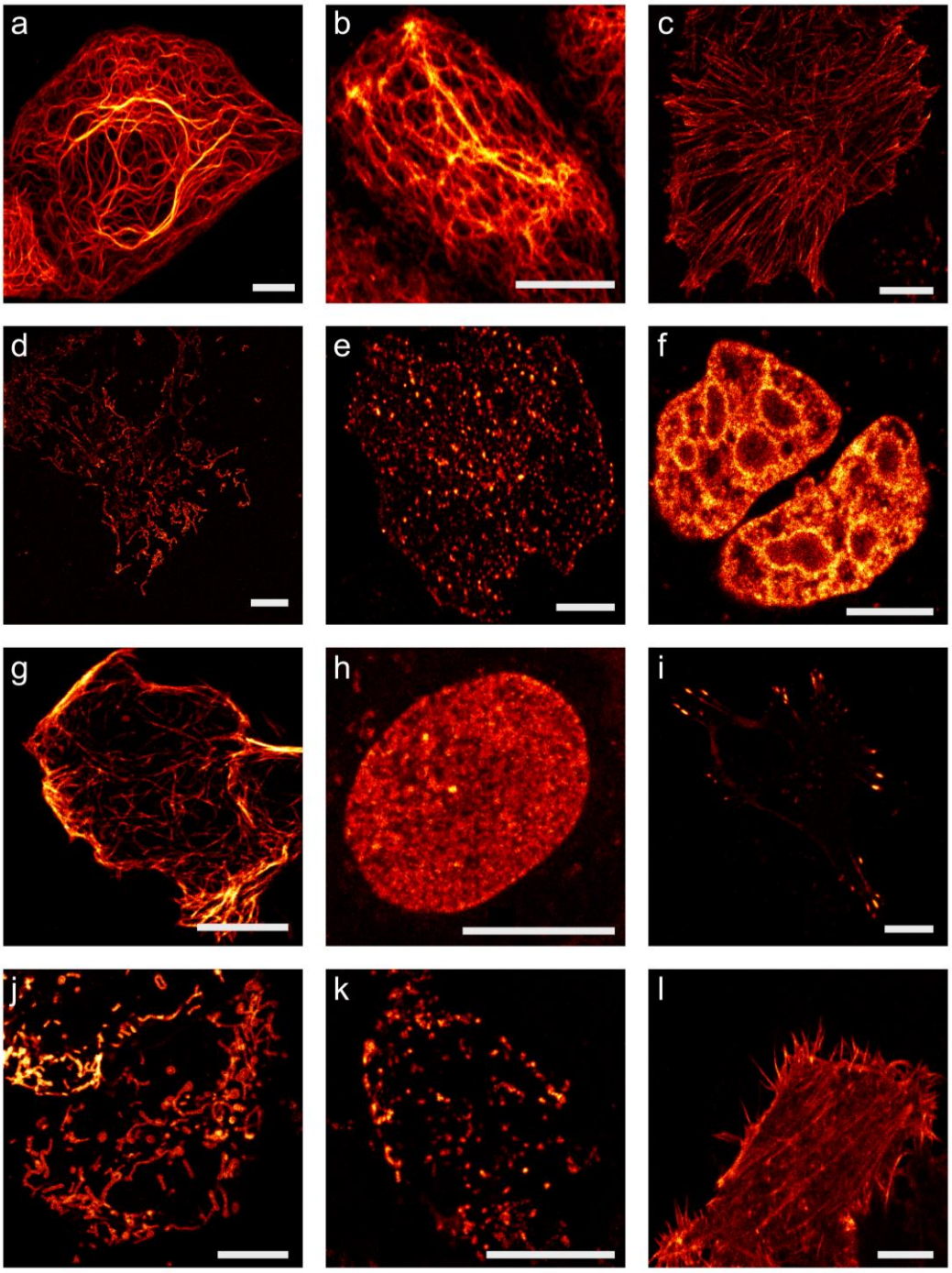

Figure 2.16: Confocal localizations of cellular structures with PENELOPE-fusion constructs. *Transiently transfected HeLa cells expressed PENELOPE-tagged cellular structures (a) cytokeratin18, (b) vimentin, (c) microtubule ends (EB3), (d) mitochondria (Omp25), (e) lysosomes (Lamp1), (f) histones (H2Bn), (g) microtubules, (h) nuclear pores (Nup50), (i) zyxin, (j) mitochondria (Cox8a), (k) peroxisomes and (l) actin (LifeAct). 25 µm BV was added 2 h before imaging. Scale bars: 10µm.*

In summary, the application of PENELOPE in confocal microscopy targets the most important cellular structures in living cells successfully. Oligomeric tendencies were not observed.

2.5.2 Photostability of PENELOPE under confocal conditions

The high resitiance to switching fatigue of PENELOPE in the screening setup, which was earlier discussed in section 2.3.6, suggested a favorable photostability. This was further evaluated under confocal conditions in a mammalian expression system. For this, living HeLa cells were transiently transfected with a plasmid expressing a PENELOPE-LifeAct fusion construct. 24 h after transfection, a single cell was imaged for 5000 consecutive frames under confocal conditions. Figure 2.17a displays selected images recorded within the 5000 frames. In order to enhance the visibility of the images, a bleaching correction based on a histogram matching algorithm was applied. For the calculation of the frame-dependent brightness distribution shown in Figure 2.17b, the raw image data were used. The graph displays the average brightness of every 100^{th} frame. After ~ 2300 frames, the average image brightness was 5 0% of the initial brightness of the first frame. Over the course of the image formation of living cells, primary indicators of cellular stress e.g., cell shrinking were not observed.

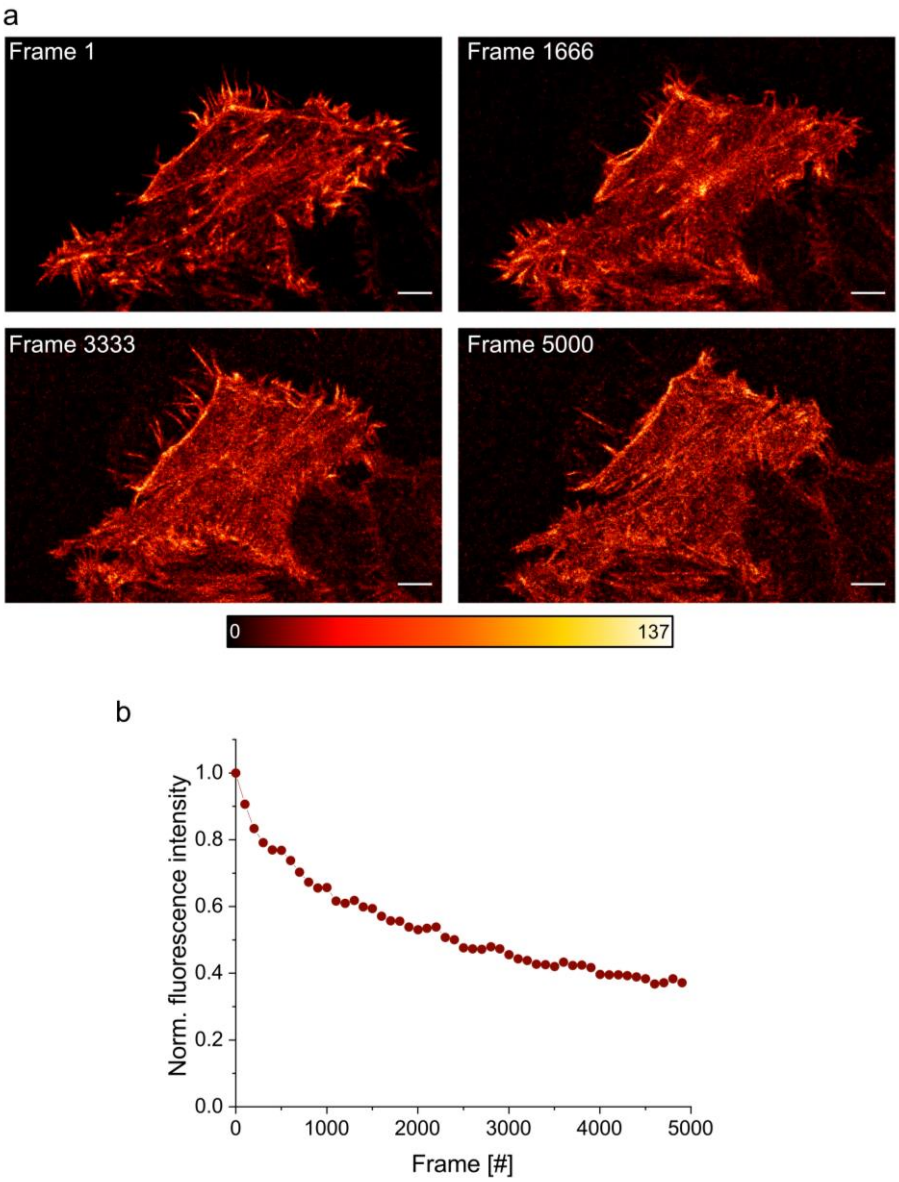

Figure 2.17: Photobleaching of PENELOPE under confocal conditions. *(a) 5000 consecutive images of LifeAct-PENELOPE expressing transiently transfected live HeLa cells were recorded. The presented images display selected frames of the recorded timelapse measurement. For better visualization, a bleaching correction based on a histogram matching algorithm was applied. (b) Normalized fluorescence intensity of the raw images plotted against the frame number. The fluorescence intensity was calculated as an average of the selected ROI and every 100th value was plotted. 25 µM. BV was added 2 h before imaging. Scale bar: 5 µm.*

2.6 Super-resolution imaging with PENELOPE in the NIR region

The good tagging quality of PENELOPE in conjunction with the previously determined switching parameters in *E. coli* and in vitro spectral characteristics suggested a successful application of PENELOPE in RESOLFT super-resolution microscopy in the NIR window. RESOLFT microscopy was performed on transiently transfected HeLa cells as well as in a stably expressing PENELOPE-cytokeratin18-Bxb1 landing pad cell line. In order to quantify the resolution improvement of super-resolution microscopy techniques, line

profiles with a width of three adjacent pixels were applied on single structures. The resulting plot profile was fitted with a Lorentzian peal function and the resulting full width at half maximum (FWHM) values were compared to the FWHM of the previously recorded confocal image.
PENELOPE was found to allow additional super-resolution microscopy techniques in the form of STED as well as an irradiation-saving pixel hopping RESOLFT approach. Furthermore, the switching mechanism of PENELOPE appeared to be resistant towards chemical fixation with paraformaldehyde. This is not the case for GFP-like RSFPs. This allows for novel applications for PENELOPE in super-resolution microscopy.

2.6.1 STED super-resolution imaging of cytokeratin18-PENELOPE

In 2018, a Wi-Phy based FP was engineered for the application in STED microscopy, namely the STED Near Infrared Fluoresent Protein (SNIFP) [121] . Even though PENELOPE was engineered for RESOLFT super-resolution microscopy, its photostability observed in confocal imaging justified exemplary measurements of STED in the NIR window. The utilized RESOLFT microscope was also equipped with a tunable STED laser, which allowed performing STED imaging with wavelengths in the NIR window. The microscope had previously been optimized for STED imaging with an 820 nm STED depletion laser by Dr. Florian Habenstein [142]. For this reason, exemplary measurements were performed with an 820 nm doughnut-shaped STED depletion beam (Figure 2.18). In order to reduce the detection of undepleted periphery photons, a detection delay was applied.

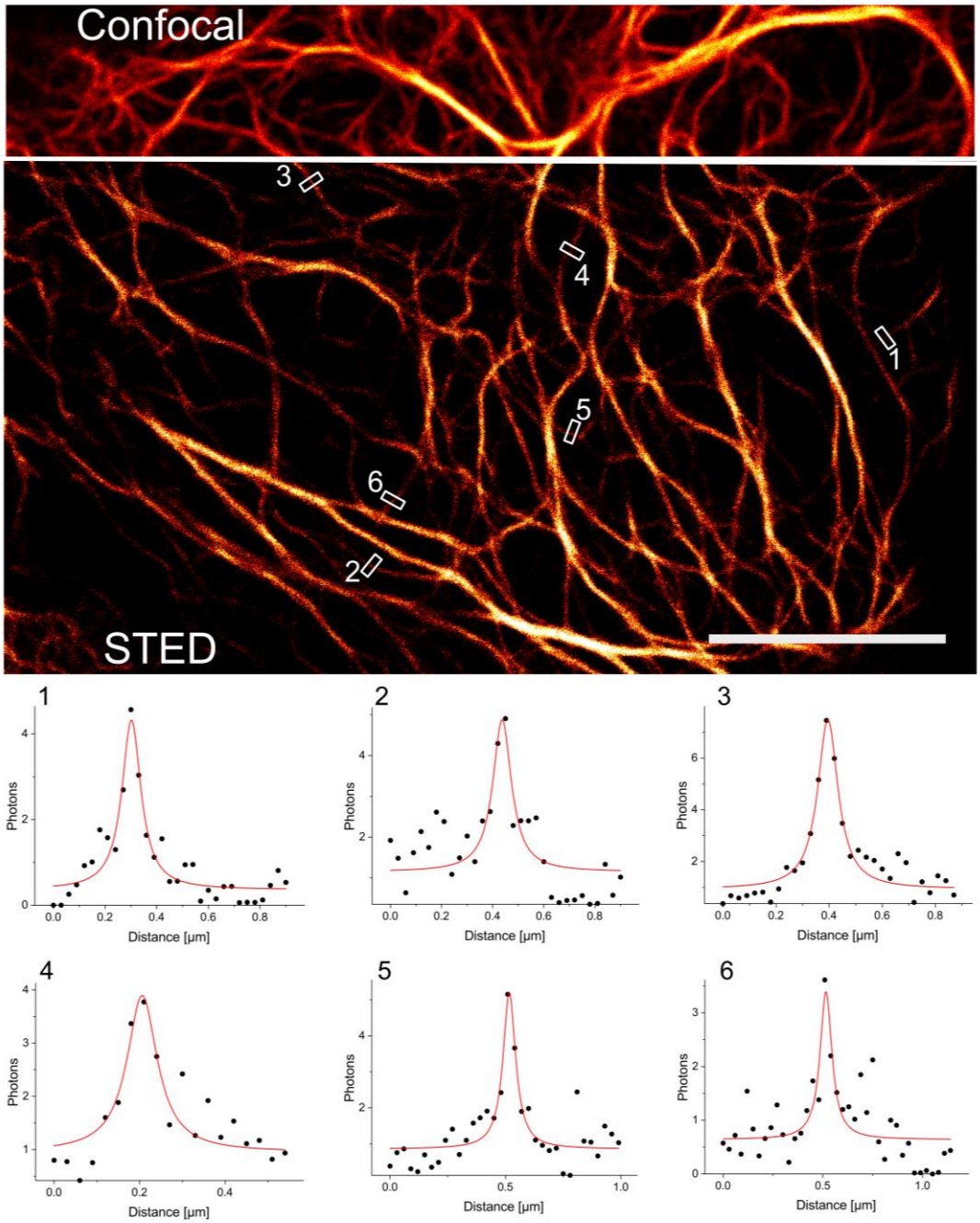

Lineprofile	1	2	3	4	5	6
STED FWHM [nm]	89	88	93	86	71	73

Figure 2.18: STED image of cytokeratin18-PENELOPE fusion constructs in transiently transfected HeLa cells*. Live HeLa cells were imaged with a 30 nm pixel size in line step mode. The confocal image was recorded prior to the STED image. 25 µM BV was added 2 h before imaging. Pixel dwell time: 30µs. Scale bar: 5 µm.*

2.6.2 RESOLFT with a single wavelength in mammalian cells

Initial RESOLFT microscopy experiments were performed with living transiently transfected HeLa cells. Successful imaging approaches consisted of an illumination scheme including a doughnut-shaped off-switching step, a Gaussian readout step and an illumination break allowing thermal relaxation of ensemble proteins. The lasers were applied sequentially and images were recorded pixel by pixel. A schematic representation of the applied switching times per pixel is depicted in Figure 2.19.

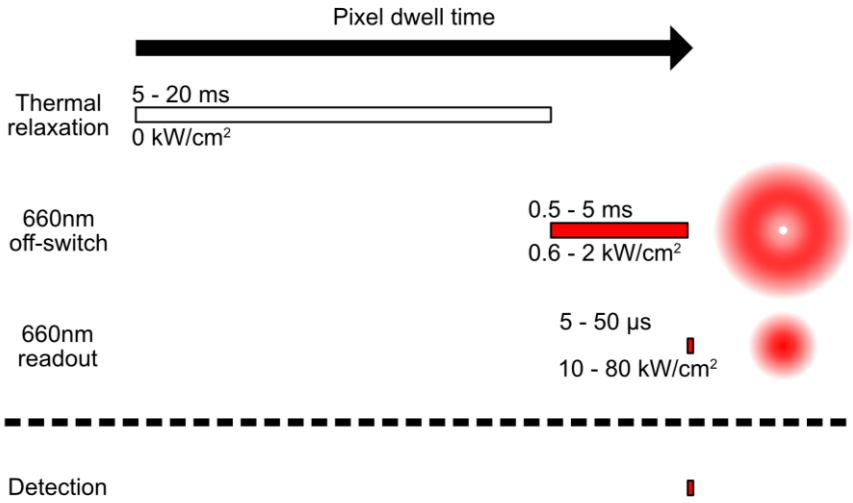

Figure 2.19: Single wavelength NIR RESOLFT imaging principle. *Graphical representation of the general illumination scheme for probing a single pixel in single wavelength NIR RESOLFT microscopy. The width of the single illumination steps indicates the relative time of the total pixel dwell time. Used laser intensities are placed below the single illumination steps.Used thermal relaxation times above the single illumination steps.*

Based on the kinetics observation of PENELOPE in *E. coli*, the marginal effect of the 785 nm on-switching step on transferring PENELOPE to the on-state was exchanged with an illumination break allowing for thermal relaxation of ensemble proteins back to the on-state. Despite the potentially increased fluorescence brightness of PENELOPE in a RESOLFT imaging scheme, high 785 nm laser powers applied for a millisecond time range would have had been required to detect a decisive effect. For many RESOLFT applications with negative switching RSFPs, the on-switching step bears a high phototoxic potential due to its UV-wavelength and occasional high laser powers. In order to strengthen the low interference nature of RESOLFT microscopy in living cells, RESOLFT super-resolution microscopy was performed for the first time with only a single wavelength by harnessing thermal relaxation of the chromophore to the fluorescent on-state.

2.6.3 RESOLFT microscopy with a single wavelength in transiently transfected mammalian cells

Successful application of this switching sequence was applied in live HeLa cells expressing a transiently transfected PENELOPE-LifeAct fusion construct. Figure 2.20 displays an overlay of a confocal image and a RESOLFT image. The confocal image was recorded prior to the super-resolved image and consisted of a 5 ms illumination break to allow for thermal relaxation of off-switched ensemble proteins and a 5 µs readout pulse with a laser intensity of 80 kW/cm^2. The RESOLFT image was recorded with an additional off-switching step prior to the readout step consisting of a 1.5 ms doughnut-shaped pulse with a laser intensity of 0.6 kW/cm^2. In order to obtain a sufficient amount of photons and signal-to-noise ratio, times line accumulation was performed 5 times. With the low laser intensity of the off-switching step, the RESOLFT image was recorded with a light dose of 6.375 kJ/cm^2 compared to 0.520 kJ/cm^2 for the confocal image. The achieved resolution improvements are depicted in Figure 2.20 below the super-resolved image. The FWHM of profiles across single filaments revealed a minimum width of 62 nm, which is on the limit of the Nyquist criterion with a pixel size of 30 nm. The comparison of the Lorentzian function fitted line profiles revealed a resolution improvement of 2 to 5-fold in 2D between the confocal and RESOLFT image. Deviations of the superposition of the confocal and RESOLFT line profiles are caused by mechanic drift or dynamic filament movements due to long image recoding times. Besides the exemplary depiction of a LifeAct fusion tag, RESOLFT images were also recorded for microtubule-bound protein EB3 and nucleoporin 50 (Nup50) (see appendix Figure 5.3 and Figure 5.4)

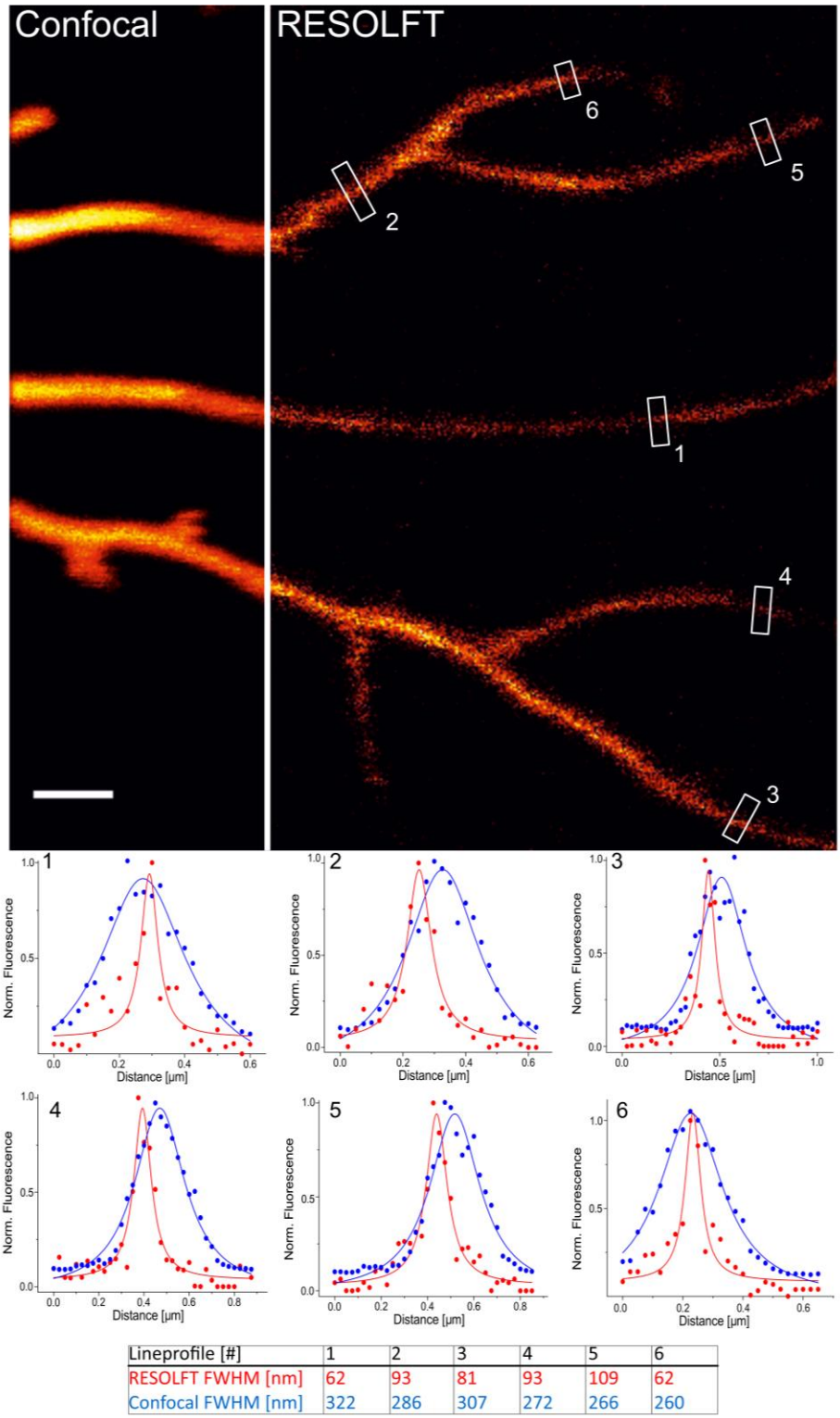

Lineprofile [#]	1	2	3	4	5	6
RESOLFT FWHM [nm]	62	93	81	93	109	62
Confocal FWHM [nm]	322	286	307	272	266	260

Figure 2.20: RESOLFT image of LifeAct-PENELOPE fusion constructs in transiently transfected HeLa cells. *Live HeLa cells were imaged with a 30 nm pixel size in pixel step mode. The confocal image was recorded prior to the RESOLFT image and was recorded with a pixel dwell-time of 5.01 ms which consisted of a 5 ms thermal relaxation break and a 10 µs 660 nm illumination with 103 kW/cm^2. The RESOLFT image was recorded with a sequential scheme consisting of a 5 ms thermal relaxation break, illumination with a 1.1 kW/cm^2 doughnut-shaped 660 nm off-switching laser for 1.5 ms and readout with a 103 kW/cm^2 Gaussian-shaped 660 nm laser for 5 µs. The presented line profiles were measured at 6 manually selected positions with a line width of 3 pixels. The data points were normalized and afterwards fitted with a Lorentzian function. The resulting FWHM values of the fit are displayed in the table below. 25 µM BV was added 2 h before imaging.Scale bar: 2 µm.*

After demonstrating successful RESOLFT super-resolution microscopy with a single wavelength in actin filopodia, cellular abundant cytokeratin18 was targeted. Figure 2.21 displays the overlay of the confocal and RESOLFT image. The applied illumination scheme complies with the scheme described for Figure 2.20 with the exception of the readout illumination, which consisted of a 15 µs 660 nm Gaussian illumination with an intensity of 82 kW/cm^2. Furthermore, line accumulation was not required anymore and therefore reduced the applied light dose to 1.275 kJ/cm^2 for the RESOLFT image. The line profiles of the manually selected super-resolved filaments are displayed below the image together with the respective FWHMs in the adjacent table. The smallest achieved FWHM of actin filopodia accounts for a width of 62 nm. Due to the high dependency of successful RESOLFT imaging on homogenous expression levels, a stably expressing cytokeratin18-PENELOPE cell line was established and allowed further optimization of the RESOLFT imaging protocol.

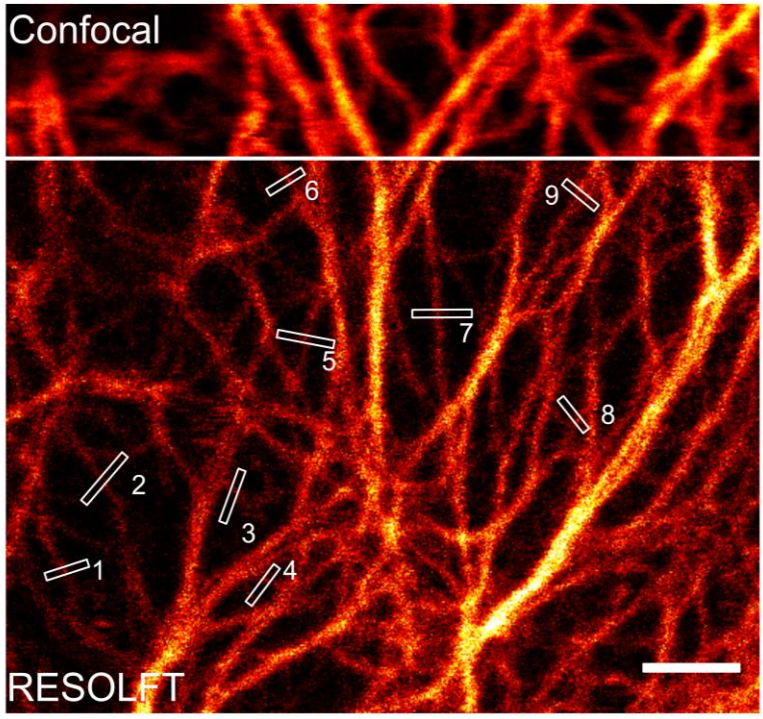

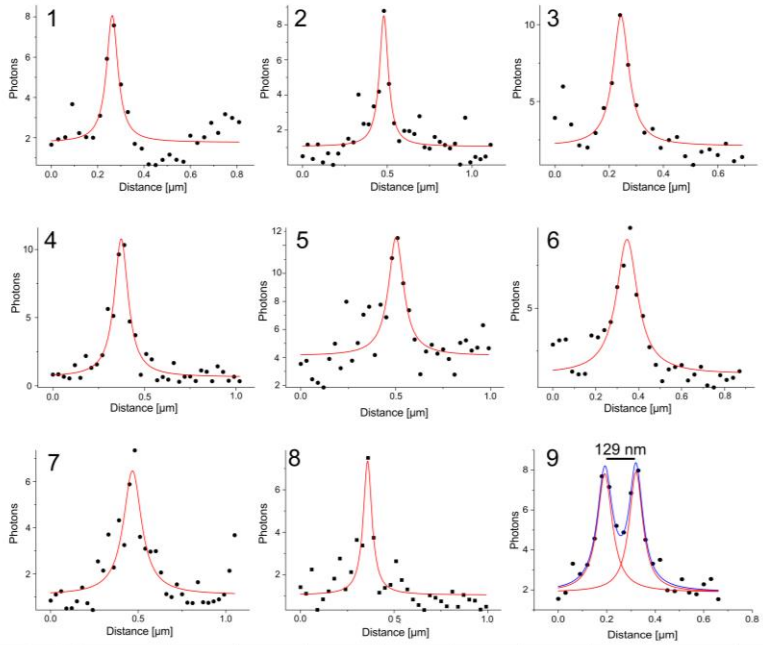

Lineprofile [#]	1	2	3	4	5	6	7	8	9
RESOLFT FWHM [nm]	60	69	70	91	95	125	119	62	75 + 68

Figure 2.21: RESOLFT image of cytokeratin18-PENELOPE fusion constructs in transiently transfected HeLa cells. *Live HeLa cells were imaged with a 30 nm pixel size in pixel step mode. The confocal image was recorded simultaneously to the RESOLFT image. The total pixel dwell-time accounted for 10.72 ms. This total pixel dwell time consisted of a 5 ms thermal relaxation break and a 15 µs 660 nm illumination with 82 kW/cm^2 to record the confocal image as well as a 5 ms thermal relaxation break, illumination with a 1.1 kW/cm^2 doughnut-shaped 660 nm off-switching laser for 1.5 ms and readout with a 82 kW/cm^2 Gaussian-shaped 660 nm laser for 15 µs to record the RESOLFT image. The presented line profiles were measured at 6 manually selected positions with a line width of 3 pixels. The data points were normalized and afterwards fitted with a Lorentzian function. The resulting FWHM values of the fit are displayed in the table at the bottom. 25 µM BV was added 2 h before imaging. Scale bar: 2 µm.*

2.6.4 RESOLFT microscopy with a single wavelength in a Bxb1-landing pad cell line

Since RESOLFT super-resolution microscopy in transiently transfected HeLa cells proved successful, the generation of a stably expressing monoclonal Bxb1 landing pad cell line was initiated. This cell line harboring a single landing pad element only allows incorporation of a single plasmid into the respective cell. This lowers the expression heterogeneity, which is often observed in transiently transfected cells. The integrated gene of interest is then controlled by a constitutive CAG promoter. An increased expression homogeneity of observed cells in conjunction with close to natural expression levels of the respective fusion protein creates a sufficient framework for optimizing RESOLFT schemes. With this, the possibility for imaging potential overexpression artifacts such as protein delocalization or altered cellular morphology were prevented. In addition, time-consuming transfection was eliminated and allowed a higher throughput of analyzing cells. Figure 2.22 displays the successful RESOLFT imaging of the stably expressing cytokeratin18-PENELOPE Bxb1 landing pad cell line. The cell line exhibited a higher number of cells with consistently distributed labeling of PENELOPE to the cytokeratin18 target structure. The image illustrates the beneficial effects of lower overall expression, as the fluorescent background from out of focus sections is lower and does thereby not affect the final resolution of single filaments. This can be observed in the plotted line profiles, which are also depicted in Figure **2.22**. The respective photon counts for confocal and RESOLFT structures can be observed on the y-axis and generally exhibit a 50% to 70% decrease of photon counts at filament centers in the RESOLFT image compared to the confocal image. The smallest FWHM for a single measurement was accounted for 63 nm in the RESOLFT image, compared to 279 nm in the confocal image. The applied illumination scheme allowed an illumination time decrease of the doughnut-shaped off-switching laser to 700 µs while maintaining the previously required laser intensity of 1.1 kW/cm^2. This reduces the light dose for RESOLFT image formation to 0.650 kJ/cm^2. To enhance the contrast, confocal and RESOLFT images were furthermore deconvolved with respective PSF sizes (see appendix Figure 5.5)

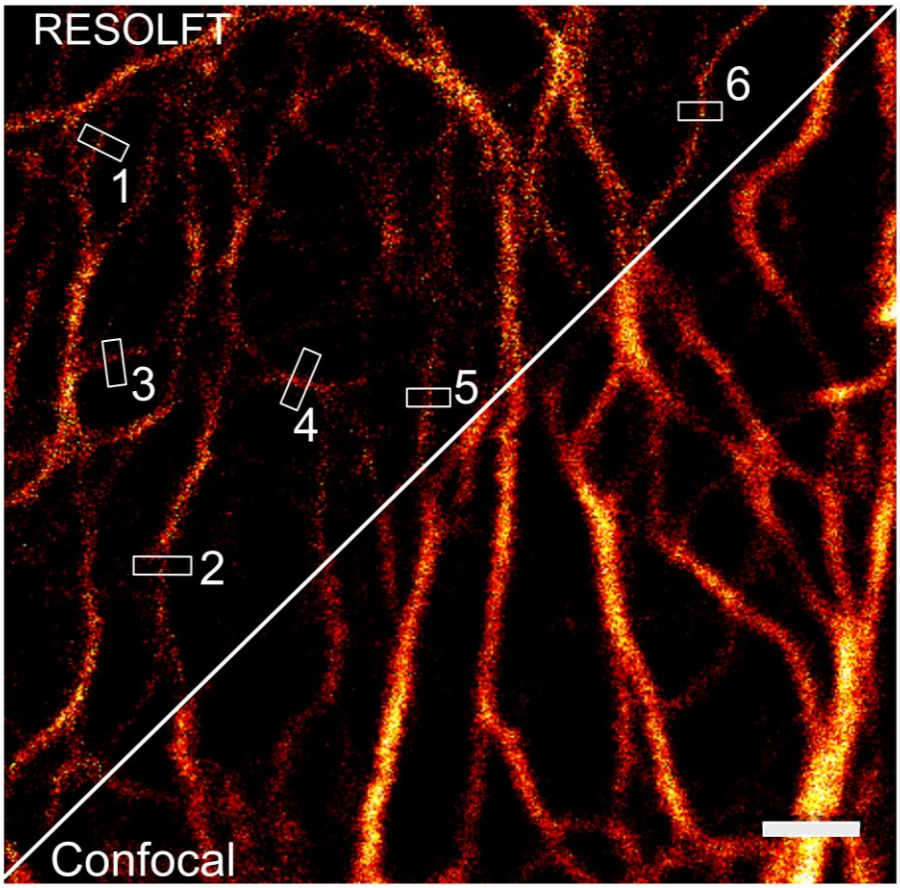

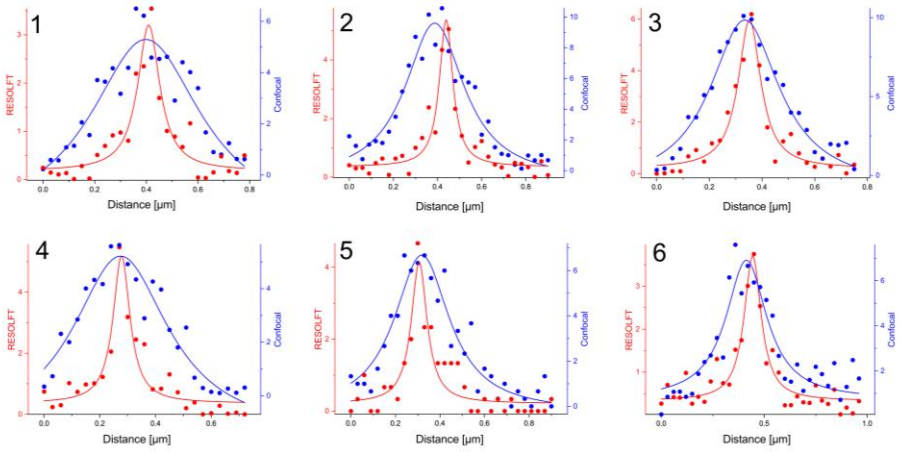

Lineprofile [#]	1	2	3	4	5	6
RESOLFT FWHM [nm]	91	74	104	63	85	100
Confocal FWHM [nm]	273	326	321	279	302	241

Figure 2.22: RESOLFT image of live stable Bxb1 landing pad cell line expressing cytokeratin18-PENELOPE. *Live HeLa cells were imaged with a 30 nm pixel size in pixel step mode. The confocal image was recorded simultaneously to the RESOLFT image. The total pixel dwell-time accounted for 10.72 ms. This total pixel dwell time consisted of a 5 ms thermal relaxation break and a 10 µs 660 nm illumination with 103 kW/cm^2 to record the confocal image as well as a 5 ms thermal relaxation break, illumination with a 1.1 kW/cm^2 doughnut-shaped 660 nm off-switching laser for 700 µs and readout with a 103 kW/cm^2 Gaussian-shaped 660 nm laser for 10 µs to record the RESOLFT image. The presented line profiles were measured at 6 manually selected positions with a line width of 3 pixels. The data points represent the respective photon counts and were fitted with a lorentzian function RESOLFT data points and fits are colored in red, confocal data points and fits are colored in blue. The resulting FWHM values of the fit are displayed in the table below. 25 µM BV was added 2 h before imaging. Scale bar: 2 µm.*

2.6.5 RESOLFT microscopy with a single wavelength in fixed cells

The main application of RESOLFT microscopy, as introduced in section 1.2.4, is super-resolution microscopy in living cells. However, with emerging relevance of correlative light and electron microscopy (CLEM) imaging approaches, usage of dyes, which maintain their photophysical properties under live and fixed cell conditions, appears crucial. In 2015, Ilgen et al. published a fusion construct consisting of an antibody-binding Z-domain and rsEGFP2, which allowed RESOLFT imaging of previously fixed cells [143]. However, RESOLFT imaging of genetically tagged fixed cells was not performed. With the development of PENELOPE which exhibited a new chromophore and a new chromophore environment, RESOLFT imaging attempts appeared justified.

Figure 2.23 displays the successful RESOLFT imaging of the stably expressing cytokeratin18-PENELOPE Bxb1 landing pad cell line fixed with formaldehyde.
The imaging protocol followed the same sequence, laser intensity and illumination duration as applied for Figure 2.22. Thermal relaxation and off-switching kinetics were observed for fixed cells and compared to the respective live cell observed kinetics (see appendix Figure **5.10**).

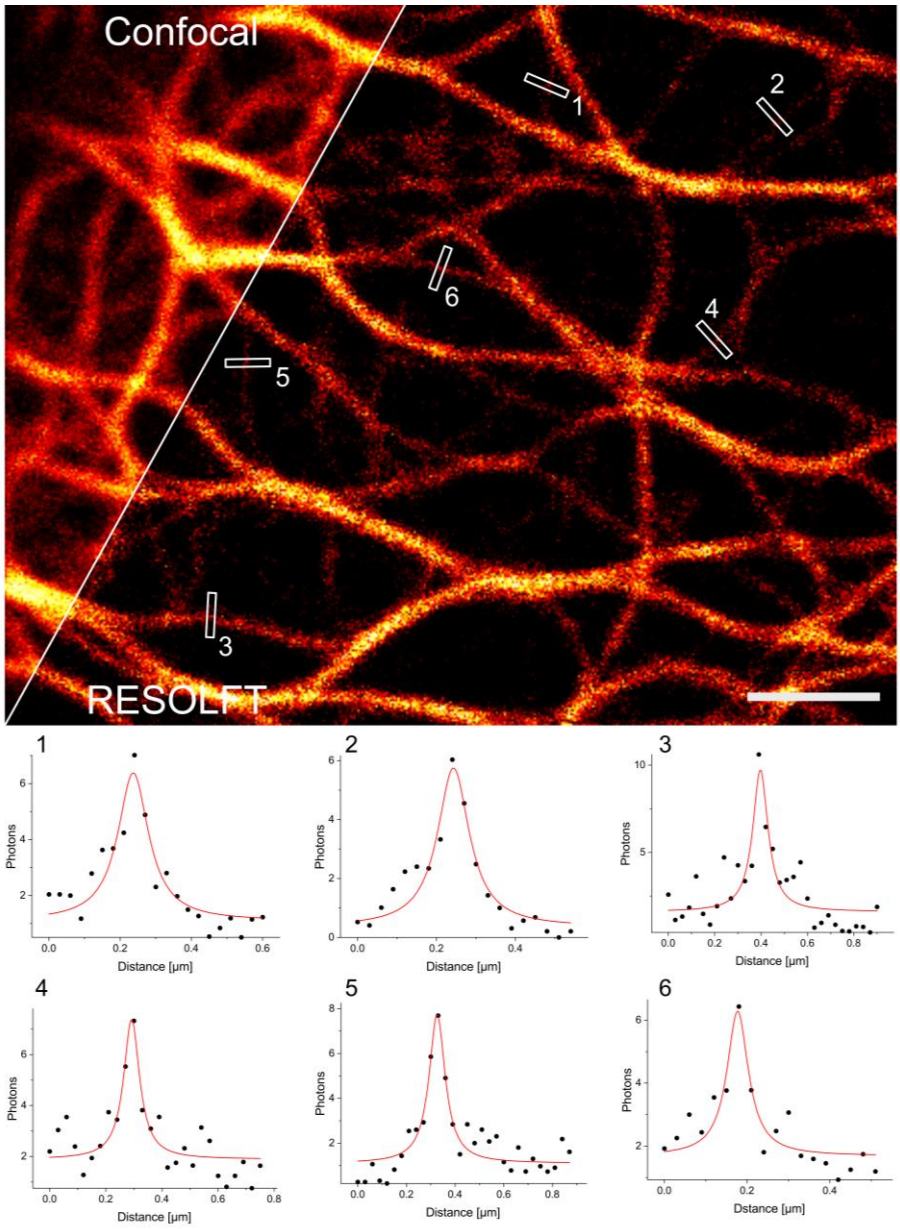

Lineprofile [#]	1	2	3	4	5	6
RESOLFT FWHM [nm]	105	98	79	69	80	63

Figure 2.23: RESOLFT image of formaledhyde fixed stable Bxb1 landing pad cell line expressing cytokeratin18-PENELOPE. *Formaldehyde fixed HeLa cells were imaged with a 30nm pixel size in pixel step mode. The confocal image was recorded simultaneously to the RESOLFT image. The total pixel dwell-time accounted for 10.42 ms. This total pixel dwell time consisted of a 5 ms thermal relaxation break and a 10 µs 660 nm illumination with 103 kW/cm^2 to record the confocal image as well as a 5 ms thermal relaxation break, illumination with a 1.1 kW/cm^2 doughnut-shaped 660 nm off-switching laser for 400 µs and readout with a 103 kW/cm^2 Gaussian-shaped 660 nm laser for 10 µs to record the RESOLFT image. 25 µM BV was added 2 h before imaging. Scale bar: 2 µm.*

2.6.6 RESOLFT microscopy with a single wavelength in a time-saving pixel hop mode

The single wavelength RESOLFT microscopy protocols presented in this work so far share a major disadvantage of this low light dose super-resolution microscopy approach. The thermal relaxation step accounts for up to 87 % of the total pixel dwell-time required for the generation of a super-resolved image. Further, an elongation of this step would increase the overall image quality at the expense of an even prolonged pixel dwell time. However, despite its necessity in the pixel step mode, the thermal relaxation step is an undesirable waiting period. This waiting period can be harnessed to record image areas, which have been previously unaffected by the applied lasers. This was realized by applying the doughnut-shaped off-switching beam followed by the Gaussian readout beam on previously determined x-axis positions accounting for at least half the distance of the doughnut-shaped off-switching PSF away from the previous position. Reaching the end of the x-axis scan range, the scanner will target again the previously first x-position but with an additional offset matching the desired pixel size. A single image is recorded upon filling up the whole distance between consecutive x-positions with single pixel steps in this interleaved scanning scheme. The custom axis implemented in the commercially available Imspector software by Abberior Instruments allows creating such an offset within the x-axis matching the desired pixel size. This protocol is repeated until all pixels of the image have been probed (Figure 2.24). The interface connection between Imspector and a self-written Python program developed by Dr. Jan Keller-Findeisen allowed the formation of the single image out of the single offset frames. This approach should allow the improvement of recording speed by increasing the area size along the x-axis of the respective region of interest that can be recorded within a certain time.

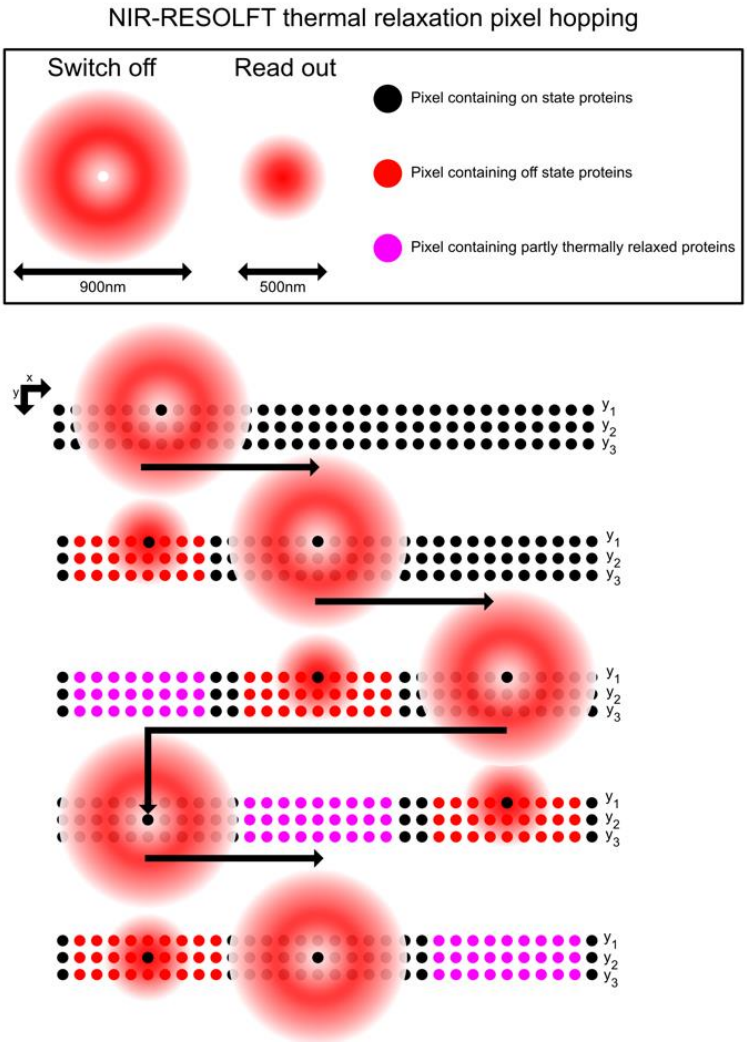

Figure 2.24: Single wavelength NIR pixel hop RESOLFT imaging principle. *Graphical representation of the general illumination scheme for performing single wavelength NIR RESOLFT without a pixel-dwell time contributing thermal relaxation step. This is achieved by applying the off-switch and readout illumination stepwise along the x-axis along distances, which have previously not been illuminated by either of the lasers. Upon return of the illumination pattern, proteins have thermally relaxed to the fluorescent on-state and can be again illuminated with the doughnut off-switching and readout pattern.*

The application of this newly developed imaging protocol is presented in Figure 2.25. Imaging of the confocal and RESOLFT image of formaldehyde-fixed stable Bxb1 landing pad cell line expressing Cytokeratin18-PENELOPE resulted in an improved resolution. However, only few single filaments showed limited resolution improvement accounted for FWHMs of ~100 nm. This limited resolution improvement could be caused by insuffcient positioning of the laser beam position as a consequence of the large distances covered for each pixel hop step.

The confocal image was recorded prior to the super-resolved image and consisted of a 470 µs step without any illumination and a 30 µs 660 nm Gaussian illumination with 42 kW/cm^2 for the readout. The RESOLFT image was recorded by activating the doughnut-shaped 660 nm laser with an intensity of 1.1 kW/cm^2 during the 470 µs illumination step and subsequent readout for 30 µs with a 660 nm Gaussian illumination

with 42 kW/cm^2. For the formation of confocal and RESOLFT images, additional 50 µs steps before and after the illumination protocol were added to increase the probability for correct scanner positioning. The pixel dwell time applied for pixel hop RESOLFT accounted for 550µs and thereby allows a 10-fold faster image formation than stepwise scanning. Potential causes limiting the resolution increase compared to stepwise scanning will be discussed in section 3.4.2.

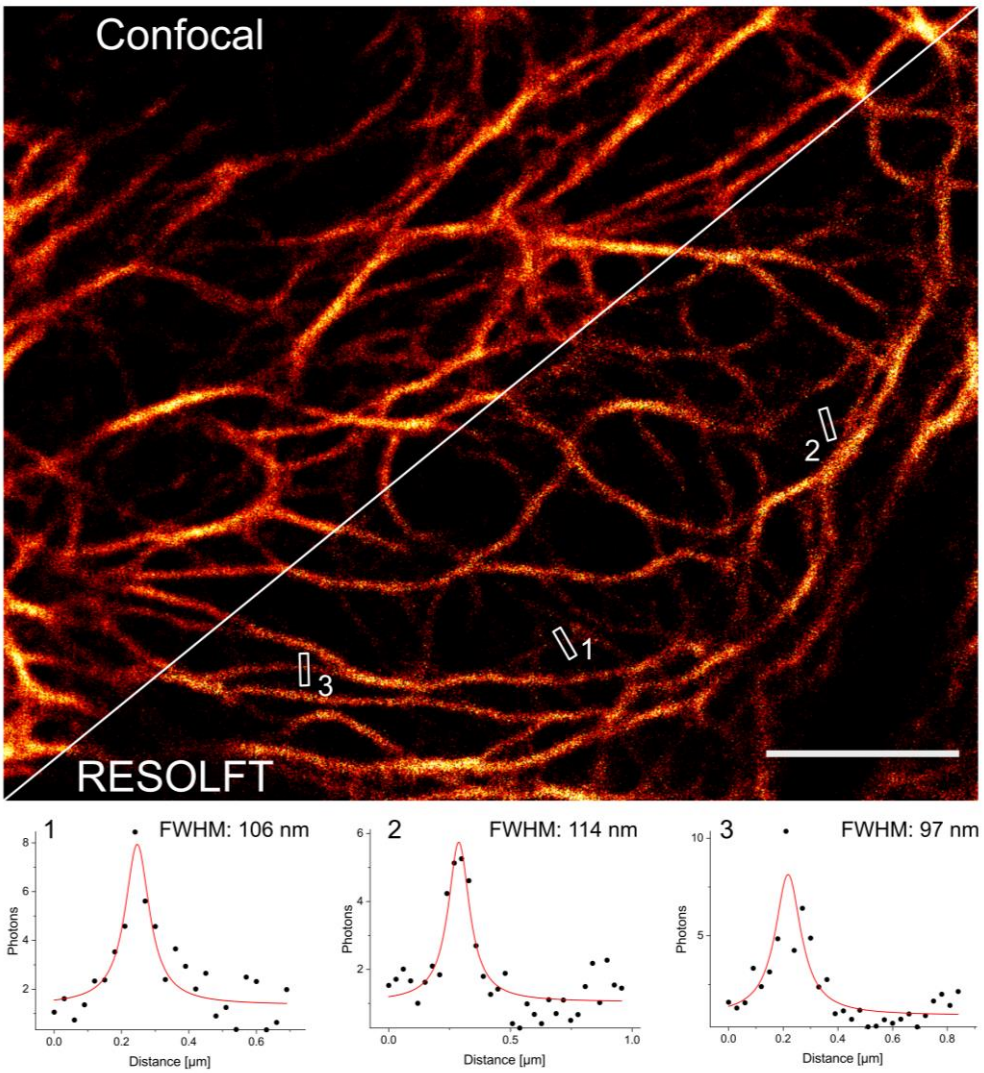

Figure 2.25: RESOLFT image of formaldehyde fixed stable Bxb1 landing pad cell line expressing Cytokeratin18-PENELOPE in pixel hop mode. *Formaldehyde fixed HeLa cells were imaged with a 30 nm pixel size in pixel step mode. The confocal image was recorded previously to the RESOLFT image. The pixel dwell-time for confocal imaging accounted for 600 µs. This pixel dwell time consisted of a 470 µs additional thermal relaxation break and a 30 µs 660 nm illumination with 42 kW/cm^2 to record the confocal image. Additional 50 µs at the start and end of the pixel dwell-time allowed the scanner to reach the next positions. The pixel dwell-time for RESOLFT imaging accounted for 600 µs. This pixel dwell-time consisted of illumination with a 1.1 kW/cm^2 doughnut-shaped 660 nm off-switching laser for 470 µs and readout with a 42 kW/cm^2 Gaussian-shaped 660 nm laser for 30 µs to record the RESOLFT image. Additional 50 µs at the start and end of the pixel dwell-time allowed the scanner to reach the next positions. 25 µM BV was added 2 h before imaging. Scale bar: 5 µm.*

2.7 Switching kinetics of PENELOPE in living mammalian cells

For GFP-based negative switching RSFPs such as rsEGFP2, long-time off-switching or off-switching with high laser intensities results in a low residual fluorescence. This residual fluorescence was shown to reach an equilibrium after sufficient off-switching time durations until photobleaching effects start to rise. In addition, a steady rise in switching rate kinetics can be observed from laser intensities ranging from 0-25 kW/cm^2 and presumably beyond this range. For intensities I<5 kW/cm^2, switching rates amount for decay rates smaller than 10^4 decays per second. Since kinetics experiments in *E. coli* suggested a different behavior for PENELOPE, general switching kinetics were investigated with the confocal setup in living mammalian cells. The laser and detection control were facilitated by a 9420 series pulse generator.

Figure 2.26 illustrates the effect of thermal relaxation and of different laser intensities on the residual fluorescence and switching rate constants in mammalian cells. Figure 2.26a displays the thermal relaxation kinetics of PENELOPE in mammalian cells. Plotted data points represent the ratio of on-state molecules after the respective thermal relaxation time. The fitted cumulative distribution function reveals a thermal relaxation halftime of 5.96 ms. This means that 50% of previously off-switched proteins thermally relaxed back to the on-state after 5.96 ms. To achieve on-state fractions of 90 % and 95 %, thermal relaxation times of 13.8 ms and 19.9 ms would be required.

For Figure 2.26b,c, a narrow range of laser intensities from 0.01 kW/cm^2 to 3 kW/cm^2 was applied. In contrast to previously discussed rsEGFP2, an early saturation of the apparent switching rate at low laser intensities I < 1 kW/cm^2 was observed. Interestingly, residual fluorescence reached a minimum at laser intensities I < 1 kW/cm^2. This can prove beneficial for RESOLFT imaging as it favors low laser intensities to reach a low residual fluorescence for the off-switching of the ensemble periphery. At the same time, early saturation of the switching rates allows to perform a high laser intensity readout allowing a high photon collection while only switching a fraction of the center proteins to the non-fluorescent off-state. For the residual fluorescence, an early saturation at 0.2 kW/cm^2 was observed at a residual level at ~ 5% (Figure 2.26b), which is lower than values observed for investigated *E. coli* cells in the automated screening setup (section 2.3.3). The minimum fluorescence decay halftime of 70.9 µs is observed at 1.6 kW/cm^2 (Figure 2.26c).

The saturation of the off-switching half time at low light intensities differs from GFP-like negative-switching RSFPs, which, in the case of rsEGFP2, show a positive correlation between applied laser intensity and off-switching half time. This difference implies the presence of an additional fluorescence state. This intermediate state would be accessed from the on-state via a light-driven process and transitioned to the off-state via a thermal process. The transition to the on-state would be achieved solely by a thermal process or a synergy of

the thermal and a light-driven process (Figure 2.26d). This model will be further discussed in section 3.5.

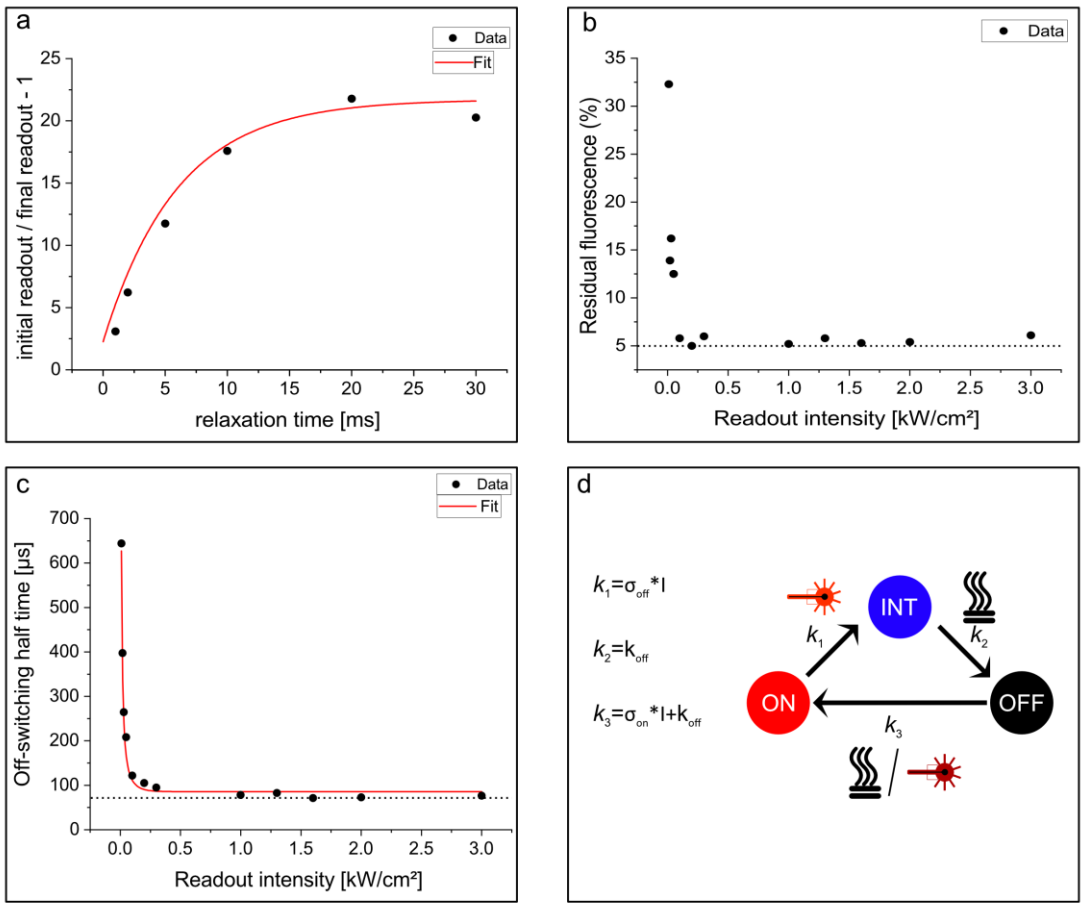

Figure 2.26: Thermal relaxation and laser intensity effects on residual fluorescence and switching rate kinetics in mammalian cells in a confocal setup. *(a) Recovered fluorescence brightness as a function of relaxation time. The protocol consisted of repeated application of a 0.21 kW/cm²660 nm Gaussian-shaped laser for 3 ms. Between each repetition, a varying time for thermal relaxation was implemented. (b) Residual fluorescence as a function of low to medium laser intensities. The protocol consisted of the application of a 0.21 kW/cm²660 nm Gaussian-shaped laser for 3 ms Minimum residual level is indicated by dashed line. (c) Off-switching half time as a function of low laser to medium laser intensities. The protocol consisted of the application of a 0.21 kW/cm²660 nm Gaussian-shaped laser for 3 ms Minimum residual level is indicated by dashed line. Experiments were performed on a predefined area of 16 µm². Analysis of experiment data was done by Dr. Jan Keller-Findeisen. (d) Proposed fluorescent state switching model of PENELOPE based on kinetics measurements conducted under confocal conditions. A three state model is assumed, with a fluorescent on-state (ON), a non-fluorescent off-state (OFF) and a fluorescent intermediate state (INT). Assumed switching kinetics are indicated with σ as the cross-section, I as the light intensity and k as the respective rate constants.*

3 Discussion

Until recently, super-resolution microscopy with fluorescent proteins in living cells was limited to the visual electromagnetic spectrum. With the development of bacteriophytochrome-derived FPs such as SNIFP [121] and emIRFP703 [124] for STED microscopy, the spectral window of FP-based super-resolution microscopy immediately widened. In this work, the toolbox of accessible super-resolution microscopy methods for bacteriophytochrome-derived FPs was expanded to the low light intensity regime. The development of the *Deinococcus radiodurans* based PhotostablE Nir rEversibly switchabLe fluOrescent ProtEin (PENELOPE) allowed for the first time RESOLFT super-resolution imaging in the NIR window. This was accomplished by only using a single wavelength. Besides its successful application in super-resolution microscopy, this work thoroughly characterized PENELOPE in different environments and under varying imaging conditions. PENELOPE's unique switching was the driving force to develop a switching model, which significantly differs from the switching model of conventional RSFPs.

3.1 Parameter improvement for the generation of a bacteriophytochrome-derived RSFP for RESOLFT microscopy

The inherent natural photocycle of bacteriophytochromes with distinct absorption-states suggests a high potential for their use as fluorescent proteins in microscopy methods that harness the accessibility and transitioning between these states. Due to their low quantum yield, many bacteriophytochrome-derived FPs have been engineered to arrest the Pr-state and improve the fluorescence by suppressing respective non-fluorescent states. In this thesis, the truncated Wi-Phy version W3.50, which exhibited a reestablished photocycle [104, 133] was mutated to improve its photophysical properties in order to allow its usability for RESOLFT super-resolution microscopy. Site-directed and random mutagenesis resulted in a mutant library. Three W3.50 successors were further characterized, including the final variant PENELOPE. This section will discuss the properties of the single variants and provide an assessment for the application in RESOLFT microscopy (see table 2.1).

3.1.1 W3.50

The application of *Deinococcus radiodurans*-based FPs in microscopy has been limited to the constitutively fluorescent proteins IFP1.4 [90], IFP2.0 [144] and SNIFP [121], so far. An additionally developed *D. radiodurans* FP was Wi-Phy [104]. However, Wi-Phy was not used for imaging, despite its superior fluorescence over IFP1.4. The fluorescence increase was caused by the Y263F mutation and can be explained by a suppressed photoconversion [104]. In W3.50, this photoconversion was reintroduced by reversing the Y263F mutation and allowed its photoswitching [133]. However, the observed fluorescence traces indicate an impaired switching from the off-state to the on-state compared to the on-

switched initial equilibrium state. The fluorescence brightness at illumination cycle 1 exhibits a 42 % increase over the fluorescence brightness at illumination cycle 2. This behavior is highly restrictive for RESOLFT microscopy. An initial 30 % loss of fluorescence signal for once illuminated ensemble proteins lowers the achievable contrast ratio and furthermore reduces the number of photons that can be detected. Since RESOLFT image formation inherently requires repeated illumination of ensemble proteins, W3.50 is already conceptionally limited. In comparison to its successors, W3.50 moreover exhibits unfavorably low fluorescence brightness along with high residual fluorescence and slow on-switching kinetics. The displayed switching fatigue is strongly influenced by the initial fluorescence brightness loss and does therefore only have limited informative value. The minimum off-switching halftime of W3.50 accounts for 65 µs and thereby outperforms its successors. However, along with its previously characterized unfavorable properties, W3.50 is not suitable for RESOLFT super-resolution microscopy.

3.1.2 V10

The introduction of the M174F mutation in V10 allowed to reduce the impaired photoconversion and resulted in a more stable switching. The achievable brightness of the protein ensemble on-state transferred by photoinduced on-switching as well as thermal relaxation from the off-state was more stable during first switching cycles.
The amino acid 174 is located in close proximity to the BV D-ring, which cis-trans-isomerization is the expected key step in switching between on and off-states [145]. The exchange of methionine to phenylalanine was performed with the assumption that potential stacking-effects of the phenylalanine aromatic ring with the BV D-ring could increase the metastability of the off-state to suppress the thermal relaxation. A suppression of the thermal relaxation step was not observed but a stronger distinction between the 785nm induced on-state and the thermal relaxation induced on-state was possible. V10 showed a fluorescence brightness increase to W3.50, which was especially pronounced for higher laser intensities. This effect was not expected for this mutation but proved beneficial. The resistance to switching fatigue is increase by a factor of ~ two compared to W3.50. This is seemingly caused by suppressing the fluorescence brightness decrease after the first switching cycle. The fast off-switching speed follows the trend of W3.50 and does not exhibit a strong power-dependency, as it can be observed in GFP-like RSFPs. Due to the increased residual fluorescence of up to 12.5 %, V10 cannot be used in RESOLFT microscopy. However, allowing the reproducibility of the switching cycles and thereby improving the switching fatigue allowed to focus on advancing the two key parameters fluorescence brightness and residual fluorescence.

3.1.3 V30

Since targeting the close proximity of the BV D-ring proved to provide significant changes of V10 compared to the template W3.50, site-directed mutagenesis was continuously applied. This resulted in a large BpRSFP-library, of which 36 variants showed improved parameters. These 36 variants were subsequently sequenced and characterized. Within these variants, V30 showed major improvements to V10 while only exhibiting a single additional mutation. In V30, the alanine at position 288 was mutagenized to a valine. Both amino acids are small and hydrophobic. Due to its aliphatic side chain, valine exhibits a slightly higher extension over alanine. Based on crystal structure analysis, this extension is directed towards the BV C- and D-ring and thereby increases the interaction probability. The carboxyl and methyl groups of the BV C-ring could allow a repulsion of BV from the cavity-surrounding environment as well as an attraction to it. The D-ring methyl group position is strongly affected by the conformational state of the D-ring and would lead to a repulsion in the case of a close proximity to V288 [146]. The switching cycle reproducibility was unaffected by the V288 introduction. However, thermal relaxation to the on-state after 20 ms accounted for a 50 % increase of fluorescence brightness compared to V10. Among the 36 observed site-directed mutagenized variants, an increased metastability of the off-state could not be observed. The site-directed mutagenesis screening did not result in any variants exhibiting an increased off-state metastability. This observation initiated a shift in the screening process, which henceforth favored variants with fast thermal relaxation kinetics and would ultimately allow performing RESOLT microscopy without a laser-dependent on-switching step. In conjunction with its fast thermal relaxation kinetics, V30 exhibited a fluorescence brightness increase by a factor 2 and furthermore achieved residual fluorescence levels below 10% at high off-switch laser intensities. Its superior resistance to switching fatigue of 539 cycles justified the first experimental applications for RESOLFT microscopy in living mammalian cells. These first tries did not allow significant resolution improvements. This could be explained by a comparatively high residual fluorescence. For this reason, the screening process was readjusted to identify BpRSFPs with a low residual fluorescence while maintaining fast thermal relaxation kinetics.

3.1.4 PENELOPE

Site-directed mutagenesis in the direct proximity of the chromophore did not result in significantly improved variants after the development of V30. For this reason, the mutagenesis protocol was changed to introduce random mutations over eight rounds via error-prone mutagenesis. Over the course of this directed evolution approach, the 100th variant that was later referred to as PhotostablE Nir rEversibly switchabLe fluOrescent ProtEin (PENELOPE), was generated. PENELOPE exhibited the lowest residual fluorescence with 6 % of the presented BpRSFPs, which balanced its fluorescence brightness decrease of 16 % compared to V30. A fluorescence brightness decrease can be either caused by alteration of the amino acid environment of the bound chromophore or a

decreased BV affinity [123]. In conjunction with increased thermal relaxation kinetics, improved off-switching and a repeatedly accessible fluorescent on-state, PENELOPE showed desirable RESOLFT properties. In contrast to V10 and V30, parameter improvement cannot be traced back to a single amino acid substitution. In comparison to V30, PENELOPE exhibits mutations G46V, R265W and T227A. W265 and A227 are located in medium proximity of around 12 Å around the chromophore, whereas V46 has a direct distance to the chromophore of 30 Å. These distances do not indicate a direct effect of substiuted amino acids on the chromophore. However, W265 is loctaed in an α-helix structure that is located within a 5 Å distance to the flexible linker residing A227. This α-helix structure also covers the crucial Y263 position, which is required to sustain the inherent photocycle. Hence, spatial alterations of the helix structure caused by interacting W265 and A227 potentially leads to a change in the direct chromophore environment. Due to the lower resdiual fluorescence and fluorescence brightness, a loosened packaging of the chromophore due to a spatially enlargened chromophore pocket around the BV D-ring is possible [147, 148]. The observed changes of protein characteristics in response to single mutations and the derived conclusions remain speculative due to a scarcity of scientific publications dealing with bacteriophytochrome-derived FPs exhibiting a natural photocycle. Furthermore, novel structural elements and amino acid interactions are likely to have occurred during mutagenesis. Structure determination using x-ray crystallography could elucidate this.

Following the generation of PENELOPE, further mutants were generated and analyzed. 37 additional variants showed a variety of improved switching characteristics. However, early-stage confocal imaging of a subset of these variants, including V112, V130 and V135 (see appendix Figure 5.2), showed an impaired tagging quality in cytoskeletal structures. These variants share a common mutation on position 9, which substituted a leucin against a phenylalanine. The phenotypical structures indicated an advanced oligomerization tendency and therefore prohibited the further use of these variants. This effect appears counterintuitive at first sight since the dimerization interface is located on the opposite lateral site of the protein [104]. However, the higher incidence of hydrophobic amino acids surrounding position 9 (L6/P7/F8/L9/P10/P11/12L/Y13), which partly resembles the dimerization interface of the wildtype bacteriophytochrome (R310/L311/L312/S313/L314/Q315/V316/ Q317) could hint to a potential formation of a new dimerization interface. This undesirable effect cannot be observed in the applied screening system in *E. coli*. This highlights the necessity for regular evaluation of tagging performance in mammalian cells between mutation cycles.
Interestingly, directed evolution over 8 rounds only yielded minor improvements of critical parameters such as residual fluorescence. In contrast to GFP-based RSFPs such as rsFastLime, Dronpa-M159T [64] and rsEGFP2 [47], key mutations allowing kinetic parameter improvement by a factor of 10-1000 to predecessor variants were not observed. Of course, this could be a stochastic event. However, this could also indicate a higher spatial integrity in the interaction between the chromophore and its environment compared to

GFP-based RSFPs. An adaptation of the mutagensis approach to shift towards multiple site-directed mutagenesis could also lead to the generation of a library with more hit counts. Consequently, a detailed crystallographic analysis of PENELOPE in its fluorescent on- and non-fluorescent off-state could provide valuable information on the underlying structural rearragements compared to constitutively fluorescent bacteriopytochrome-derived FPs. Crystallographic insights could furthermore resolve whether the non-fluorescent state resembles the natural Pfr-state or if the photocycle of PENELOPE occupies a previous or diverging state. The ms-range in which PENELOPE achieves thermal relaxation to the on-state indicates a fundamentally different photocycle as this process exhibits duration on the minute- to hour-range in naturally occuring bacteriophytochromes.

3.2 The BpRSFPs Off-state to On-state transition

Initially, the screening for the development of suitable NIR-RESOLFT microscopy BpRSFPs aimed at selecting BpRSFPs with a conventional on-switching step. In GFP-based negative switching RSFPs, the on-switching step can have a high switching quantum yield of ~ 0.1 [136]. This allows for fast and complete on-switching with a Gaussian on-switching beam of the central ensemble proteins within 70-500 µs using light intensities of several kW/cm^2. However, the utilized on-switching wavelengths used for RESOLFT microscopy are typically in the UV or blue region of the spectrum, with 365 nm for Dreiklang [149], 430 nm for rsCherryRev1.4 [150] and 405 nm for other RSFPs [151-153]. In conjunction with the required moderate to high laser powers (0.8 kW/cm^2 – 24 kW/cm^2), the on-switching step bears potential phototoxicity risks in live cell imaging. In contrast, BpRSFPs used in this work, are entirely switched in the NIR-region. In addition, the on-switching wavelength is bathochromic to the off-switching wavelength. However, a negative side effect observed with this favorable feature was the slow switching efficiency and switching speed. Adequate switching to the on-state was achieved only after 20ms with high laser intensities. Interestingly, the on-switched protein ensemble equilibrium state of the starting template W3.50 exhibited a 42 % increase of the fluorescence brightness than the protein ensemble switched on from the off-state in the following switching step.
One explanation might be that equilibrium state FPs are more susceptible for 785 nm on-switching than off-state FPs. It is likewise conceivable that the majority of FPs in the unprobed equilibrium state account for on-state proteins. In this case, an on-switching effect of 785 nm light could not be separated from the equilibrium state. A 660 nm light induced transition of a FP fraction to long-lived triplet states is a further possibility, which could be verified via Fluorescence Correlation Spectroscopy (FCS) [154]. Furthermore, Auldridge et al. published in 2013, that Y263 might act as an opposing force for BV A-ring interaction of H207 by creating a hydrogen bond to H207. Structural changes of BV induced by high laser intensities could disrupt this weak interaction in a fraction of FPs and thereby lead to this alternating photoconversion [104].
At this point, thermal relaxation to the on-state was already observed and reached ~70 % of the light-induced on-state. Mutation M174F caused a thermal relaxation speed decrease,

while allowing repeated transition between the initial and subsequent on-states. Over the course of the adjacent screening process, a further suppression of the thermal relaxation speed was not achieved. Simultaneously, on-switching kinetics could also not be increased over the course the screening.
Consequently, the screening process was adjusted to rate BpRSFPs with fast thermal relaxation kinetics higher. Interestingly, the repeatable transition between initial and subsequent on-states shifted over the course of mutagenesis. Repeated switching cycles resulted in a fluorescence increase within the first five switching cycles for variants V30 and PENELOPE. This is beneficial for RESOLFT microscopy, as RSFPs are repeatedly switched. For the GFP-like RSFP Padron, a bright intermediate state was observed, which might be responsible for a comparable behavior in subsequently generated Padron variants [155]. For PENELOPE, it is likewise conceivable that multiple fluorescent and non-fluorescent states are present.

3.3 Biophysical characterization of PENELOPE

In vitro absorption spectra of PENELOPE revealed distinctive on- and off-sates, visible by the shift in the Q-band. The overnight equilibrium state showed a high resemblance with the on-switched state and only exhibited a minor absorption decrease. Similar behaviors were found for GFP-like RSFPs rsEGFP2 and Padron2 [156]. However, the off-state absorption peak of PENELOPE accounted for 50% of the on-state absorption peak. In GFP-like RSFPs, the ratio of on-state peak to off-state peak approximates residual fluorescence observed in kinetics measurements in *E. coli*. For PENELOPE, this would require a further reduction down to ~6%. At the chosen 660nm light intensities, a further absorption peak reduction after 180s was not observed. This effect might be due to the presence of a high fraction of absorbing molecules, which do not emit in the respective screening and imaging setups. Furthermore, this difference could indicate the detection of different fluorescent states. Due to the high variation in temporal resolution, with µs-resolution in the screening and characterization setup and seconds in the *in vitro* approach, determination of the cause for this varying behavior requires additional measurements.

Interestingly, the detected off-state showed a 10 % absorption increase and 5 nm redshift of the Soret band peak. In heme-binding holoproteins, such as the mitochondrial cytochrome P450, water molecule displacements can cause changes in the respective Soret peak [157]. For PENELOPE, this might be caused by light-induced protein conformation changes, which ultimately lead to a displacement of the pyrrole water. This pyrrole water molecule is located in 3 Å proximity to BV rings A, B and C [104]. For heme-binding holoproteins, a Soret band red shift is caused by modification of the ligands [157]. For PENELOPE, the marginal red-shift could be caused by the conformational changes of the BV D-ring. In addition to light-induced changes, increasing pH values also showed an increase of the Soret peak. However, a bathochromic shift was not observed. These findings indicate light-driven effects on the chromophore environment and

chromophore conformation, whereas pH-driven effects are only observed on the chromophore environment.

A further observation was the apparent metastability of the fluorescent off-state in vitro. While the off-state to on-state transition occurred on a ms-time scale in laser-probed *E. coli* and mammalian cells, *in vitro* UV/VIS absorption spectroscopy suggest an off-state to on-state transition within hours. A major diverging condition between the screening or imaging environment and the in vitro environment is attributed to the utilized light source. For screening and imaging, lasers as a point source of coherent light were used and allowed beam focusing to a micrometer-sized spot with high intensities. In contrast, in vitro switching was carried out under LED light illumination. This illumination method allowed generation of rather low light intensities corresponding to significantly increased focal spot. Interestingly, the metastability of PENELOPE observed with LED light resembles the metastability of naturally occurring bacteriophytochromes exhibiting intact photoswitching. This raises the question, whether bacteriophytochrome-derived FPs with an intact or reconstituted photoswitching cycle populate different fluorescent states with varying metastabilities depending on the applied light intensity. Following this assumption, high laser intensities with a small focal spot size preferably transfer PENELOPE to a short-lived non-fluorescent state allowing for thermal relaxation in the millisecond range. Lower laser intensities within an enlarged spot would transfer PENELOPE to a long-lived non-fluorescent state with a thermal relaxation in the hour range. In this scenario, the long-lived non-fluorescent state could correspond with the Pfr-state (section 1.4.2). The susceptibility of the off-switched state for 780nm light reinforces this hypothesis. The short-lived non-fluorescent state on the other hand, could correspond with, or resemble the protonated Meta-Ra or deprotonated Meta-Rc state [95]. However, this model is highly hypothetical and needs to be evaluated by either crystallographic structures or ultrafast spectroscopy.

The dimerization tendencies of naturally occurring bacteriophytochromes can pose serious challenges for the development of a bacteriophytochrome-derived FP. With the development of the first monomerized bacteriophytochrome-derived FPs IFP1.4 [90] based on *Deinococcus radiodurans* and mIRFP670v1 [123] based on *Radiodurans palustris*, future engineering approaches could be conducted in a more targeted fashion. In conjunction with the application in super-resolution microscopy, dimeric behavior of PENELOPE would have severe effects regarding the informative value of recorded super-resolution images. Despite the spatial separation of the PENELOPE amino acid mutations from the *Deinococcus radiodurans* monomerization mutations, the creation of a new dimer interface could not be ruled out. The conducted SEC experiment revealed a peak of PENELOPE at the elution volume expected to represent monomeric behavior. However, a small shoulder at a smaller elution volume that could resemble a dimeric fraction was observed. The implementation of SEC at 4 °C allowed detecting low oligomerization tendencies. During

imaging of biological samples at room temperature or under physiological conditions, this effect could be reduced due to increased temperatures.

3.4 Imaging

In the past, constitutively fluorescent bacteriophytochrome-derived FPs were applied in various imaging projects. Imaging in mouse models was the method of choice for many of these applications due to the presence of BV in living mice. Planar whole-body fluorescence imaging in the NIR window was first shown with IFP1.4 in 2009 by Shu et al.[90]. With the expansion of the NIR-FP palette and increasing the respective QYs, also advanced imaging techniques paved their way into the NIR window. In 2012, iRFP713 was used to image 4 mm deep subcutaneous tumors with the deep-tissue Photo Acoustic Microscopy (PAM) imaging[158]. Further applications of iRFP713 included Fluorescence diffuse Optical Tomgraphy (FMT), which allowed three-dimensional reconstruction of organs in mice [159]. In conjunction with the recently reported SNIFP and the emIRFP toolbox, bacteriophytochromes pioneered for live-cell super-resolution microscopy. Both proteins were imaged using STED microscopy in the NIR window with high depletion beam intensities [121, 124].
With the development of PENELOPE, the toolbox for NIR live cell imaging has been expanded by the first bacteriophytohrome-derived RSFP allowing for confocal and super-resolution imaging in live and fixed cells.

3.4.1 Confocal imaging

PENELOPE allowed the successful tagging and confocal imaging of a wide range of target proteins. These target proteins included filamentous and spherical structures of which the latter have various pH conditions. The observed structures exhibited correct localization. For transient transfections, single cells showed overexpression artifacts, which is a commonly observed phenomenon. The recoding of a 4 color image with the plurally transfected stably expressing cytokeratin-18-PENELOPE cell line highlights the benefits of harnessing the NIR window as a further recording channel (see appendix Figure 5.8).
The low cellular fluorescence of PENELOPE compared to constitutively fluorescent bacteriophytochrome-derived FPs required increased laser intensities for sparsely labeled structures such as Nup50. For these dim structures, prolonged dwell-times did not linearly increase the number of emitted photons, due to the inherent simultaneous off-switching of PENELOPE. This side effect was circumvented by applying line accumulation with shorter dwell-times to allow for a thermal relaxation between scanning steps.
The parameters used for the confocal imaging of 5000 frames included an excitation laser power of 4.82 µW applied for 15 µs at a pixel size of 80 nm. This resulted in a total light dose of 1.12 J/cm^2. This light dose is in accordance with general confocal imaging conditions. In this setting, rapid photobleaching occurs within the first 200 frames.

Immediate phototoxic effects such as cell shrinking were not observed. However, since phototoxicity is cell and sample-dependent, experiments with a higher sensitivity for photoinduced toxicity and stress factors are required. For long-term imaging, the slowdown on cell-division rates in *Caenorhabditis elegans* was chosen as phototoxicity-affected parameter [160]. The cell cycle prolonging in yeast was suggested as an additional parameter [161].

3.4.2 NIR-RESOLFT super-resolution microscopy with PENELOPE

Phototoxicity becomes even more crucial when applying light doses in the kJ/cm^2 range. This is the case for most super-resolution microscopy methods. In 2018, Kilian et al. assessed the photodamage of live-cell STED microscopy and reported an impaired cell health after 24h with 75 % the cells being affected or dead [45]. In 2015, Wäldchen et al. showed the influence of irradiation wavelength and total irradiation time typically used in widefield PALM and STORM microscopy. For 488nm irradiation, illumination for 240 s at laser intensities of 0.2 kW/cm^2 resulted in ~ 60 % dead cells and 40 % undividing and thereby affected cells. For 639 nm irradiation, illumination for 240 s at laser intensities of 2 kW/cm^2 did not affected any cells. For confocal laser scanning microscopy methods, it is hypothesized that cells imaged with wavelengths >488 nm should tolerate total light doses of a few kJ/cm^2 [76].

The only published live-cell super-resolution imaging with bacteriophytochrome-derived FPs so far, was STED imaging with SNIFP and emIRFP703 at light doses of 244 kJ/cm^2 [121] and 49-59 kJ/cm^2 [124], respectively. The light doses utilized for the generation of super-resolved images with PENELOPE in this work range from 1.275 kJ/cm^2 to 6.375 kJ/cm^2. A relative classification of RSFPs previously used in RESOLFT microscopy in comparison to PENELOPE is displayed in the appendix (Figure 5.6 and Figure 5.7) In order to evaluate the improvement of the total light dose parameter, phototoxicity assays as presented by Wäldchen et al. are required in the future. Comparison with SNIFP and emIRFP703 STED images only involved light doses, which contained quantification of improved resolution. The obtained resolutions of single filaments with minimum FWHMs of 60nm in NIR-RESOLFT microscopy are only slightly higher or equal compared to previously published RESOLFT microscopy images in the green, yellow and red spectrum. However, the absence of UV/blue light and the sole application of 660nm laser light highlights the benign properties of NIR-RESOLFT microscopy with PENELOPE.

Additionally to spatial resolution, temporal resolution is a further important factor for live-cell imaging. Dynamic processes in living cells such as vesicle transport [162], microtubule growth [163] or actin fiber growth [164] require fast imaging with short frame times and therefore pose serious challenges for the respective imaging method of choice. A pixel dwell time of >5 ms, limits NIR-RESOLFT imaging of cellular dynamics with PENELOPE to small regions of interest or imaging of slow processes. Appendix Figure 5.9

shows successful timelapse imaging of cytokeratin-18 dynamics over three images. After image formation of frame 3, mechanical drift led to focus loss. These challenges were the driving force to investigate the switching kinetics of PENELOPE in chemically fixed cells. This work allowed RESOLFT imaging in chemically fixed cells for the first time and resulted in a clearly improved resolution as well as image quality. The comparison of switching curves in live and fixed cells did not reveal changes regarding switching speed, thermal relaxation and residual fluorescence. However, the fluorescence brightness was slightly decreased. So far, GFP-like RSFPs Dronpa, rsEGFP2 and Skylan-NS were shown to maintain their switching in fixed Cos-7 cells under low light intensity illumination. (f)PALM/STORM imaging with Dronpa and mGeos-M on β-actin structures harnessed the slow off-switching and allowed image recordings with a localization precision of 15 nm and 12 nm, respectively [165]. However, these publications did not comment on effects on the switching kinetics in comparison to living cells. In 2015, Ilgen et al. published a fusion construct consisting of an antibody-binding Z-domain and rsEGFP2, which allowed RESOLFT imaging of previously fixed cells [143]. However, RESOLFT imaging of genetically tagged fixed cells was not performed. For Dronpa and asFP595, an aqueous environment is required for light-driven switching [65] , which prevents usage of methanol fixation. In contrast, formaldehyde fixation creates reactive Schiff bases mainly with lysine, tryptophan and cysteine side chains, which subsequently generate cross-linked products with surrounding nucleophiles [166]. Sequence analysis of rsEGFP2 and PENELOPE revealed a strong disproportion between formaldehyde-affected amino acids with 24 for rsEGFP2 and only 10 for PENELOPE. A direct or indirect effect on the respective chromophore could decrease with a reduction of potential formaldehyde-affected amino acids. In further studies, this theory could be validated via X-ray crystallography or NMR spectroscopy, if the purified protein solution maintains its switching properties during formaldehyde fixation.

The ability to maintain the switching in chemically immobilized cells opened the door for the implementation of the presented NIR-RESOLFT pixel-hopping approach. In this approach, the time-consuming thermal relaxation of the conventional stepwise-scanning was circumvented by skipping laser beam-affected off-switched proteins and immediately repeat the off-switching and readout step. NIR-RESOLFT pixel hopping had resulted in pixel dwell time saving of 87%.
However, the generated images did only show a limited resolution increase. An altered behavior of the ensemble BpRSFPs due to the modified illumination pattern is unlikely, since the time to achieve sufficient thermal relaxation was maintained by imaging total x-axis ranges of >15µm. Furthermore, signal reduction of ~50-66% for the RESOLFT image compared to the confocal image was observed, suggesting effective off-switching. Excluding BpRSFP-related factors, mechanic limitations appear as a potential cause. A scanning position mismatch of a few nanometers could level the achieved resolution improvement. With “pixel hop” distances between 400nm and 1µm, the utilized galvanometric scanner might incompletely translate the input voltage to a shifted x-position or display an increased localization divergence. A further analysis of this potentially limiting

hardware difficulty is planned after the submission of this thesis. Should this technical obstacle be overcome, NIR-RESOLFT pixel hopping would work as a bridge technology between conventional step scan NIR-RESOLFT and a parallelized approach. Due to the low light levels required for NIR-RESOLFT, the degree of parallelization could achieve multiple magnitudes [167].

3.5 Fluorescent states of PENELOPE in imaging

The novel switching of PENELOPE compared to established GFP-like RSFPs such as rsEGFP2 provides remarkable properties for its use in RESOLFT microscopy. Fast off-switching kinetics and minimum residual fluorescence of ~ 5 % at low light intensities of ~ 0.2 kW/cm^2 are very well suited for RESOLFT microscopy. In addition, the proposed fluorescent intermediate state, exhibiting a low fluorescence quantum yield, would allow for fluorescence readout at high laser intensities without simultaneously accelerating the off-switching. This is in contrast to RESOLFT with rsEGFP2, which shows a positive correlation between applied laser intensity and off-switching half-time [47].

Unusual switching of PENELOPE at laser intensities $I \geq 1$ kW/cm^2 suggested a diverging switching state model as it has been described for the GFP-like RSFP rsEGFP2. For rsEGFP2, it is assumed that the protein can only exist in a fluorescent on-state or a non-fluorescent off-state [36]. The inability to entirely populate the non-fluorescent off-state, which would be beneficial for RESOLFT imaging, can be explained by simultaneous partial on-switching during off-switching as a consequence of overlapping absorption spectra of these fluorescent states. For PENELOPE, the kinetics data in mammalian cells suggest a more complex interaction of switching states. Simulation data based on the mammalian cells kinetics data suggest an additional fluorescent intermediate state. In the three-state model, the transition from the on-state to the fluorescent intermediate state is light-driven and depends on the off-switching cross section σ_{off} and the light intensity I. The intermediate state can transition to the off-state with a light-independent rate constant $k_{off.}$ Initially discussed thermal relaxation provides the major transition force to reach the fluorescent on-state with a rate constant k_{on}. This step can however be accompanied by a light-driven transition which depends on the on-switching cross section σ_{on} and the light intensity I.
With insufficient off-switching laser intensities of 0.01 kW/cm^2, a fraction of the proteins remains in the on-state while the majority of the ensemble proteins was transferred to the off-state. The contribution of the intermediate state is marginal. For off-switching laser intensities of 0.2 kW/cm^2, approximately 95% of ensemble proteins are transferred to the off-state. Residual fluorescence is caused by remaining on-state proteins and an increasing number of intermediate state proteins. For high off-switching laser intensities $I > 5$ kW/cm^2, residual fluorescence increases and is almost completely caused by proteins in the intermediate state.

3.6 Conclusion and outlook

The NIR-RESOLFT imaging performed in this work is an innovative approach to transform super-resolution microscopy from a powerful but potentially cell damaging method to a benign technique to unveil cellular features beyond the diffraction limit. This has been accomplished by the engineering of the bacteriophytochrome-derived RSFP PENELOPE. Its unique ability to harness thermal relaxation in the millisecond range makes it the first RESOLFT applicable RSFP that does not require a light-driven on-switching step. This ability reinforces its inherent spectral superiority towards GFP-like RSFPs in terms of phototoxicity prevention. In addition, PENELOPE proved resilient towards chemical fixation and is the first genetically encoded RSFP applied in RESOLFT microscopy of fixed mammalian cells. Its unique switching characteristics suggest a novel fluorescent state model, which could enhance the potential of RESOLFT microscopy in the NIR window.

Future screening approaches involving PENELOPE should either address its thermal relaxation kinetics or increase its Pfr to Pr switching quantum yield. Increased thermal relaxation kinetics would allow for shortened pixel dwell times, whereas increases Pfr to Pr switching quantum yield would result in an additional control element for NIR-RESOLFT imaging. Due to the long dwell times required for conventional step scan NIR-RESOLFT imaging with PENELOPE, time-lapse imaging proved difficult. Occasionally occurring mechanical drift on the microscope stage due to unfavorable ventilation in the microscopy room became the main reason for impeded long-time imaging. Follow up experiments on long-term NIR-RESOLFT imaging in live and fixed cells will be conducted after the submission of this thesis. In conjunction with long-term live-cell imaging, quantification of potential phototoxic effects should be performed. Furthermore, troubleshooting of the unsuccessful NIR-RESOLFT pixel hopping image formation is a top priority. As discussed earlier, investigation of the galvanometric scanner position accuracy could reveal a potential source of error. The derived fluorescent state model should be supported by additional experiments. At this point, two collaborator groups located in Grenoble, France and Lille, France are working on revealing structural and photodynamic insights of PENELOPE in the form of X-ray crystallography and ultrafast spectroscopy. Once these improvements have been established and thoroughly characterized, advanced imaging experiments can be performed. Further exciting and evident experiments with PENELOPE would cover three-color RESOLFT microscopy and NIR-RESOLFT in tissues and whole animals.

4 Material and methods

4.1 Restriction enzyme cloning and mutagenesis

For restriction enzyme cloning, the gene of interest was amplified using polymerase chain reaction (PCR), digested with restriction enzymes and subsequently ligated with a DNA ligase into the previously restriction enzyme treated DNA vector backbone.

DNA amplification

For DNA insert amplification, purified DNA was mixed in a standard PCR buffer containing Master Mix (Table 1) on ice. The PCR amplification reaction protocol consisted of a denaturation, annealing and elongation step (Table 2) and was carried out in a Biometra Tone Thermocycler (Analytik Jena, Jena, Germany). Remaining template DNA was digested by adding 1ul Dpn1 (Thermo Fisher Scientific, Waltham, MA) to the reaction mix and incubating over night at 37 °C. PCR product purification was performed using NucleoSpin® Gel and PCR Clean-up kit (Macherey-Nagel, Düren, Germany).

Table 4.1: PCR amplification master mix

5 µl	10x PCR buffer
1.5 µl	sense primer (10µM)
1.5 µl	antisense primer (10µM)
50-100 ng	template DNA
2 µl	dNTP stock solution (10 mM each)
1 µl	Pfu DNA polymerase
add up with ddH_20 to 50 µl	

Table 4.2: PCR amplification cycle protocol

Temperature	Time	
94 °C	5’	
94 °C	1'	30x
55 °C	1'	
72 °C	2'/kb	
72 °C	10'	

Restriction enzyme digestion

Digestion of PCR product and DNA vector backbone was performed with the respective restriction enzymes and restriction enzyme buffers (Thermo Fisher Scientific, Waltham, MA, USA) according to the manufacturer’s instructions. Subsequent backbone

dephosphorylation prohibited religation of the digested DNA vector backbone and was achieved by 1h incubation with 1µl FastAP Thermosensitive Alkaline Phosphatase (1 U/µl; Thermo Fisher Scientific, Waltham, MA, USA) and subsequently inactivated by incubation at 65 °C for 10min.

DNA vector and insert purification

Digested DNA vector backbone was purified following agarose gel electrophoresis by DNA gel extraction, whereas digested PCR product was purified with the QIAquick PCR purification kit (Qiagen, Hilden, Germany) according to the manufacturer's instructions. Agarose gel electrophoresis required dissolving agarose (BioBudget Technologies, Krefeld, Germany) in 1x TAE buffer at a concentration of 1.2 % (w/v) with subsequent solidifying for 30min in a BlueMarineTM 100 gel chambers (Serva Electrophoresis, Heidelberg, Germany). Along with the samples, GeneRulerTM 1 kb DNA ladder (Thermo Fisher Scientific, Waltham, MA, USA) was applied as a reference marker. A constant voltage of 80 V was applied for 1h by a 300V power source (VWR, Radnor, PA, USA), separating digested and undigested DNA vector backbone. DNA band visualization was achieved by staining with ethidium bromide for 15min. DNA fragments matching the expected length were analyzed under UV light and cut out from the agarose gel. DNA isolation from gel fragments was achieved with the NucleoSpin® Gel and PCR Clean-up kit (Macherey-Nagel, Düren, Germany) according to the product instructions.

DNA ligation

DNA ligation of purified DNA vector backbone and PCR product was carried out in a master mix (table) over night at 4 °C and inactivated at 65 °C for 10min. Dialysis for 45min on 0.025 µm MCE MF-MilliporeTM membranes (Merck, Darmstadt, Germany) for salt removal allowed immediate transformation of electrocompetent *E. coli* cells with 5µl ligation solution.

Site-directed mutagenesis

Directed substitution of close-proximity base pairs was conducted via siye-directed mutagenesis. A site-directed mutagenesis master mix (Table 3) containing the plasmid of interest was subject to a specialized PCR protocol (Table 4). Remaining template DNA was digested by adding 1ul Dpn1 (Thermo Fisher Scientific, Waltham, MA) to the reaction mix and incubating over night at 37 °C. PCR product purification was performed using NucleoSpin® Gel and PCR Clean-up kit (Macherey-Nagel, Düren, Germany). Dialysis for 45min on 0.025 µm MCE MF-MilliporeTM membranes (Merck, Darmstadt, Germany) for salt removal allowed immediate transformation of electrocompetent *E. coli* cells with 5µl site-directed mutagenesis solution. Mutagenesis primers can be found in table 7

Table mastermix

Table 4.3 Site-directed mutagenesis PCR master mix

5 µl	10x PCR buffer
1 µl	sense primer (10µM)
1 µl	antisense primer (10µM)
200 ng	template DNA
1 µl	dNTP stock solution (10 mM each)
1 µl	Pfu DNA polymerase
add up with ddH_20 to 50 µl	

Table 4.4: Site-directed mutagenesis PCR cycle protocol

Temperature	Time	
94 °C	30''	
94 °C	1'	16x
55 °C	1'	
68 °C	10'	
68 °C	10'	

Error-prone mutagenesis

Random mutations within the gene of interest were introduced by error-prone mutagenesis. An error-prone mutagenesis master mix (Table 5) containing the plasmid of interest was divided into four separate 0.2ml PCR tubes in order to allow for higher mutation variety. The master mix containing tubes were subsequently subject to a specialized PCR protocol (Table 6). After PCR, the samples were combined and PCR fragments along with DNA vector backbone were purified, restriction enzyme digested and ligated as described in the previous sections and subsequently 5µl error-prone mutagenesis solution were transformed into electrocompetent *E. coli* cells. Mutagenesis primers can be found in table 7

Table 4.5: Error-prone mutagenesis PCR master mix

10 µl	10x EP-PCR buffer
10 µl	sense primer (10µM)
10 µl	antisense primer (10µM)
1 µg	template DNA
10 µl	10x EP-dNTP stock solution
1-3 µl	$MnCl_2$ (10mM)
2 µl	*Taq* DNA polymerase
add up with ddH_20 to 50 µl	

Table 4.6: Error-prone mutagenesis PCR cycle protocol

Temperature	Time	
94 °C	1’	
94 °C	30’’	30x
55 °C	45’’	
72 °C	90’’	
72 °C	2'	

DNA sequencing

DNA sequencing of generated plasmids was performed by Microsynth Seqlab (Balgach, Switzerland) in Göttingen. For sequencing, 1ug DNA was diluted in a total volume of 12µl ddH_2O and added with 10µM of the respective sequencing primer.

4.2 Bacterial protein expression and purification

4.2.1 *E. coli* expression systems

Fluorescent protein expression of intermediate or final variants was carried out in different expression systems. Bacterial expression was used for cloning and screening of intermediate variants as well as for switching characteristics analysis and protein purification for final variants.

E. coli strain DH5α (MAX Efficiency DH5αF’IQ Competent Cells; Life Technologies, CA, USA) was used for cloning purposes, whereas *E. coli* strain TOP10 (TOP10 Electrocomp Kits; Invitrogen, Waltham, MA, USA) was used for plasmid amplification. Prior to fluorescent protein expression, *E. coli* BL21AI cells (BL21-AITM One ShotTM Chemically Competent *E. coli*, Thermo Fisher Scientific, Waltham, MA, USA) were transformed with a heme-oxygenase expressing pWA21-plasmid. The pWA23h-plasmid expressing BL21AI-cells were utilized for fluorescent protein expression required for protein purification, screening and switching characteristics analysis.

The underlying expression systems for all *E. coli* related experiments was the pBAD/His-B backbone containing pBAD-mKalama1 expression vector, which was kindly provided by Robert Campbell (Addgene Plasmid # 14892). Fluorescent protein expression is controlled by an arabinose-inducible araBAD promoter. A N-terminally added and TEV-protease cleavable 6x His-tag allowed purification via a Ni^{2+}-NTA system. Restriction enzyme cloning into this vector required insert amplification with primers 6185 and 6196 (table) and

subsequent digestion with restriction enzymes EcoRI/SalI. The digested insert was ultimately ligated into the EcoRI/XhoI digested expression vector.

In addition, the previously transformed pWA23h-plasmid, which was kindly provided by Shcherbakova and Verkhusha, allowed Rhamnose-induced heme oxygenase expression for the increased degradation of heme to BV, Fe^{3+} and CO in addition to natural *E. coli* heme degradation. The hmuO gene codes for the heme-oxygenase of Bradyrhizobium ORS278. In order to provide a sufficient concentration of heme, heme progenitors $FeCl_3$ (AppliChem, Darmstadt, Germany) and δ-aminoluveic acid (Sigma-Aldrich, St. Louis, MO, USA) were added in molar concentrations of 50µM and 100µM, respectively.

4.2.2 *E. coli* protein expression and purification

E. coli transformation was achieved by electroporation. For this, electrocompetent cells (ref) of the *E. coli* strains DH5α, TOP10 and BL21-AI were created. For this, a 500mL LB culture was inoculated with the respective *E. coli* strain in a volumetric ratio of 1:100 and grown at 37C until an OD_{600} of 0.6-1.0 was reached. Cells were then cooled on ice for 30min and subsequently centrifuged at 4 °C with 5000 xg for 15min using a Sorvall RC6 Plus centrifuge with a HS-4 rotor (Thermo Fisher Scientific, Waltham, MA, USA). The following washing steps required repeated centrifugation and resuspension in 500 ml and 250 ml ddH_20 and 10mL 10% glycerol with a final resuspension in 1mL 10% glycerol. Cells were aliquoted in 50µl volumes, flash-frozen in liquid nitrogen and stored at -80 °C.

For transformation, 50µl electrocompetent cells were thawed and on ice and resuspended in 120µl ddH_2O. The mixed volume was transferred to a precooled electroporation cuvette (2 mm gap size; cell projects, Harrietsham, United Kingdom). For transformation of mutagenesis (ref), 5µl of purified DNA were added. For circular plasmid DNA, 1µl was added. A Bio-Rad Gene Pulser (Bio-Rad, Hercules, CA, USA) at 2.5 kV, 200 Ω and 25 µF was used for electroporation of electrocompetent cells. 1mL LB medium was immediately added after electroporation and cells were resuspended. After transferring the cells to a 1.5mL tube, cells were incubated for 1h at 37 °C to allow expression of antibiotics resistance. After incubation, cells were plated on agar plates containing the respective antibiotics resistance. For screening, switching characteristics analysis and protein purification, agar plates containing additional kanamycin antibiotics along with 0.02% arabinose and heme progenitors $FeCl_3$ (AppliChem, Darmstadt, Germany) and δ-aminoluveic acid (Sigma-Aldrich, St. Louis, MO, USA) were used. The cells were incubated for 24h at 37 °C.

Bacterial protein expression

For protein expression, proteins of interest were encoded in a pBad expression plasmid and transformed into BL21-AI *E. coli* (Invitrogen, Carlsbad, USA), which were previously transformed with a heme oxygenase expressing pWA23h plasmid. Bacterial colonies were

grown on rectangular RFA agar plates containing 0.02% arabinose and 0.02% rhamnose along with 50 µM $FeCl_3$ and 100 µM δ-aminolevulinic acid (ALA) (Sigma-Aldrich, St. Louis, MO, USA) as hemoglobin precursors to ensure BV availability. Protein expression was performed at 37 °C for 24 h. Depending on the required final amount of protein, between 4 and 40 *E. coli* full grown RFA plates were used for protein purification.

Bacterial protein purification

Following the expression, cells were collected via cell scraping in 2mL binding buffer (20 mM phosphate, 500 mM NaCl, and 20 mM imidazole, pH 7.4). Next, the cell suspension was incubated with 10µg/mL lysozyme (Serva electrophoresis, Heidelberg, Germany) on ice for 5h. Following lysozyme treatment, a cOmplete protease inhibitor (Roche, Basel, Switzerland) was added, incubated for 10 minutes on ice and subsequently frozen and thawed five consecutive times with liquid nitrogen and lukewarm water. Finally, cell lysate was supplemented with 0.5µl benzonase (Thermo Fisher Scientific, MA, USA) and protein solution was separated from debris by centrifugation 4 °C and 21,000 rcf for 4h. Isolation of proteins of interest from supernatant was performed by Ni-NTA affinity chromatography (His SpinTrap Kit, GE Healthcare, Little Chalfont, GB) according to the manufacturer's protocol. After purification, the protein concentration was determined using Bio-Rad Bradford assay (Hercules, CA, USA). Purified protein was taken up in 100 mM Tris-HCl, 150 mM NaCl, pH 7.5 via Vivaspin® 500 centrifugal concentrators (Sartorius, Göttingen, Germany) with a molecular cut-off at 100 kDa. At low concentrations in a big volume, samples were concentrated using Vivaspin® 500 centrifugal concentrators (Sartorius, Göttingen, Germany) with a molecular cut-off at 30 kDa.

4.3 Spectral measurements and oligomerization

All spectral measurements were performed with purified protein in 100mM Tris-HCl, 150mM NaCl, pH 7.5.

4.3.1 Spectroscopy

Absorption spectroscopy

Absorption spectra were measured on a Varian Cary 4000 UV/vis spectrometer (Varian, Palo Alto, CA, USA) in a quartz glass ultra-micro fluorescence cell cuvette a 1.5 mm light path (Hellma, Müllheim, Germany). Absorption spectra were detected between 250nm and 800nm starting from the highest wavelength. Absorption spectra in this work depict single or triplicate measurements.

Fluorescence spectroscopy

Excitation and emission spectra were measured on a Varian Cary Eclipse fluorescence spectrometer (Varian, Palo Alto, CA, USA) in a quartz glass ultra-micro fluorescence cell cuvette a 1.5 mm light path (Hellma, Müllheim, Germany). Excitation spectra were detected between 500 nm and 750 nm at a constant emission of 760 nm. Emission spectra were detected between 650 nm and 800 nm at a constant excitation of 640 nm. Excitation and emission spectra in this work depict triplicate measurements.

In vitro switching of fluorescent proteins

Switching to the on- or off-state was also performed in a quartz glass ultra-micro fluorescence cell cuvette a 1.5 mm light path with a mercury-vapor lamp with a Brightline Fluorescence 661/20 filter (Semrock, NY, USA) for off-switching (9.9 mW/cm^2, 0.44 mW measured behind the cuvette filled with Tris protein buffer) and a M780LP1 LED (Thorlabs,NJ, USA) for on-switching (18.7 mW/cm^2, 1.4 mW measured behind the cuvette filled with Tris protein buffer). For the mercury-vapor lamp, the incident white light is directed via a fiber, to an emission filter carrying scaffold and entering a second fiber which is directed at the quartz glass ultra-micro fluorescence cell cuvette window. For the M780LP1 LED, no fiber is required and the quartz glass ultra-micro fluorescence cell cuvette window is placed directly in front of the LED.

Power measurements were performed with a PM200 power meter equipped with a S170C sensor (ThorLabs, Newton, NJ, USA). Illumination time was hand-controlled and therefore allows for minor inaccuracies.

4.3.2 Biophysical FP parameters

Extinction coefficient

The extinction coefficient of bacteriophytochrome-derived fluorescent proteins was calculated relative to free BV in solution (39 900M^{-1} cm$^{-1)}$. All spectra were baseline corrected and normalized to the 280 nm absorption peak.

Fluorescence quantum yield

Fluorescence quantum yield was determined either using a Quantaurus-QY system (Hamamatsu, Hamamatsu City, Japan) or by Dr. Alexey Chizhik using a nanocavity-based method. Both procedures used purified protein solution in standard protein buffer at pH 7.5.

Fluorescence lifetime

Fluorescence lifetime was determined either using a Quantaurus-Tau fluorescence lifetime spectrometer (Hamamatsu, Hamamatsu City, Japan) or by Dr. Alexey Chizhik using a nanocavity-based method described by Chizhik et al. Both procedures used purified protein solution in standard protein buffer at pH 7.5.

4.3.3 pH-dependent absorption and emission spectra

pH-dependency of equilibrium state fluorescent proteins was recorded on a Cytation 3 imaging plate reader (BioTek, Winooski, VT, USA). Sample preparation required dilution to 200µM in protein buffer and overnight equilibration at room temperature. In a 96 well UV-Star® micro plate (Greiner Bio-One, Frickenhausen, Germany), technical triplicates were prepared by diluting the equilibrated samples to a final concentration of 5µM. Subsequently, absorption spectra from 250 to 600 nm were recorded. For emission spectra detection, the spectral range between 640 nm and 800 nm was chosen at a constant excitation of 630nm. The detector sensitivity was scaled to the wells with the highest fluorescence intensity. Data analysis was done in OriginPro 2018b (OriginLab Corporation, Northampton, MA, USA). p_{Ka} value determination was determined by fitting a monophasic dose response function for pH3-pH5.5 and fitting a biphasic dose response function for pH5.5-pH10.

4.3.4 Seminative SDS PAGE

Oligomerization tendencies were determined via seminative SDS PAGE. A 15% (w/v) polyacrylamide separation gel (6.3 ml H_2O MilliQ, 5 ml 1.5 M Tris-HCl pH 8.8, 8.3 ml Rotiphorese Gel 30 solution (Roth, Germany), 200 µl 10 % (w/v) (SDS), 200 µl 10 % (w/v) ammonium persulfate (APS), 20 µl Tetramethylethylendiamin (TEMED)) and a 5 % (w/v) collection gel (5.6 ml H_2O MilliQ, 2.5ml 1.5 M Tris-HCl pH 6.8, 1.7 ml Rotiphorese Gel 30 solution, 100 µl 10 % (w/v) SDS, 100 µl 10 % (w/v) APS, 10 µl TEMED) were prepared. 10 % (w/v) sucrose solution (Merck, Germany) was added to 4 µg protein solution. Gel electrophoresis was conducted at 20 mA/gel. Fluorescence of PENELOPE was excited at 655/40 nm and detected at 740/40 nm. After fluorescence detection, gels were stained with a staining solution (Coomassie-brillant-blue, 0.05 % (w/v) Coomassie R250 (Sigma-Aldrich, USA), 25 % isopropanol and 10 % acetic acid (Merck, Germany) for 1h. Destaining was performed over night in 10 % (w/v) acetic acid (Merck, Germany)

4.3.5 Size exclusion chromatography

Detailed determination of fluorescent protein oligomeric states was determined size exclusion chromatography (SEC). Prior to sample application, the system was calibrated using protein solutions with known molecular weights (Blue dextran, Aprotinin, Ribonuclease A, Carbonic Anhydrase, Ovalbumin, Conalbumin)
Samples were applied to an Äkta pure chromatography system equipped with a SuperdexTM 200 Increase 10/300 GL column (GE Healthcare, Chicago, IL, USA). After filtering the protein solution with a VIVASPIN 500 column with a 0.2 µm PES membrane (Satorius, Göttingen, Germany), 250 µl 10 µM protein solution were applied to the SuperdexTM 200 Increase 10/300 GL column and eluted in standard protein buffer at a constant flow rate of 0.75ml/min. Detection of proteins was achieved by 280 nm absorption with a UV monitor U9-L (GE Healthcare, Chicago, IL, USA). Sample markers for monomeric and dimeric states were mEGFP and dTomato. All measurements were performed at 6 °C.

4.4 Automated screening setup

Screening and characterization of BpRSFPs was performed at an intragroup developed and built automated microcope. The microscope body was a Leica DM5500 B upright microscope (Leica Microsystems, Wetzlar, Germany). A 20x/0.4 NA objective was used for irradiation and emission focusing. Utilized laser lines included a 100 mW 660 nm CW diode laser (Coherent, Santa Clara, CA, USA) and a 50 mW 785 nm CW diode laser (Coherent, Santa Clara, CA, USA). Laser powers were controlled with acousto-optic tunable filters (AA.AOTF.nc-TN 1002 Opto-Electronic Orsay, France). The excitation wavelengths were superimposed via a beam splitter and directed towards the remaining beam path via a P5-780PM-FC-5 optical fiber (ThorLabs, Newton, NJ, USA). Spectral separation of excitation light and emission light was accomplished via a dichroic mirror (reflection: 630-730 nm, 750-800 nm; transmission: 695-730 nm) and a bandpass filter (HC 710/40, AHF Analysetechnik, Germany). Fluorescence emission was detected with a H10723-20 PMT (Hamamatsu, Japan). Microscope and lasers were controlled with intragroup-developed Labview software (National Instruments, Austin, TX, USA). The software furthermore controlled the autofocus, which was required for automated screening and characterization of bacterial colonies.

4.4.1 Screening and characterization

Screening and characterization of bacterial colonies was initiated after colony selection. The selection was either performed manually by probing colonies with a low intensity excitation laser and subsequently adding the position as a screening location or automated after previous fluorescence recoding of the bacterial colonies on a Amersham Imager 600RGB (GE Healthcare, Chicago, IL, USA). Threshold adjustment were done in the Fiji distribution

imageJ (v1.52p) and subsequent software control was again performed a LabVIEW (National Instruments, Austin, TX, USA) function. To prevent affecting the measurement, the autofocus light intensity was chosen slightly above the detection minimum. The sample rate was generally set to 2-10 µs due to fast switching times. Depending on the experiment, multiple cycles or alternating illumination powers or durations were applied. Recorded data were analyzed in a separate LabView program, allowing for the display of recorded fluorescent traces and subsequent calculation of switching parameters. For screening, colonies with improved parameters were picked, inoculated and DNA was ultimately isolated and sequenced from an external sequencing service (Microsynth Seqlab, Göttingen, Germany). Based on the respective mutagenesis strategy, isolated plasmids of improved variants were either pooled or separately mutagenized for the creation of the BpRSFP library. For characterization, DNA isolation, sequencing and subsequent mutagenesis was not necessary. The informative value was increased by screening multiple colonies expressing the respective BpRSFP of choice.

4.5 Mammalian cells

4.5.1 Mammalian cell expression systems

Fluorescent protein expression in mammalian cells was required for fluorescence imaging as well as switching characteristics analysis in transiently transfected and constitutively expressing mammalian expression systems.

In order to evaluate the suitability of PENELOPE as a protein fusion tag for confocal and super-resolution microscopy, PENELOPE was linked to variety of proteins of interest, namely: vimentin, keratin, F-actin (Lifeact), vesicles (clathrin), zyxin, lysosomes(LAMP1), Microtubules (EB3), Peroxisomes, Histones (H2B), nuclear pore complex protein 50 (Nup50).
To target vimentin, the coding sequence of PENELOPE was amplified using the primers 5’TCCCCCGGGCGCCACCATGTCCCGTGACCCTCTCCCCT3’ and 5’TCAGCGGCCGCTCAACTCTGGCGAAAGGCGGCAA3’. The PCR-product was exchanged with the mKate2 coding sequence in pmKate2-Vimentin (Evrogen, Moskau, RU) using AgeI/XmaI and NotI, resulting in pVIM-PENELOPE.
For the generation of a human cytokeratin-18 fusion construct, the PENELOPE coding sequence was amplified with the primers 5’ACGGTACCGCGGGCCCGGGATCCACCGGTCGCCACCATGTCCCGTGACCCTC TCCCCT3’ and 5’AGCTGTGCGGCCGCTCAACTCTGGCGAAAGGCGGCAAC3’. The PCR-product was exchanged with the TagRFP coding sequence in pTagRFP-Keratin18 (Evrogen) using KpnI and NotI, resulting in pKrt18-PENELOPE.
F-actin filaments were labeled indirectly with PENELOPE fused to LifeAct (ibidi GmbH, Gräfelfing, Germany). For the generation of a PENELOPE-LifeAct fusion construct, the

PENELOPE coding sequence was amplified with the primers 5'ACGGTACCGCGGGCCCGGGATCCACCGGTCGCCACCATGTCCCGTGACCCTC TCCCCT3' and 5'AGCTGTGCGGCCGCTCAACTCTGGCGAAAGGCGGCAAC3'. The PCR-product was exchanged with the EGFP coding sequence in Lifeact-EGFP pcDNA3.1(+) (Evrogen) using KpnI and NotI, resulting in LifeAct-PENELOPE.

To target vesicles via the clathrin light chain the coding sequence of PENELOPE was amplified using the primers 5'TCCGCTAGCGCTACCGGTCGCCACCATGTCCCGTGACCCTCT3' and 5'CACTCGAGATCTGAGTCCGGAACTCTGGCGAAAGGCGG3'. The PCR-product was exchanged with the EGFP coding sequence in pEGFP-GFP11-Clathrin light chain (Addgene plasmid #70217) using NheI and BglII, resulting in PENELOPE-GFP11-Clathrin light chain.

To target zyxin, the coding sequence of PENELOPE was amplified using the primers 5'TCCCCCGGGCGCCACCATGTCCCGTGACCCTCTCCCCT3' and 5'TTCTGCGGCCGCACTCTGGCGAAAGGCG3'. The PCR-product was exchanged with the mMaple3 coding sequence in pZyxin-mMaple3 (Addgene plasmid # 101151) using AgeI/XmaI and NotI, resulting in pZyxin-PENELOPE.

To target lysosomes via the Lysosomal-associated membrane protein 1 (LAMP-1), the coding sequence of PENELOPE was amplified using the primers 5'TCCCCCGGGCGCCACCATGTCCCGTGACCCTCTCCCCT3' and 5'TTCTGCGGCCGCACTCTGGCGAAAGGCG3'. The PCR-product was exchanged with a rsCherryRev1.4 coding sequence in pLamp1-rsCherryRev1.4-N using AgeI/XmaI and NotI, resulting in pLamp1-PENELOPE.

To label microtubule filament ends, the coding sequence for human microtubule-associated factor EB3 had previously been PCR amplified from ptagRFP657-EB3 and inserted into TagRFP-N (Evrogen, Moscow, Russia) with restriction enzymes SalI and BamHI. The coding sequence of PENELOPE was amplified using the primers 5'TCCCCCGGGCGCCACCATGTCCCGTGACCCTCTCCCCT3' and 5'CACTCGAGATCTGAGTCCGGAACTCTGGCGAAAGGCGG3'. The PCR-product was exchanged with the TagRFP coding sequence using AgeI/XmaI and NotI, resulting in EB3-PENELOPE.

To target peroxisomes, a plasmid expressing PENELOPE with the peroxisomal targeting sequence (PTS) at its C-terminus was generated. The PTS was fused to the coding sequence of mEGFP by PCR using the primers Subsequently, this PCR-product was exchanged with the coding sequence of pEGFP-Tub in pEGFP-Tub (BD Biosciences Clontech) using NheI and BamHI, resulting in pEGFP-PTS. In the last step, the coding sequence of PENELOPE was exchanged with the EGFP coding sequence using BglII and NheI, resulting in pPENELOPE-PTS.

The c-terminal fusion construct of the peroxisomal targeting sequence (PTS) with PENELOPE was designed by exchanging EGFP against PENELOPE amplified with primers 5'TCCGCTAGCGCTACCGGTCGCCACCATGTCCCGTGACCCTCT3' and

5′AACAGGATCCCTACAGCTTGGACACTCGAGATCTGAGTCCGGACTTGTACAG CTCGTCCATGCC3′ in the construct pEGFP_PTS described.
For H2B, EGFP was exchanged with PENELOPE via NheI and BglII restriction sites in the construct pEGFP-H2B.
To target the nuclear pore complex via Nup50, the coding sequence of PENELOPE was amplified via PCR using the primers 5'TCCGCTAGCGCTACCGGTCGCCACCATGTCCCGTGACCCTCT3' and 5'CACTCGAGATCTGAGTCCGGAACTCTGGCGAAAGGCGG3'. The Nup50 fusion construct was cloned by exchanging mEmerald with the PCR product via NheI and BglII in pmEmerald –Nup50 construct (addgene #54209). An overview is presented in table 8.

Table 4.7: Cloning summary including used primers and restriction enzymes.

PrimerA	PrimerB	Restriktion enzyme insert 1	Restriktion enzyme insert 2	Restriktion enzyme vector 1	Restriktion enzyme vector 2	Target structure
6000	7134	BamHI	NotI	BamHI	NotI	LifeAct
7138	7129	NheI	BglII	NheI	BglII	α-tubulin
7138	7129	NheI	BglII	NheI	BglII	Nup50-C-10
7138	7129	NheI	BglII	NheI	BglII	H2bn
6452	7134	XmaI	NotI	AgeI	NotI	TOMM20
7138	7129	NheI	BglII	NheI	BglII	Omp25
6452	7134	XmaI	NotI	AgeI	NotI	Centromeres
6452	7134	XmaI	NotI	AgeI	NotI	EB3
7138	7129	NheI	BglII	NheI	BglII	Peroxisomes
6452	7134	XmaI	NotI	AgeI	NotI	N(Cytsolic)
6983	7134	SalI	NotI	SalI	NotI	ER
6380	5540	KpnI	NotI	KpnI	NotI	Cytokeratin-18
6452	6003	XmaI	NotI	AgeI	NotI	Vimentin

4.5.2 Mammalian cell culture

HeLa (ATCC CCl-2) cells were cultivated in Dulbecco's Modified Eagle's Medium (DMEM-Medium: 4.5 g/L glucose, GlutaMAX, phenol red, 10% vol/vol FCS, 1 mM sodium pyruvate, 100 µg/ml streptomycin, 100 µg/ml penicillin) in T25 flasks for adherent cells as well as in 6-well plates for imaging and FACS analysis at 37 °C, 90% humidity and 5% CO2. Transient transfection was conducted using JetPrime transfection kit (Polyplus transfection, Illkirch, France) together with 2.5 µg of the respective expression plasmid. Approximately 2h before FACS analysis or imaging, 25 µM BV per well was added to the medium.

4.5.3 Monoclonal cell line generation

The establishment of a stable landing pad cell line constantly expressing PENELOPE-keratin and PENELOPE-vimentin was performed in a HeLa cell line containing a CAG promoter upstream of a Bxb1 attP site, both located in the AAVS1 locus on chromosome 19. The engineered cell line was kindly provided by Dr. Isabelle Jansen [168]. Integration of PENELOPE with the respective cytoskeletal protein was achieved by co-transfecting 1 µg of the respective integration plasmid together with 1 µg of the plasmid pCAG-NLS-HA-Bxb1 [169]. The plasmid pCAG-NLS-HA-Bxb1 was a gift from Pawel Pelczar (Addgene #51271) and enabled transient expression of the Bxb1 recombinase protein.

Transfected cells were kept in culture at 37 °C and 5 % CO2 for one week. Following up FACS analysis, fluorescent cells were single-cell sorted into 96-well plates and were subsequently kept in culture at 37 °C and 5 % CO2 for three weeks and ultimately analyzed with a Cytation 3 Cell Imaging Multi-Mode Reader (BioTek, Winooski, VT, USA) for correct localization under 640 nm illumination.

4.6 Microscopy

Imaging of transfected cells mounted in in HEPES buffered DMEM (HDMEM) without phenol red was performed approximately 24h after transfection. Constitutively expressing mammalian cells were imaged 24h after seeding. Cells were seeded on 18 mm glass coverslips No. 1.5H (Paul Marienfeld, Lauda-Königshofen, Germany) in 6-well plates (Sarstedt, Nümbrecht, Germany). 25 µM BV was added to the medium 2h before imaging.
Confocal and RESOLFT imaging was performed on a commercial QUAD scanning fluorescence microscope (Abberior Instruments GmbH, Göttingen, DE) built around an Olympus microscope body (IX83, Olympus, Tokyo, JPN). The microscope was equipped with an UPLSAPO 1.4 NA 100× oil immersion objective (Olympus, Shinjuku, Japan) as well as a 660 nm continuous-wave laser (Cobolt, Solna, Sweden). This laser was split via a polarizing beam splitter (PBS) in two beams. The 660 nm doughnut-shaped laser beam was realized with an easy 3D module (Abberior Instruments GmbH, Göttingen, Germany). The NIR fluorescence (680–750 nm) light was focused through a pinhole on a silicon avalanche photodiode (Photon Counting Module SPCM-AQRH-13-FC, Excelitas Technologies, Waltham, USA) for confocal and RESOLFT imaging. Microscope control and image acquisition was regulated by the software Imspector (Abberior Instruments GmbH, Göttingen, Germany). In addition to the utilized 660nm lasers, further laser lines including the wavelengths 405 nm, 488 nm, 561nm and 785nm (Cobolt, Solna, Sweden) were built into the microscope. These laser lines allowed for multicolor confocal imaging as well as potential RESOLFT imaging with 561nm, due to the direction of the splitted 561 nm beam on an easy 3D module.
Beam line orientation and general microscope architecture are depicted in Figure 4.1.
STED imaging was performed on the same microscope but required additional lasers and optical elements. A titanium-sapphire laser (Mai Tai – Spectra-Physics, Santa Clara, CA,

USA, pulse rate: 80 MHz, output pulse duration 150 fs) was directed on a laser beam splitter and split into an excitation and STED beam. The doughnut-shape of the STED beam was again generated by an easy 3D module.
Laser powers were measured behind the objective with a PM200 power meter with a S170C sensor (ThorLabs, Newton, NJ, USA). Images and filament intensity line profiles were measured with three adjacent lines and were analyzed with the Fiji distribution of ImageJ (v1.53h) and OriginPro 2020 (OriginLab, Northampton, MA, USA).

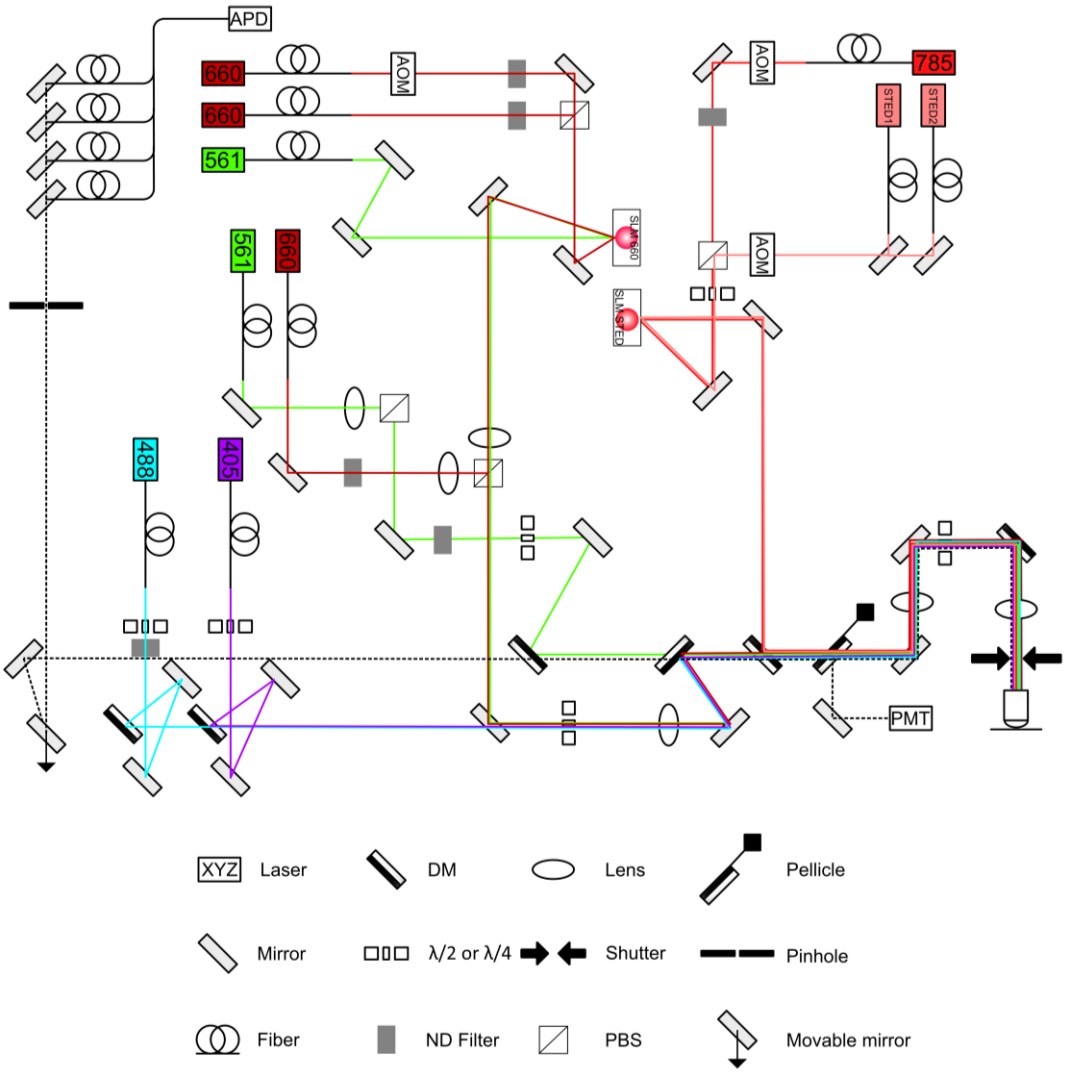

Figure 4.1: Schematic representation of the NIR-RESOLFT setup. *Laser beam lines are represented in the respective color of the laser box. Emission is depicted as dotted line. DM, Dichroic mirror; λ/2 and λ/4, phase plate; ND filter, Neutral density filter; PBS, Polarizing bam splitter; SLM, Spatial light modulator; AOM, Acoustic optical modulator; PMT, Photomultiplier tube.*

Switching kinetics in mammalian cells were recorded using a 9420 series pulse generator (Quantum composers, USA). Pulsegenerator measurements allowed laser control and detection with sub-µs temporal resolution. Application of an additional optical axis in the Imspector software (V16.3.13787-w21199 allowed pixel-wise signal detection over time.

4.6.1 Image analysis

Confocal and RESOLFT images were imported in the image-processing package FIJI and displayed with the ‘Red Hot’ lookup table. For figures 5.3 and 5.4, the background was subtracted using the rolling ball subtraction algorithm. The color table was readjusted to the maximum signal. Images were exported as .tiff files. Displayed line profiles were with a pixel width of three were extracted and fitted with a Lorentzian function in Origin Pro 2020 (OriginLab, USA)

5 Appendix

```
DrCBD        1 --------------MSRDPLPFFPPLYLGGPEITTENCEREPIHIPGSIQPHGALLTADG
Wi-Phy       1 MASMTGGQQMGRGSMSRDPLPFFPPLYLGGPEITTENCEREPIHIPGSIQPHGALLTADG
IFP2.0       1 --------------MARDFQPFFPPLYLGGPEITTENCEREPIHIPGSIQPHGALLTADG
PENELOPE     1 --------------MSRDPLPFFPPLYLGGPEITTENCQREPIHIPGSIQPHGALLTADV

DrCBD       47 HSGEVLQMSLNAATFLGQEPTVLRGQTLAALLPEQWPALQAALPPGCPDALQYRATLDWP
Wi-Phy      61 HSGEVLQMSLNAATFLGQEPTVLRGQTLAALLPEQWPALQAALPPGCPDALQYRATLDWP
IFP2.0      47 HSGEVLQVSLNAATFLGQEPTVLRGQTLAALLPDQWPALQTALPPGCQDALQYRATLDWP
PENELOPE    47 HSGEVLQMSLNAATFLGQEPTVLRGQTLAALLPEQWPALQAALPPGCPDALQYRATLDWP

DrCBD      107 AAGHLSLTVHRVGELLILEFEPTEAWDSTGPHALRNAMFALESAPNLRALAEVATQTVRE
Wi-Phy     121 AAGHLSLTVHRVGELLILEFEPTEAWDSTGPHALRNAMSALESAPNLRALAEVATQTVRE
IFP2.0     107 AAGHLSLTVHRVAELLILEFEPTEAWDSIGPHALRNAMFALESAPNLRALAEVATQTVRE
PENELOPE   107 AAGHLSLTVHRVGELLILEFEPTEAWDSTGPHALRNAMSALESAPNLRALAEVATQTVWE

DrCBD      167 LTGFDRVMLYKFAPDATGEVIAEARREGLHAFLGHRFPASDIPAQARALYTRHLLRLTAD
Wi-Phy     181 LTGFDRVMLYKFAPDATGEVIAEARREGLHAFLGHRFPASHIPAQARALYTRHLLRLTAD
IFP2.0     167 LSGFDRVMLYKFAPDATGEVIAEARREGMQAMLGHRFPASTTPAQARALYTRHLLRLTAD
PENELOPE   167 LTGFDRVFLYKFAPDATGEVIAEARREGLHAFLGHRFPASDIPAQARALYTRHLLRLTAD

DrCBD      227 TRAAAVPLDPVLNPQTNAPTPLGGAVLRATSPMHMQYLRNMGVGSSLSVSVVVGGQLWGL
Wi-Phy     241 TRAAAVPLDPVLNPQTNAPTPLGGAVLRATSPMHMQFLRNMGVGSSLSVSVVVGGQLWGL
IFP2.0     227 TRAAAVPLDPVLNPQTNAPTPLGGAVLRATSPMHMQYLRNMGVGSSLSVSVVVGGQLWGL
PENELOPE   227 ARAAAVPLDPVLNPQTNAPTPLGGAVLRATSPMHMQYLRNMGVRSSLSVSVVVGGQLWGL

DrCBD      287 IACHHQTPYVLPPDLRTTLEYLGRLLSLQVQVKEA---------
Wi-Phy     301 IACHHQTPYVLPPDLRTTLEYLGRELSEQVQVKEA---------
IFP2.0     287 IVCHHQTPYVLPPDLRTTLEYLGRLLSLQVQRKEA---------
PENELOPE   287 IVCHHQTPYVLPPDLRTTLEYLGRELSEQVQVKEAADVAAFRQS
```

Figure 5.1: Sequence alignment of D.radiodurans-derived constitutively fluorescent FPs with PENELOPE.

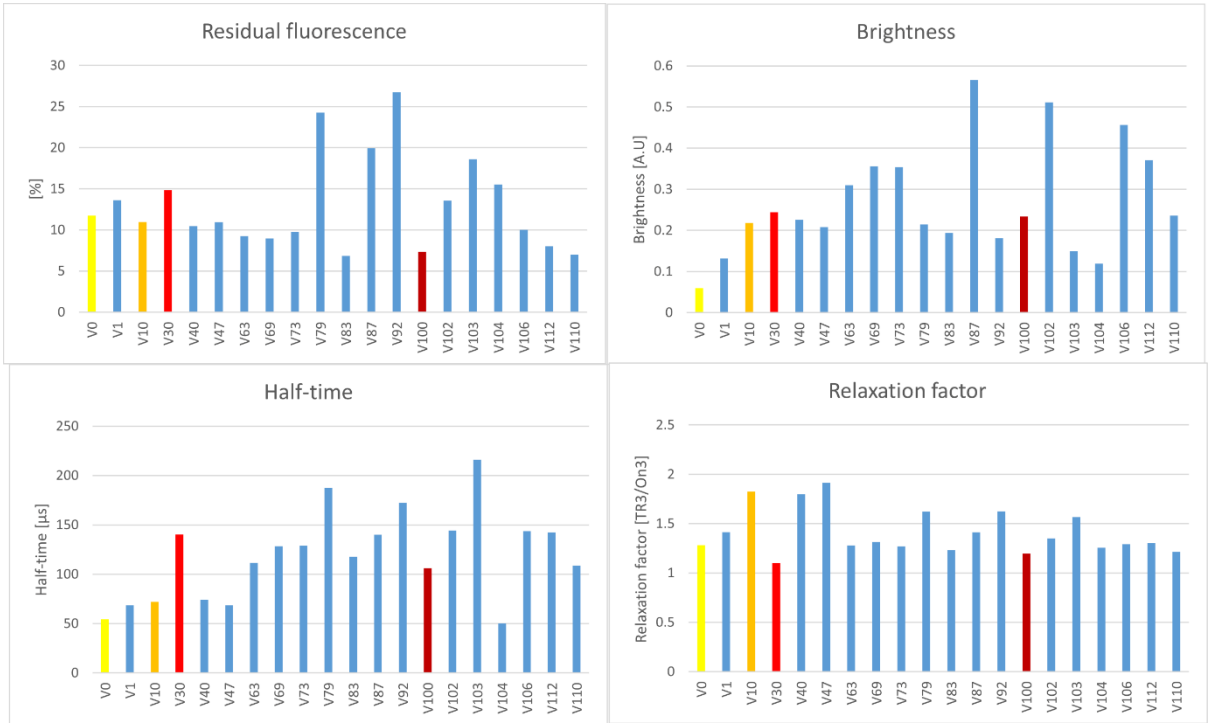

Figure 5.2: Overview of exemplary mutants of the generated bacteriophytochrome-derived RSFP library.

Relevant parameters include residual fluorescence, fluorescence brightness, off-switching halftime and relaxation factor.

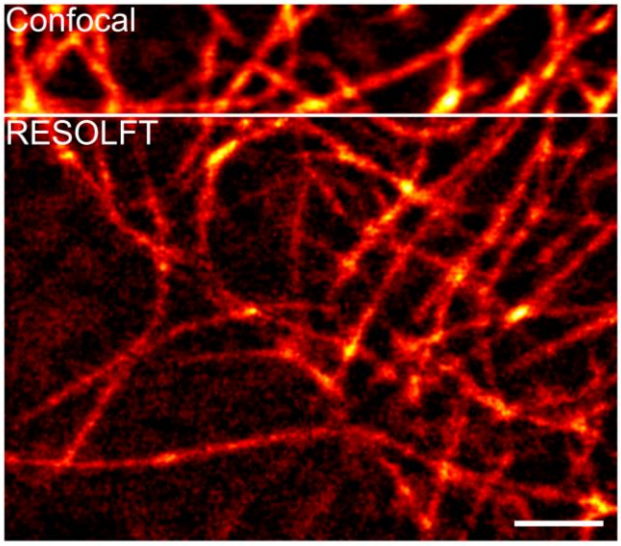

Figure 5.3: RESOLFT image of EB3-PENELOPE fusion constructs in transiently transfected HeLa cells. *Live HeLa cells were imaged with a 30 nm pixel size in pixel step mode. The confocal image was recorded prior to the RESOLFT image and was recorded with a pixel dwell-time of 6.13 ms, which consisted of a 5 ms thermal relaxation break and a 30 µs 660 nm illumination with 32 kW/cm2. The RESOLFT image was recorded with a sequential scheme consisting of a 5 ms thermal relaxation break, illumination with a 1.3 kW/cm^2 doughnut-shaped 660 nm off-switching laser for 1.1 ms and readout with a 32 kW/cm^2 Gaussian-shaped 660 nm laser for 30 µs. 25 µM BV was added 2 h before imaging. Due to high cellular fluorescence background, background subtraction including a 20 pixels wide rolling ball algorithm with was applied, followed by a convolution with a 1.2 pixel wide Gaussian function. Scale bar: 2 µm.*

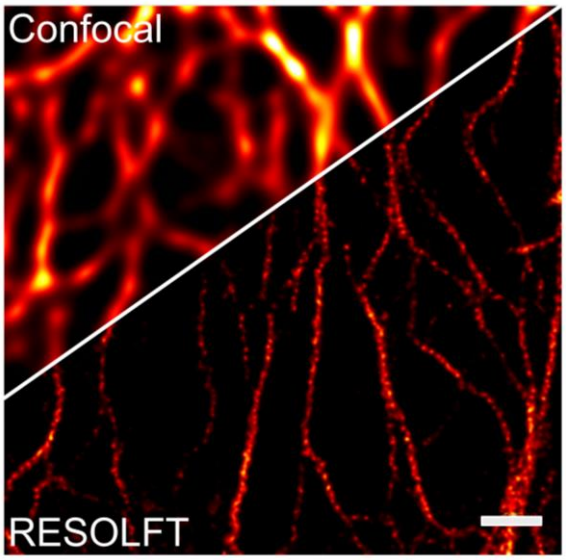

Figure 5.4: RESOLFT image of live stable Bxb1 landing pad cell line expressing cytokeratin18-PENELOPE*. Live HeLa cells were imaged with a 30 nm pixel size in pixel step mode. The confocal image was recorded simultaneously to the RESOLFT image. The total pixel dwell-time accounted for 10.72 ms. This total pixel dwell time consisted of a 5 ms thermal relaxation break and a 10 µs 660 nm illumination with 103 kW/cm2 to record the confocal image as well as a 5 ms thermal relaxation break, illumination with a 1.1 kW/cm2 doughnut-shaped 660 nm off-switching laser for 700 µs and readout with a 103 kW/cm2 Gaussian-shaped 660 nm laser for 10 µs to record the RESOLFT image. The image was deconvolved using the Huygens software*

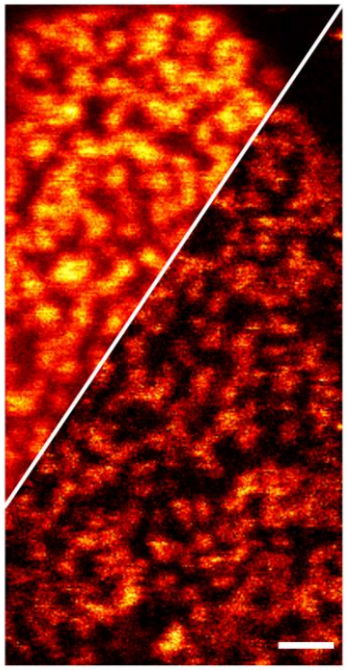

Figure 5.5: RESOLFT image of Nup50-PENELOPE fusion constructs in transiently transfected HeLa cells. *Live HeLa cells were imaged with a 30 nm pixel size in pixel step mode. The confocal image was recorded prior to the RESOLFT image and was recorded with a pixel dwell-time of 7.015 ms, which consisted of a 5 ms thermal relaxation break and a 15 µs 660 nm illumination with 118 kW/cm2. The RESOLFT image was recorded with a sequential scheme consisting of a 5 ms thermal relaxation break, illumination with a 1.7 kW/cm^2 doughnut-shaped 660 nm off-switching laser for 2 ms and readout with a 118 kW/cm^2 Gaussian-shaped 660 nm laser for 15 µs. 25 µM BV was added 2 h before imaging. Line accumulation was set to 5. Due to high cellular fluorescence background, background subtraction including a 20 pixels wide rolling ball algorithm with was applied, followed by a convolution with a 1.2 pixel wide Gaussian function. Scale bar: 2 µm.*

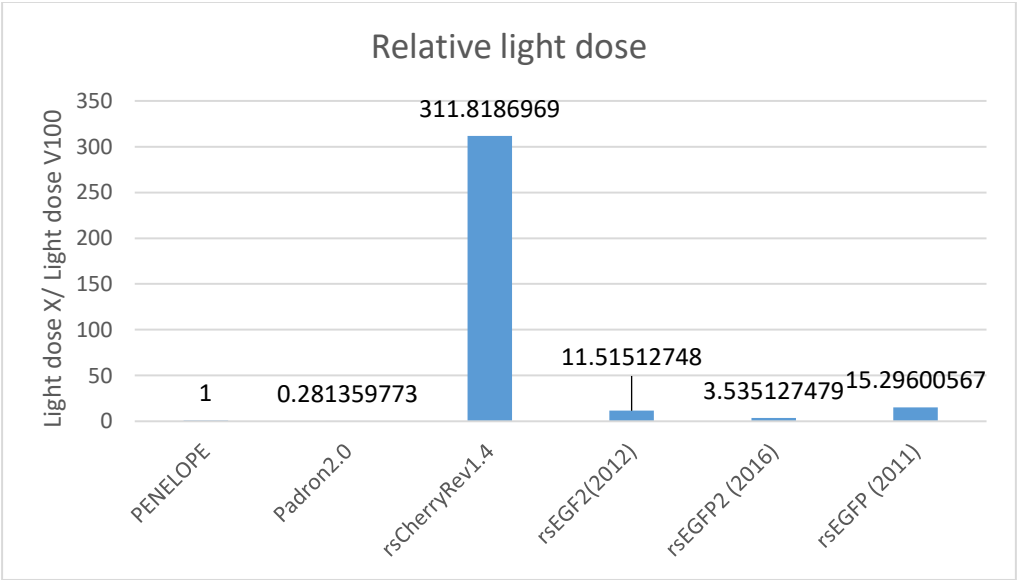

Figure 5.6: Comparison of applied loght doses in formation of publsihed RESOLFT images normalized to the light dose applied for PENELOPE.

Protein	Wavelengths	Line accumulation	Light intensity [kW/cm^2] (Time[µs])	Light dose [J/cm^2]	Dwell time [µs]
PENELOPE	660	1	0.6(700);80(5)	564	5.705
SNIFP	660,860	1	8(40);50000(40)	1.408.032	400
rsCherryRev1.4	430,591,561	1	0.8(500);37(10.000);1.6(500)	176.115	11.000
rsFusionRed3 (Scan)	405,591,561	1	24(500);9(5.000);16(100)	18.155	5.600
Padron2	405,488	1	23.1(70);1(350);1(120)	158	540
rsEGFP2 (2012)	405,488	2	5(20);34(360);76(20)	6.503	400
rsEGFP2 (2016)	405,488	2	2(170);6(380);24(10)	1.996	800
rsEGFP (2011)	405,488	1	1(100);1(10.000);1(1.000)	8.639	11.100

Figure 5.7: Overview of utilized wavelengths, line accumulations, light intensities, light doses and dwell times in VIS-RESOLFT, NIR-STED and NIR-RESOLFT experiments.

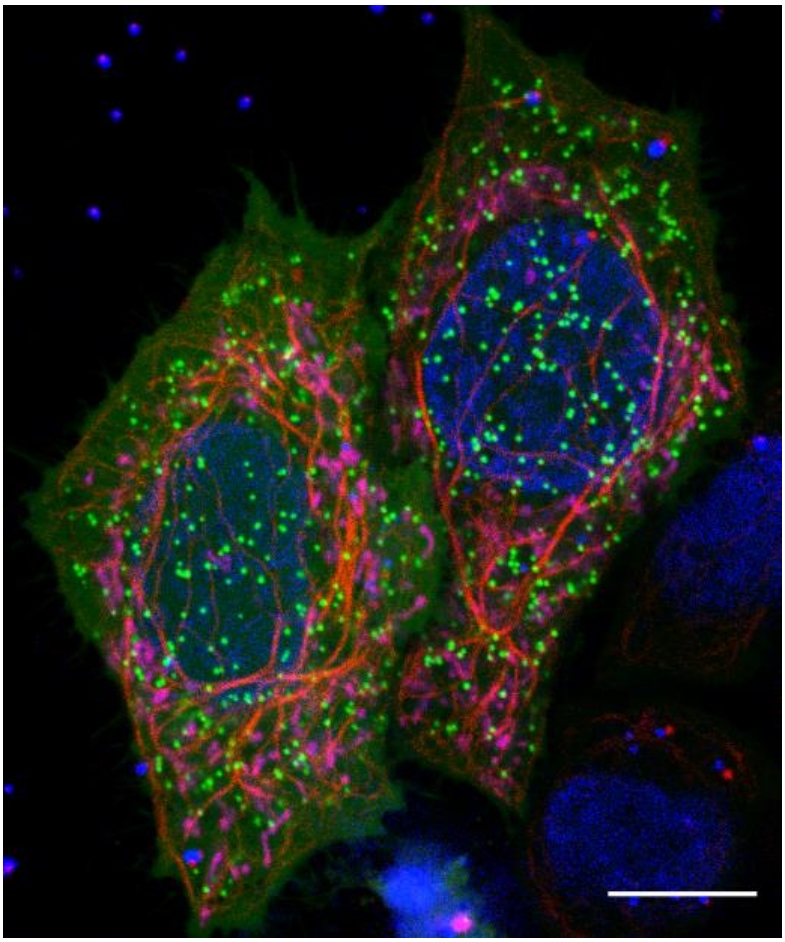

Figure 5.8: Multicolor imaging with PENELOPE. *Stably expressing cytokeratin18-PENELOPE HeLa cells were transftected with pMito-DsRd to visualize mitochondria in magenta and preoxisomes-mEGFP to visualize peroxsisomes. The nucleus was stained with Hoechst 33342. Cellular fluorescent background in the green channel is caused by cytsolic GFP-expressing of the Bxb1 cell line.*

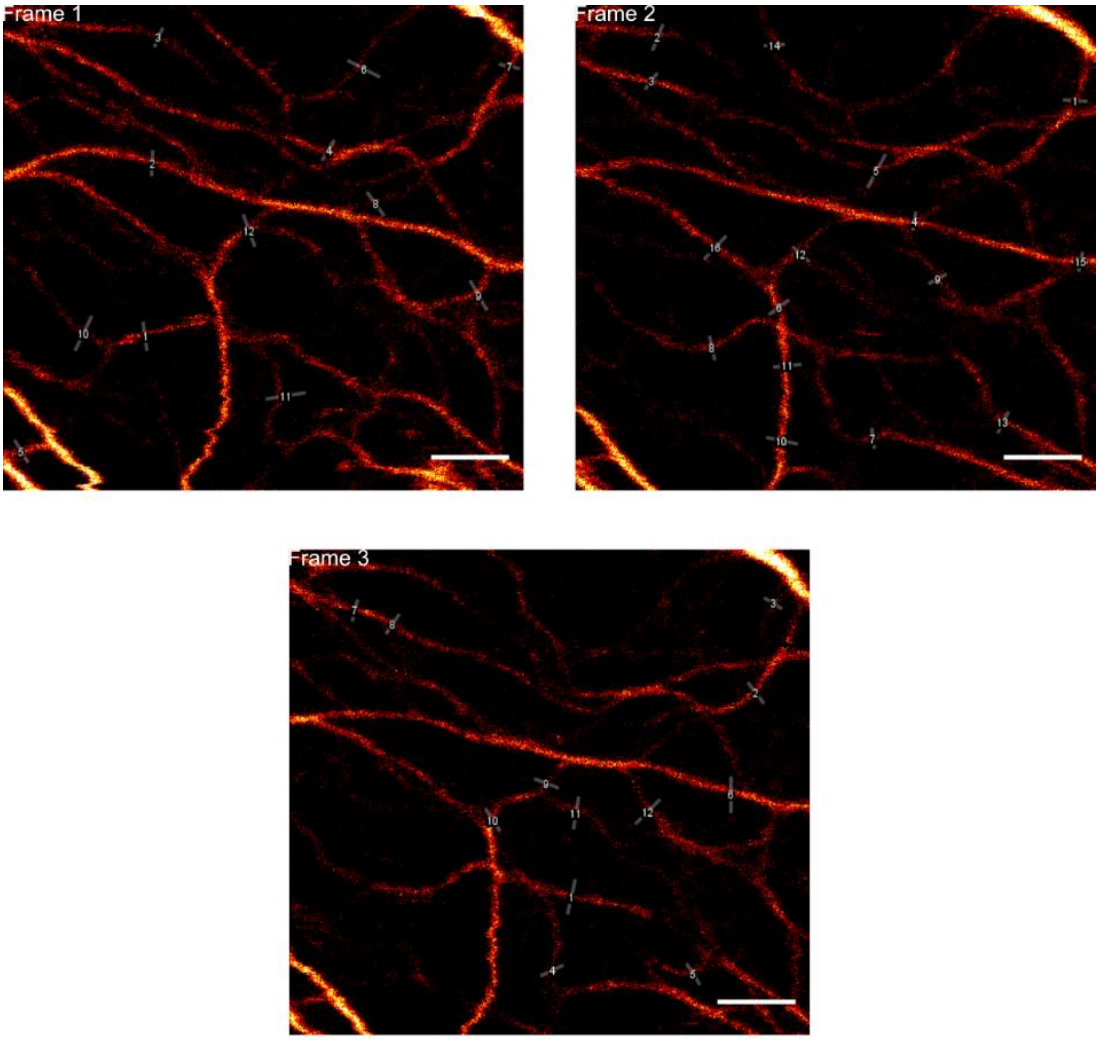

Lineprofile [Frame 1]	1	2	3	4	5	6	7	8	9	10	11	12
RESOLFT [FWHM]	64	64	72	70	65	90	53	97	96	76	129	99

Lineprofile [Frame 2]	1	2	3	4	5	6	7	8	9	10	11	12
RESOLFT [FWHM]	71	79	54	63	104	115	79	85	82	88	83	131

Lineprofile [Frame 3]	1	3	6	7	8	9	10	13	15	16
RESOLFT [FWHM]	74	69	89	56	95	89	116	83	104	71

Figure 5.9: RESOLFT time lapse imaging of live stable Bxb1 landing pad cell line expressing Cytokeratin18-PENELOPE. *Live HeLa cells were imaged with a 30 nm pixel size in pixel step mode. The confocal image was recorded simultaneously to the RESOLFT image. The total pixel dwell-time accounted for 10.72 ms. This total pixel dwell time consisted of a 5 ms thermal relaxation break and a 10 µs 660 nm illumination with 103 kW/cm^2 to record the confocal image as well as a 5 ms thermal relaxation break, illumination with a 1.1 kW/cm^2 doughnut-shaped 660 nm off-switching laser for 700 µs and readout with a 103 kW/cm^2 Gaussian-shaped 660 nm laser for 10 µs to record the RESOLFT image. The FWHM values of the respective line profiles are displayed in the table below. Every table line represents a FWHMs of a new frame. 25 µM BV was added 2 h before imaging. Scale bar: 2 µm.*

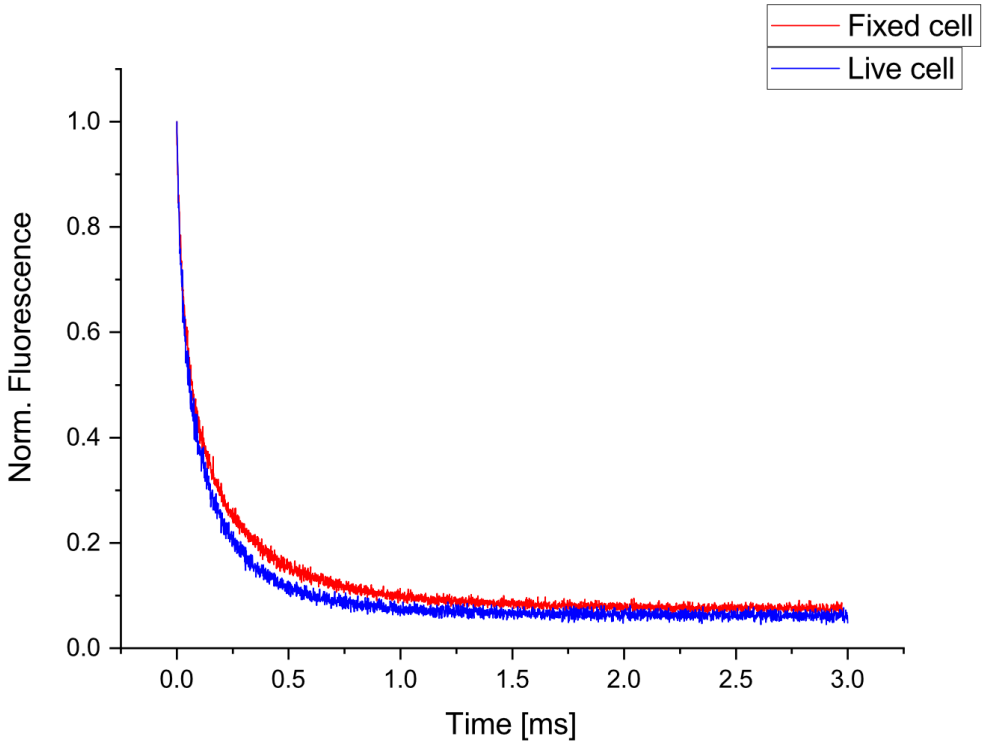

Figure 5.10: Raw data switching curves of PENELOPE-cytokeratin18 recorded in live and fixed mammalian cells.

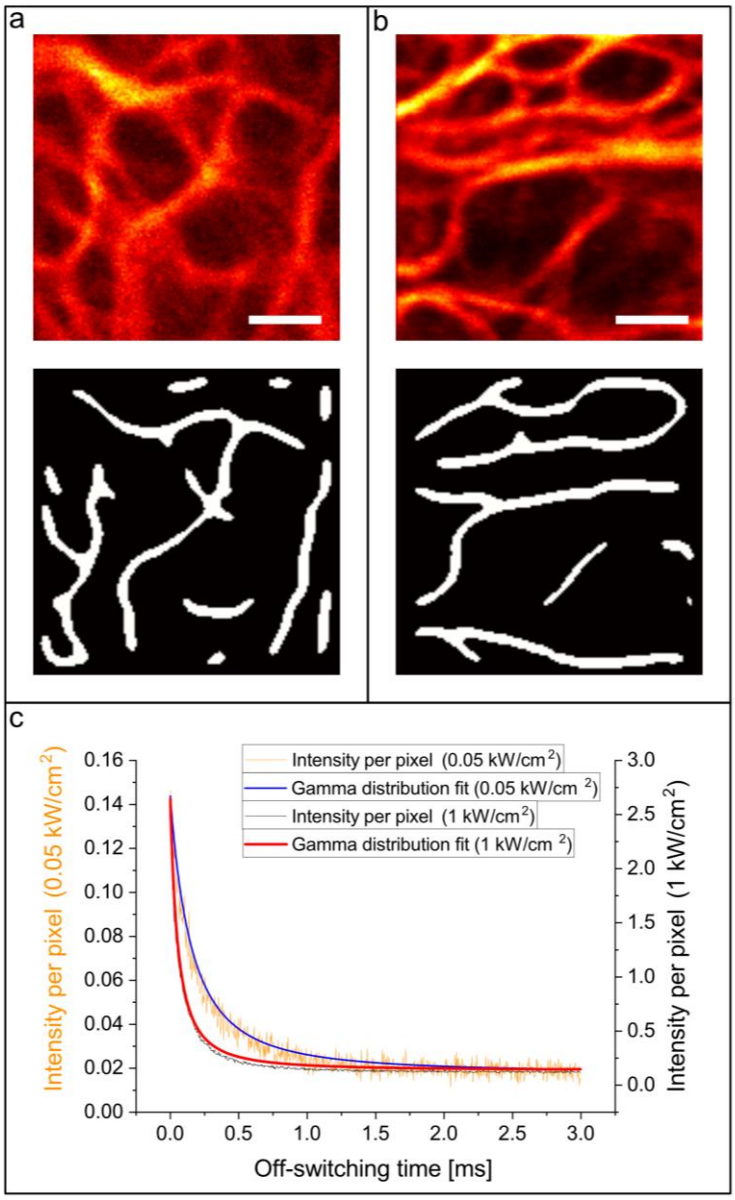

Figure 5.11: Intensity dependence in raw data off-switching curves recorded in mammalian cells. *(a) Recorded confocal image and applied structure mask. The image was recorded with 0.05 kW/cm². (b) Recorded confocal image and applied structure mask. The image was recorded with 1 kW/cm2. (c) Comparative analysis of off-switching data at 0.05 kW/cm² (yellow) and 1 kW/cm² (black). A gamma fit was applied to the raw off-switching data for 0.05 kW/cm2 (blue) and 1 kW/cm2 (red). Scale bar: 1µm*

Table 5.1: Mutagenesis primers

9136 W3_T20/21X	GGTGGCCCCGAGATTNDTTBKGAGAACTGCCAAAGG
9138 W3_C24X_N23C	GAGATTACGACTGAGTGCNNNCAAAGGGAACCCATCCAC
9140 W3_C24X_E25C	ACGACTGAGAACNNNTGTAGGGAACCCATCCACATTCCG
9142 W3_H196X/F198X	GAAGCGCGCAGAGAAGGACTGDBKGCGNDTCTGGGGCATAGGTTTCCG
9144 W3_H201X/F203X	CTGCACGCGTTTCTGGGGDBKAGGNDTCCGGCTTCTGACATTCCCGCA
9253 W3.50_M174X	GGCTTCGATCGTGTANNNCTGTACAAGTTCGCA
9255 W3.50_G184X	GCACCCGATGCTACANNNGAGGTGATCGCTGAA
9257 W3.50_DIP/XXX	GGGCATAGGTTTCCGGCTTCTDBKNDTDBKGCACAAGCTAGGGCCCTC
9259 W3.50_L286X	GGGCAACTGTGGGGCNNNATTGCCTGTCACCAC
9262 W3.50_C24X	ATTACGACTGAGAACNNNCAAAGGGAACCCATC
9264 W3.50_E320STOP	CAGGTGCAAGTCAAATAAGCCGCGGATGTTGCC
9266 W3.50_A322STOP	CAAGTCAAAGAGGCCTAAGATGTTGCCGCCTTT
9268 W3.50_V324STOP	AAAGAGGCCGCGGATTAAGCCGCCTTTCGCCAG
9270 W3.50_A326STOP	GCCGCGGATGTTGCCTAATTTCGCCAGAGTTAA
9274 W3.50_F203P/P204X	TTTCTGGGGCATAGGCCTNNNGCTTCTGACATT
9276W3.50_P204X	CTGGGGCATAGGTTTNNNGCTTCTGACATTCCC
9278 W3.50_P204X/A205P	CTGGGGCATAGGTTTNNNCCTTCTGACATTCCC
9288 W3.50_S257C	GTGCTGCGCGCCACTTGTCCCATGCACATGCAG
9290 W3.50_M259C	CGCGCCACTAGCCCCTGCCACATGCAGTACCTC
9298 W3.50_L199-R202/Helix	GGACTGCACGCGTTTCTGGRHGRHGRHTTTCCGGCTTCTGACATT
Wi-Phy_EP_fwd	TACGTCGACGATGTCCCGTGACCCTCT
Wi-Phy_EP_rev	CAGCCAAGCTTCGAATTCTTA
W4.35-S257C	GCTGTGCTGCGCGCCACTTGCCCCATGCACATGCAGTTC
W4.35-M259C	CTGCGCGCCACTAGCCCCTGCCACATGCAGTTCCTCCGG
W4.35-S257C/M259C	GGGGCTGTGCTGCGCGCCACTTGCCCCTGCCACATGCAGTTCCTCCGG

6 List of figures

7 List of tables

8 References

[1] Lockyer, N., *Nature*. 1876: Macmillan Journals Limited.

[2] Hooke, R., *Micrographia, or, Some physiological descriptions of minute bodies made by magnifying glasses : with observations and inquiries thereupon.* London : Printed for James Allestry, printer to the Royal Society, and to be sold at his shop, at the Rose and Crown in Duck-Lane, 1667.

[3] Stokes, G.G., *On the Change of Refrangibility of Light.* Philosophical Transactions of the Royal Society of London 1852. **142**: p. 463-562.

[4] Kanan, S.M. and A. Malkawi, *Recent Advances in Nanocomposite Luminescent Metal-Organic Framework Sensors for Detecting Metal Ions.* Comments on Inorganic Chemistry, 2021. **41**(1): p. 1-66.

[5] Jablonski, A., *Efficiency of Anti-Stokes Fluorescence in Dyes.* Nature, 1933. **131**: p. 839-840.

[6] Albani, J.R., *Structure and Dynamics of Macromolecules: Absorption and Fluorescence Studies*. 2011: Elsevier Science.

[7] Kubitscheck, U., *Fluorescence Microscopy: From Principles to Biological Applications, Second Edition.* Wiley-VCH Verlag GmbH & Co. KGaA, 2017.

[8] C. J. R. Sheppard, T.W., *The theory of the direct-view confocal microscope.* Journal of Microscopy, 1981. **124**(2): p. 107-117.

[9] Kitamura, A., *Pinhole Closure Improves Spatial Resolution in Confocal Scanning Microscopy.* Methods Mol Biol, 2021. **2274**: p. 385-389.

[10] Monici, M., *Cell and tissue autofluorescence research and diagnostic applications.* Biotechnol Annu Rev, 2005. **11**: p. 227-256.

[11] Guo, H.W., et al., *Hemoglobin autofluorescence as potential long-term glycemic marker in the rat animal model.* J Biophotonics, 2021. **14**(9): p. e202000389.

[12] Croce, A.C. and G. Bottiroli, *Autofluorescence Spectroscopy for Monitoring Metabolism in Animal Cells and Tissues*, in *Histochemistry of Single Molecules: Methods and Protocols*, C. Pellicciari and M. Biggiogera, Editors. 2017, Springer New York: New York, NY. p. 15-43.

[13] E.Abbe, *Beiträge zur Theorie des Mikroskops und der mikroskopischen Wahrnehmung.* Archiv für Mikroskopische Anatomie, 1873. **9**: p. 413-468.

[14] Richards, B. and E. Wolf, *Electromagnetic Diffraction in Optical Systems. II. Structure of the Image Field in an Aplanatic System.* Proceedings of the Royal Society of London. Series A, Mathematical and Physical Sciences, 1959. **253**(1274): p. 358-379.

[15] Rayleigh, L., *XII. On the manufacture and theory of diffraction-gratings.* The London, Edinburgh, and Dublin Philosophical Magazine and Journal of Science, 1874. **47**(310): p. 81-93.

[16] Airy, G.B., *On the Diffraction of an Object-glass with Circular Aperture.* Transactions of the Cambridge Philosophical Society, 1835. **5**: p. 283.

[17] Maraloiu, V.-A., *A multiscale study of magnetic nanovectors : application to USPIO contrast agents for MRI of atherotic inflammation in a murine model*. 2010.

[18] Cremer, C. and T. Cremer, *Considerations on a laser-scanning-microscope with high resolution and depth of field.* Microsc Acta, 1978. **81**(1): p. 31-44.

[19] Guerra, J.M., *Super-resolution through illumination by diffraction-born evanescent waves.* Applied Physics Letters, 1995. **66**(26): p. 3555-3557.

[20] Markwirth, A., et al., *Video-rate multi-color structured illumination microscopy with simultaneous real-time reconstruction.* Nat Commun, 2019. **10**(1): p. 4315.

[21] Gustafsson, M.G., *Surpassing the lateral resolution limit by a factor of two using structured illumination microscopy.* J Microsc, 2000. **198**(Pt 2): p. 82-7.

[22] von Diezmann, L., Y. Shechtman, and W.E. Moerner, *Three-Dimensional Localization of Single Molecules for Super-Resolution Imaging and Single-Particle Tracking.* Chem Rev, 2017. **117**(11): p. 7244-7275.

[23] Rust, M.J., M. Bates, and X. Zhuang, *Sub-diffraction-limit imaging by stochastic optical reconstruction microscopy (STORM).* Nat Methods, 2006. **3**(10): p. 793-5.

[24] Endesfelder, U. and M. Heilemann, *Direct stochastic optical reconstruction microscopy (dSTORM).* Methods Mol Biol, 2015. **1251**: p. 263-76.

[25] Hess, S.T., T.P.K. Girirajan, and M.D. Mason, *Ultra-High Resolution Imaging by Fluorescence Photoactivation Localization Microscopy.* Biophysical Journal, 2006. **91**(11): p. 4258-4272.

[26] Hell, S.W. and M. Kroug, *Ground-state-depletion fluorscence microscopy: A concept for breaking the diffraction resolution limit.* Applied Physics B, 1995. **60**: p. 495-497.

[27] Betzig, E., et al., *Imaging intracellular fluorescent proteins at nanometer resolution.* Science, 2006. **313**(5793): p. 1642-5.

[28] Thompson, R.E., D.R. Larson, and W.W. Webb, *Precise Nanometer Localization Analysis for Individual Fluorescent Probes.* Biophysical Journal, 2002. **82**(5): p. 2775-2783.

[29] Sigal, Y.M., R. Zhou, and X. Zhuang, *Visualizing and discovering cellular structures with super-resolution microscopy.* Science, 2018. **361**(6405): p. 880-887.

[30] Shroff, H., et al., *Live-cell photoactivated localization microscopy of nanoscale adhesion dynamics.* Nat Methods, 2008. **5**(5): p. 417-23.

[31] Vandenberg, W., et al., *Diffraction-unlimited imaging: from pretty pictures to hard numbers.* Cell Tissue Res, 2015. **360**(1): p. 151-78.

[32] Khater, I.M., I.R. Nabi, and G. Hamarneh, *A Review of Super-Resolution Single-Molecule Localization Microscopy Cluster Analysis and Quantification Methods.* Patterns (N Y), 2020. **1**(3): p. 100038.

[33] Willig, K.I., et al., *Nanoscale resolution in GFP-based microscopy.* Nat Methods, 2006. **3**(9): p. 721-3.

[34] Hell, S.W., *Fluorescence nanoscopy: Breaking the diffraction barrier by the RESOLFT concept.* NanoBiotechnology, 2005. **1**(3): p. 296-297.

[35] Hell, S.W. and J. Wichmann, *Breaking the diffraction resolution limit by stimulated emission: stimulated-emission-depletion fluorescence microscopy.* Optics Letters, 1994. **19**(11): p. 780-782.

[36] Frahm, L., et al., *Molecular contribution function in RESOLFT nanoscopy.* Opt Express, 2019. **27**(15): p. 21956-21987.

[37] Hell, S.W., S. Jakobs, and L. Kastrup, *Imaging and writing at the nanoscale with focused visible light through saturable optical transitions.* Applied Physics A, 2003. **77**(7): p. 859-860.

[38] Hell, S.W., M. Dyba, and S. Jakobs, *Concepts for nanoscale resolution in fluorescence microscopy.* Curr Opin Neurobiol, 2004. **14**(5): p. 599-609.

[39] Eilers, Y., et al., *MINFLUX monitors rapid molecular jumps with superior spatiotemporal resolution.* Proceedings of the National Academy of Sciences, 2018. **115**(24): p. 6117-6122.

[40] Balzarotti, F., et al., *Nanometer resolution imaging and tracking of fluorescent molecules with minimal photon fluxes.* Science, 2017. **355**(6325): p. 606-612.

[41] Gwosch, K.C., et al., *MINFLUX nanoscopy delivers 3D multicolor nanometer resolution in cells.* Nat Methods, 2020. **17**(2): p. 217-224.

[42] Dyba, M. and S.W. Hell, *Photostability of a fluorescent marker under pulsed excited-state depletion through stimulated emission.* Applied Optics, 2003. **42**(25): p. 5123-5129.

[43] Bouzin, M., et al., *Stimulated Emission Properties of Fluorophores by CW-STED Single Molecule Spectroscopy.* The Journal of Physical Chemistry B, 2013. **117**(51): p. 16405-16415.

[44] Hotta, J.-i., et al., *Spectroscopic Rationale for Efficient Stimulated-Emission Depletion Microscopy Fluorophores.* Journal of the American Chemical Society, 2010. **132**(14): p. 5021-5023.

[45] Kilian, N., et al., *Assessing photodamage in live-cell STED microscopy.* Nature methods, 2018. **15**(10): p. 755-756.

[46] Grotjohann, T., et al., *Diffraction-unlimited all-optical imaging and writing with a photochromic GFP*. Nature, 2011. **478**(7368): p. 204-8.

[47] Grotjohann, T., et al., *rsEGFP2 enables fast RESOLFT nanoscopy of living cells.* eLife, 2012. **1**: p. e00248.

[48] Chmyrov, A., et al., *Nanoscopy with more than 100,000 'doughnuts'*. Nature Methods, 2013. **10**(8): p. 737-740.

[49] Masullo, L.A., et al., *Enhanced photon collection enables four dimensional fluorescence nanoscopy of living systems.* Nature Communications, 2018. **9**(1): p. 3281.

[50] Chmyrov, A., et al., *Achromatic light patterning and improved image reconstruction for parallelized RESOLFT nanoscopy.* Scientific Reports, 2017. **7**: p. 44619.

[51] Crivat, G. and J.W. Taraska, *Imaging proteins inside cells with fluorescent tags.* Trends in biotechnology, 2012. **30**(1): p. 8-16.

[52] Lukinavičius, G., et al., *A near-infrared fluorophore for live-cell super-resolution microscopy of cellular proteins.* Nature Chemistry, 2013. **5**(2): p. 132-139.

[53] Shimomura, O., F.H. Johnson, and Y. Saiga, *Extraction, purification and properties of aequorin, a bioluminescent protein from the luminous hydromedusan, Aequorea.* J Cell Comp Physiol, 1962. **59**: p. 223-39.

[54] Chalfie, M., et al., *Green fluorescent protein as a marker for gene expression.* Science, 1994. **263**(5148): p. 802-5.

[55] Ormö, M., et al., *Crystal structure of the Aequorea victoria green fluorescent protein.* Science, 1996. **273**(5280): p. 1392-5.

[56] Yang, F., L.G. Moss, and G.N. Phillips, *The molecular structure of green fluorescent protein.* Nature Biotechnology, 1996. **14**(10): p. 1246-1251.

[57] Tsien, R.Y., *THE GREEN FLUORESCENT PROTEIN.* Annual Review of Biochemistry, 1998. **67**(1): p. 509-544.

[58] Matz, M.V., et al., *Fluorescent proteins from nonbioluminescent Anthozoa species.* Nat Biotechnol, 1999. **17**(10): p. 969-73.

[59] Ando, R., H. Mizuno, and A. Miyawaki, *Regulated fast nucleocytoplasmic shuttling observed by reversible protein highlighting.* Science, 2004. **306**(5700): p. 1370-3.

[60] Tomosugi, W., et al., *An ultramarine fluorescent protein with increased photostability and pH insensitivity.* Nat Methods, 2009. **6**(5): p. 351-3.

[61] Li, Z., et al., *Mutagenesis of mNeptune Red-Shifts Emission Spectrum to 681-685 nm.* PLoS One, 2016. **11**(4): p. e0148749.

[62] Shaner, N.C., et al., *A bright monomeric green fluorescent protein derived from Branchiostoma lanceolatum.* Nat Methods, 2013. **10**(5): p. 407-9.

[63] Mizuno, H., et al., *Light-dependent regulation of structural flexibility in a photochromic fluorescent protein.* Proceedings of the National Academy of Sciences, 2008. **105**(27): p. 9227-9232.

[64] Stiel, Andre C., et al., *1.8 Å bright-state structure of the reversibly switchable fluorescent protein Dronpa guides the generation of fast switching variants.* Biochemical Journal, 2007. **402**(1): p. 35-42.

[65] Andresen, M., et al., *Structure and mechanism of the reversible photoswitch of a fluorescent protein.* Proc Natl Acad Sci U S A, 2005. **102**(37): p. 13070-4.

[66] Andresen, M., et al., *Structural basis for reversible photoswitching in Dronpa.* Proceedings of the National Academy of Sciences, 2007. **104**(32): p. 13005-13009.

[67] Woodhouse, J., et al., *Photoswitching mechanism of a fluorescent protein revealed by time-resolved crystallography and transient absorption spectroscopy.* Nature Communications, 2020. **11**(1): p. 741.

[68] Duan, C., et al., *Structural Basis of Photoswitching in Fluorescent Proteins*, in *Photoswitching Proteins: Methods and Protocols*, S. Cambridge, Editor. 2014, Springer New York: New York, NY. p. 177-202.

[69] Woodhouse, J., et al., *Photoswitching mechanism of a fluorescent protein revealed by time-resolved crystallography and transient absorption spectroscopy.* Nature communications, 2020. **11**(1): p. 741-741.

[70] Chang, J., M.G. Romei, and S.G. Boxer, *Structural Evidence of Photoisomerization Pathways in Fluorescent Proteins.* Journal of the American Chemical Society, 2019. **141**(39): p. 15504-15508.

[71] Schüttrigkeit, T.A., et al., *Femtosecond study of light-induced fluorescence increase of the dark chromoprotein asFP595.* Chemical Physics, 2006. **323**(2): p. 149-160.

[72] Li, X., et al., *Primary Events of Photodynamics in Reversible Photoswitching Fluorescent Protein Dronpa.* The Journal of Physical Chemistry Letters, 2010. **1**(23): p. 3328-3333.

[73] Costantini, L.M., et al., *Assessing the Tendency of Fluorescent Proteins to Oligomerize Under Physiologic Conditions.* Traffic, 2012. **13**(5): p. 643-649.

[74] Jensen, N.A., et al., *Coordinate-Targeted and Coordinate-Stochastic Super-Resolution Microscopy with the Reversibly Switchable Fluorescent Protein Dreiklang.* ChemPhysChem, 2014. **15**(4): p. 756-762.

[75] Shemetov, A.A., O.S. Oliinyk, and V.V. Verkhusha, *How to Increase Brightness of Near-Infrared Fluorescent Proteins in Mammalian Cells.* Cell Chem Biol, 2017. **24**(6): p. 758-766 e3.

[76] Waldchen, S., et al., *Light-induced cell damage in live-cell super-resolution microscopy.* Sci Rep, 2015. **5**: p. 15348.

[77] Demir Duman, F. and H. Acar, *Development of Near Infrared Emitting Cationic Ag2S Quantum Dots as Drug-Gene Delivery and Optical Imaging Agents*. 2017.

[78] Li, J., et al., *Phytochrome Signaling Mechanisms.* The Arabidopsis Book, 2011. **2011**(9).

[79] Verma, R.K., et al., *A Bacteriophytochrome Mediates Interplay between Light Sensing and the Second Messenger Cyclic Di-GMP to Control Social Behavior and Virulence.* Cell Rep, 2020. **32**(13): p. 108202.

[80] Burgie, E.S. and R.D. Vierstra, *Phytochromes: An Atomic Perspective on Photoactivation and Signaling.* Plant Cell, 2014. **26**(12): p. 4568-4583.

[81] Rockwell, N.C., Y.S. Su, and J.C. Lagarias, *Phytochrome structure and signaling mechanisms.* Annu Rev Plant Biol, 2006. **57**: p. 837-58.

[82] Fischer, A.J. and J.C. Lagarias, *Harnessing phytochrome's glowing potential.* Proceedings of the National Academy of Sciences, 2004. **101**(50): p. 17334-17339.

[83] Terry, M.J., *Biosynthesis and Analysis of Bilins*, in *Heme, Chlorophyll, and Bilins: Methods and Protocols*, A.G. Smith and M. Witty, Editors. 2002, Humana Press: Totowa, NJ. p. 273-291.

[84] Kadish, K., K. Smith, and R. Guilard, *The Porphyrin Handbook: Chlorophylls and Bilins: Biosynthesis, Synthesis and Degradation*. 2012. 1-281.

[85] Burgie, E.S. and R.D. Vierstra, *Phytochromes: an atomic perspective on photoactivation and signaling.* Plant Cell, 2014. **26**(12): p. 4568-83.

[86] Takala, H., et al., *Signal amplification and transduction in phytochrome photosensors.* Nature, 2014. **509**(7499): p. 245-+.

[87] Zhu, W., A. Wilks, and I. Stojiljkovic, *Degradation of heme in gram-negative bacteria: the product of the hemO gene of Neisseriae is a heme oxygenase.* J Bacteriol, 2000. **182**(23): p. 6783-90.

[88] Wang, J. and P.R. de Montellano, *The binding sites on human heme oxygenase-1 for cytochrome p450 reductase and biliverdin reductase.* J Biol Chem, 2003. **278**(22): p. 20069-76.

[89] Otterbein, L.E., et al., *Heme oxygenase-1: unleashing the protective properties of heme.* Trends Immunol, 2003. **24**(8): p. 449-55.

[90] Shu, X., et al., *Mammalian expression of infrared fluorescent proteins engineered from a bacterial phytochrome.* Science, 2009. **324**(5928): p. 804-7.

[91] Greenberg, A.J., I. Bossenmaier, and S. Schwartz, *Green jaundice.* The American Journal of Digestive Diseases, 1971. **16**(10): p. 873-880.

[92] Gourinchas, G., S. Etzl, and A. Winkler, *Bacteriophytochromes - from informative model systems of phytochrome function to powerful tools in cell biology.* Current opinion in structural biology, 2019. **57**: p. 72-83.

[93] Bhoo, S.H., et al., *Bacteriophytochromes are photochromic histidine kinases using a biliverdin chromophore.* Nature, 2001. **414**(6865): p. 776-9.

[94] Essen, L.-O., J. Mailliet, and J. Hughes, *The structure of a complete phytochrome sensory module in the Pr ground state.* Proceedings of the National Academy of Sciences, 2008. **105**(38): p. 14709-14714.

[95] Wagner, J.R., et al., *A light-sensing knot revealed by the structure of the chromophore-binding domain of phytochrome.* Nature, 2005. **438**(7066): p. 325-31.

[96] Burgie, E.S., et al., *Crystal structure of the photosensing module from a red/far-red light-absorbing plant phytochrome.* Proceedings of the National Academy of Sciences, 2014. **111**(28): p. 10179-10184.

[97] Stepanenko, O.V., et al., *A knot in the protein structure - probing the near-infrared fluorescent protein iRFP designed from a bacterial phytochrome.* FEBS J, 2014. **281**(9): p. 2284-98.

[98] Buhrke, D., et al., *Chromophore binding to two cysteines increases quantum yield of near-infrared fluorescent proteins.* Sci Rep, 2019. **9**(1): p. 1866.

[99] Takala, H., et al., *Light-induced Changes in the Dimerization Interface of Bacteriophytochromes.* J Biol Chem, 2015. **290**(26): p. 16383-92.

[100] Burgie, E.S., et al., *Crystallographic and electron microscopic analyses of a bacterial phytochrome reveal local and global rearrangements during photoconversion.* J Biol Chem, 2014. **289**(35): p. 24573-87.

[101] Woitowich, N.C., et al., *Structural basis for light control of cell development revealed by crystal structures of a myxobacterial phytochrome.* IUCrJ, 2018. **5**(Pt 5): p. 619-634.

[102] Anders, K., et al., *Structure of the cyanobacterial phytochrome 2 photosensor implies a tryptophan switch for phytochrome signaling.* J Biol Chem, 2013. **288**(50): p. 35714-25.

[103] Wagner, J.R., et al., *Mutational analysis of Deinococcus radiodurans bacteriophytochrome reveals key amino acids necessary for the photochromicity and proton exchange cycle of phytochromes.* J Biol Chem, 2008. **283**(18): p. 12212-26.

[104] Auldridge, M.E., et al., *Structure-guided engineering enhances a phytochrome-based infrared fluorescent protein.* J Biol Chem, 2012. **287**(10): p. 7000-9.

[105] Song, C., et al., *Two ground state isoforms and a chromophore D-ring photoflip triggering extensive intramolecular changes in a canonical phytochrome.* Proceedings of the National Academy of Sciences, 2011. **108**(10): p. 3842-3847.

[106] Björling, A., et al., *Ubiquitous Structural Signaling in Bacterial Phytochromes.* The Journal of Physical Chemistry Letters, 2015. **6**(17): p. 3379-3383.

[107] Mroginski, M.A., D.H. Murgida, and P. Hildebrandt, *The chromophore structural changes during the photocycle of phytochrome: a combined resonance Raman and quantum chemical approach.* Acc Chem Res, 2007. **40**(4): p. 258-66.

[108] Robben, U., I. Lindner, and W. Gartner, *New open-chain tetrapyrroles as chromophores in the plant photoreceptor phytochrome.* J Am Chem Soc, 2008. **130**(34): p. 11303-11.

[109] Yang, Y., et al., *Real-time tracking of phytochrome's orientational changes during Pr photoisomerization.* J Am Chem Soc, 2012. **134**(3): p. 1408-11.

[110] Vierstra, R.D. and J. Zhang, *Phytochrome signaling: solving the Gordian knot with microbial relatives.* Trends Plant Sci, 2011. **16**(8): p. 417-26.

[111] van Thor, J.J., K.L. Ronayne, and M. Towrie, *Formation of the early photoproduct lumi-R of cyanobacterial phytochrome cph1 observed by ultrafast mid-infrared spectroscopy.* J Am Chem Soc, 2007. **129**(1): p. 126-32.

[112] Wang, C., et al., *Bacteriophytochrome Photoisomerization Proceeds Homogeneously Despite Heterogeneity in Ground State.* Biophys J, 2016. **111**(10): p. 2125-2134.

[113] Mroginski, M.A., D.H. Murgida, and P. Hildebrandt, *The chromophore structural changes during the photocycle of phytochrome: A combined resonance raman and quantum chemical approach.* Accounts of Chemical Research, 2007. **40**(4): p. 258-266.

[114] Dasgupta, J., et al., *Ultrafast excited-state isomerization in phytochrome revealed by femtosecond stimulated Raman spectroscopy.* Proc Natl Acad Sci U S A, 2009. **106**(6): p. 1784-9.

[115] Mathes, T., et al., *Femto- to Microsecond Photodynamics of an Unusual Bacteriophytochrome.* Journal of Physical Chemistry Letters, 2015. **6**(2): p. 239-243.

[116] Wagner, J.R., et al., *Mutational analysis of Deinococcus radiodurans bacteriophytochrome reveals key amino acids necessary for the photochromicity and proton exchange cycle of phytochromes.* Journal of Biological Chemistry, 2008. **283**(18): p. 12212-12226.

[117] Yang, X.J., et al., *Temperature-scan cryocrystallography reveals reaction intermediates in bacteriophytochrome.* Nature, 2011. **479**(7373): p. 428-U190.

[118] Wang, C., et al., *Bacteriophytochrome Photoisomerization Proceeds Homogeneously Despite Heterogeneity in Ground State.* Biophysical Journal, 2016. **111**(10): p. 2125-2134.

[119] Frankland, B., *Biosynthesis and dark transformations of phytochrome.* 1972. **1972**: p. 195-225.

[120] Takala, H., et al., *Connection between Absorption Properties and Conformational Changes in Deinococcus radiodurans Phytochrome.* Biochemistry, 2014. **53**(45): p. 7076-7085.

[121] Kamper, M., et al., *Near-infrared STED nanoscopy with an engineered bacterial phytochrome.* Nature Communications, 2018. **9**(1): p. 4762.

[122] Bellini, D. and M.Z. Papiz, *Structure of a bacteriophytochrome and light-stimulated protomer swapping with a gene repressor.* Structure, 2012. **20**(8): p. 1436-46.

[123] Shcherbakova, D.M., et al., *Bright monomeric near-infrared fluorescent proteins as tags and biosensors for multiscale imaging.* Nat Commun, 2016. **7**: p. 12405.

[124] Matlashov, M.E., et al., *A set of monomeric near-infrared fluorescent proteins for multicolor imaging across scales.* Nat Commun, 2020. **11**(1): p. 239.

[125] Lambert, T.J., *FPbase: a community-editable fluorescent protein database.* Nat Methods, 2019. **16**(4): p. 277-278.

[126] Rumyantsev, K.A., et al., *Development of Single-Domain near-Infrared Fluorescent Protein Gaf-Fp Based on Bacterial Phytochrome.* Tsitologiia, 2016. **58**(10): p. 744-54.

[127] Oliinyk, O.S., et al., *Smallest near-infrared fluorescent protein evolved from cyanobacteriochrome as versatile tag for spectral multiplexing.* Nature Communications, 2019. **10**(1): p. 279.

[128] Shcherbakova, D.M., et al., *Molecular Basis of Spectral Diversity in Near-Infrared Phytochrome-Based Fluorescent Proteins.* Chem Biol, 2015. **22**(11): p. 1540-1551.

[129] Piatkevich, K.D., F.V. Subach, and V.V. Verkhusha, *Far-red light photoactivatable near-infrared fluorescent proteins engineered from a bacterial phytochrome.* Nat Commun, 2013. **4**: p. 2153.

[130] Yao, J., et al., *Multiscale photoacoustic tomography using reversibly switchable bacterial phytochrome as a near-infrared photochromic probe.* Nature Methods, 2016. **13**(1): p. 67-73.

[131] Lychagov, V.V., et al., *Microfluidic System for In-Flow Reversible Photoswitching of Near-Infrared Fluorescent Proteins.* Anal Chem, 2016. **88**(23): p. 11821-11829.

[132] Zhang, J., R.J. Stankey, and R.D. Vierstra, *Structure-Guided Engineering of Plant Phytochrome B with Altered Photochemistry and Light Signaling* Plant Physiology, 2013. **161**(3): p. 1445-1457.

[133] Kamper, M., *Gerichtete Evolution und Charakterisierung von Bakteriophytochromen für die tiefrote, hochauflösende Fluoreszenzmikroskopie.* PhD Thesis, 2017.

[134] Burgie, E.S., et al., *Crystallographic and Electron Microscopic Analyses of a Bacterial Phytochrome Reveal Local and Global Rearrangements during Photoconversion.* Journal of Biological Chemistry, 2014. **289**(35): p. 24573-24587.

[135] Lehtivuori, H., et al., *Removal of Chromophore-Proximal Polar Atoms Decreases Water Content and Increases Fluorescence in a Near Infrared Phytofluor.* Front Mol Biosci, 2015. **2**: p. 65.

[136] Jensen, N.A., et al., *Reversibly Switchable Fluorescent Proteins for RESOLFT Nanoscopy*, in *Nanoscale Photonic Imaging*, T. Salditt, A. Egner, and D.R. Luke, Editors. 2020, Springer International Publishing: Cham. p. 241-261.

[137] Li, S.-S., et al., *Monitoring the Changes of pH in Lysosomes during Autophagy and Apoptosis by Plasmon Enhanced Raman Imaging.* Analytical Chemistry, 2019. **91**(13): p. 8398-8405.

[138] Geisow, M.J. and W.H. Evans, *pH in the endosome: Measurements during pinocytosis and receptor-mediated endocytosis.* Experimental Cell Research, 1984. **150**(1): p. 36-46.

[139] Feher, J., *2.10 - ATP Production II: The TCA Cycle and Oxidative Phosphorylation*, in *Quantitative Human Physiology*, J. Feher, Editor. 2012, Academic Press: Boston. p. 180-190.

[140] Ruhlandt, D., et al., *Absolute quantum yield measurements of fluorescent proteins using a plasmonic nanocavity.* Communications Biology, 2020. **3**(1): p. 627.

[141] Schneider, F., et al., *Quantum Yield Measurements of Fluorophores in Lipid Bilayers Using a Plasmonic Nanocavity.* The Journal of Physical Chemistry Letters, 2017. **8**(7): p. 1472-1475.

[142] Habenstein, F., *Engineering of NIR fluorescent protein for live-cell nanoscopy*. PhD Thesis, 2020.

[143] Ilgen, P., et al., *RESOLFT Nanoscopy of Fixed Cells Using a Z-Domain Based Fusion Protein for Labelling.* PLOS ONE, 2015. **10**(9): p. e0136233.

[144] Yu, D., et al., *An improved monomeric infrared fluorescent protein for neuronal and tumour brain imaging.* Nature Communications, 2014. **5**(1): p. 3626.

[145] Lenngren, N., et al., *Coordination of the biliverdin D-ring in bacteriophytochromes.* Physical Chemistry Chemical Physics, 2018. **20**(27): p. 18216-18225.

[146] Claesson, E., et al., *The primary structural photoresponse of phytochrome proteins captured by a femtosecond X-ray laser*. eLife, 2020. **9**: p. e53514.

[147] Yang, X., et al., *Temperature-scan cryocrystallography reveals reaction intermediates in bacteriophytochrome.* Nature, 2011. **479**(7373): p. 428-432.

[148] Burgie, E.S., J. Zhang, and Richard D. Vierstra, *Crystal Structure of Deinococcus Phytochrome in the Photoactivated State Reveals a Cascade of Structural Rearrangements during Photoconversion.* Structure, 2016. **24**(3): p. 448-457.

[149] Brakemann, T., et al., *A reversibly photoswitchable GFP-like protein with fluorescence excitation decoupled from switching.* Nature Biotechnology, 2011. **29**(10): p. 942-947.

[150] Lavoie-Cardinal, F., et al., *Two-Color RESOLFT Nanoscopy with Green and Red Fluorescent Photochromic Proteins.* ChemPhysChem, 2014. **15**(4): p. 655-663.

[151] Pennacchietti, F., et al., *Fast reversibly photoswitching red fluorescent proteins for live-cell RESOLFT nanoscopy.* Nature Methods, 2018. **15**(8): p. 601-604.

[152] Chang, H., et al., *A unique series of reversibly switchable fluorescent proteins with beneficial properties for various applications.* Proceedings of the National Academy of Sciences, 2012. **109**(12): p. 4455-4460.

[153] Tiwari, D.K., et al., *A fast- and positively photoswitchable fluorescent protein for ultralow-laser-power RESOLFT nanoscopy.* Nature Methods, 2015. **12**(6): p. 515-518.

[154] Widengren, J., R. Rigler, and Ü. Mets, *Triplet-state monitoring by fluorescence correlation spectroscopy.* Journal of Fluorescence, 1994. **4**(3): p. 255-258.

[155] Konen, T., *One-step RESOLFT with a positively switchable RSFP with improved deactivation kinetics.* PhD thesis, 2019.

[156] Konen, T., et al., *The Positive Switching Fluorescent Protein Padron2 Enables Live-Cell Reversible Saturable Optical Linear Fluorescence Transitions (RESOLFT) Nanoscopy without Sequential Illumination Steps.* ACS Nano, 2021. **15**(6): p. 9509-9521.

[157] Feyereisen, R., *Insect CYP Genes and P450 Enzymes ☆*, in *Reference Module in Life Sciences*. 2019, Elsevier.

[158] Filonov, G.S., et al., *Deep-Tissue Photoacoustic Tomography of a Genetically Encoded Near-Infrared Fluorescent Probe.* Angewandte Chemie International Edition, 2012. **51**(6): p. 1448-1451.

[159] Shcherbakova, D.M. and V.V. Verkhusha, *Near-infrared fluorescent proteins for multicolor in vivo imaging.* Nat Methods, 2013. **10**(8): p. 751-4.

[160] Tinevez, J.-Y., et al., *Chapter fifteen - A Quantitative Method for Measuring Phototoxicity of a Live Cell Imaging Microscope*, in *Methods in Enzymology*, P.M. Conn, Editor. 2012, Academic Press. p. 291-309.

[161] Carlton, P.M., et al., *Fast live simultaneous multiwavelength four-dimensional optical microscopy.* Proceedings of the National Academy of Sciences of the United States of America, 2010. **107**(37): p. 16016-16022.

[162] Zhou, L., et al., *Superresolution and pulse-chase imaging reveal the role of vesicle transport in polar growth of fungal cells.* Science Advances. **4**(1): p. e1701798.

[163] Zwetsloot, A.J., G. Tut, and A. Straube, *Measuring microtubule dynamics.* Essays Biochem, 2018. **62**(6): p. 725-735.

[164] Staiger, C.J., et al., *Actin filament dynamics are dominated by rapid growth and severing activity in the Arabidopsis cortical array.* Journal of Cell Biology, 2009. **184**(2): p. 269-280.

[165] Zhang, X., et al., *Highly photostable, reversibly photoswitchable fluorescent protein with high contrast ratio for live-cell superresolution microscopy.* Proceedings of the National Academy of Sciences, 2016. **113**(37): p. 10364-10369.

[166] Hoffman, E.A., et al., *Formaldehyde crosslinking: a tool for the study of chromatin complexes.* The Journal of biological chemistry, 2015. **290**(44): p. 26404-26411.

[167] Chmyrov, A., et al., *Nanoscopy with more than 100,000 'doughnuts'.* Nat Methods, 2013. **10**(8): p. 737-40.

[168] Jansen, I., *Development and characterization of novel reversibly switchable red fluorescent proteins with opposing switching modes.* PhD Thesis, 2019.

[169] Hermann, M., et al., *Binary recombinase systems for high-resolution conditional mutagenesis.* Nucleic Acids Res, 2014. **42**(6): p. 3894-907.

9 List of Abbreviations

RESOLFT	reversible saturable optical linear fluorescence transition
RSFP	reversibly switchable fluorescent protein
NIR	near infrared
PENELOPE	photostable nir reversibly switchable fluorescent protein
PMT	Photomultiplier tube
APD	Avalanche photodiode
VIS	Visible
UV	Ultraviolet
NADPH	nicotinamide adenine dinucleotide
PSF	Point spread function
NA	Numerical aperture
SIM	Structured illumination microscopy
SLM	Spatial light modulator
SMLM	Single molecule localization microscopy
STORM	stochastic optical reconstruction microscopy
(f)PALM	(fluorescence) photoactivated localization microscopy
FWHM	full width half maximum
MINFLUX	Minimal photon fluxes
STED	Stimulated emission depletion
ISC	Incoherent standing wave
GFP	Green fluorescent protein
FP	Fluorescent protein
PCM	Photosensory core module
PAS	Per arnt sim
GAF	cGMP phosphodiesterase adenylate cyclase/FhlA
PHY	Phytochrome-specific
BV	Biliverdin
CBD	Chromophore binding domain
Wi-Phy	Wisconsin Phytofluor
SNIFP	STED near infrared fluorescent protein
BpRSFP	Bacteriophytochrome-derived reversibly switchable fluorescent protein
PDB	Protein database
SDS	Sodium dodecyl sulfate
PAGE	Polyacrylamide gel electrophoresis
EC	Extinction coefficient
QY	Quantum yield
SEC	Size exclusion chromatography
PFA	Paraformaldehyde

10 Acknowledgements

Throughout working on this dissertation over the past four years, I have received amazing support and assistance, for which I am incredibly thankful. First, I want to thank Prof. Dr. Stefan Jakobs and Prof. Dr. Stefan Hell for the opportunity to work on my doctoral thesis in the amazing environment of Tower 2 of the Max-Planck-Institute for Biophysical Chemistry/Multidisciplinary Sciences. I would like to thank Prof. Dr. Stefan Jakobs for his supervision and support over the course of this work. I am grateful to Prof. Dr. Dirk Schwarzer and Prof. Dr. Jörg Enderlein for an encouraging atmosphere and very fruitful discussions during my Thesis Advisory Committee meetings. Furthermore, I would like to thank Prof. Dr. Alexander Egner, Dr. Melina Schuh and Dr. Sonja Lorenz as members of my examination board.

I would like to thank my collaborators Dr. Alexey Chizhik (Prof. Dr. Jörg Enderlein), Dr. Nicolas Foos (Prof. Dr. Martin Weik) and Cédric Mittleheiser (Dr. Michel Sliwa). Alexey for carrying out the fluorescence quantum yield measurements and fruitful discussion about the possible fluorescent state models. Nicolas for his work on generating crystal structures of PENELOPE. Martin for his great interest and passion for this collaboration and an amazing and honest discussion environment during our Zoom meetings. Cédric for generating amazing amounts of ultrafast spectroscopy data in just a few months of his PhD and being a great collaborator to work with. Michel for reaching out and supervising the general course of this project

I would like to speak out my deepest appreciation and thankfulness to all my friends and coworkers in the Nanobiophotonics department.

For excellent technical and emotional support in the lab and having lovely chats, I would like to thank Rita Schmitz-Salue, Ellen Rothermel, Marco Roose and Nicole Molitor. Furthermore, Tanja Gilat for excellent cell culture advise as well as for her always positive vibes and great humor, no matter if in the lab, cell culture or Deja. Also, thanks to Anne Folmeg for being a great addition to the biology team, taking care of my cells and talking about music and upcoming festivals. Cornelia Heistermann for the continuous supply with RFA plates (mostly on short notice from my side), while always being friendly, encouraging and nice to talk to. Jaydev Jethwa for knowing about/ fixing every screw you can find in Tower 2 and sharing his great experience about everything. Simon Piechota for his active maintenance of every switch, cable and bulb there is while still finding the time to talk about running. To Sarah Leondarakis, Stefanie Kruse and Susanne Fok Shan for not being annoyed by me for asking the same questions about shipping every 6 months and always being helpful with every organizational task I can think of. Also, for lifting everyone's spirits when bringing their dogs Ole and Racker.

To all current and former members of office 240. Adrian Przybylski for introducing me into programming and splines, while giving me the best possible start in Göttingen by also introducing me to all the sports teams I'm still a part of. Dr. Heydar Shojaei for interesting talks about everything that's going on in the world and sharing his experience about the science world. Béla Görtz for being a great addition to the office and always being happy to talk about sequencing data analysis, veganism, music and everything else.

To all students,PhDs and Post-Docs who joined in these demanding last two years. Daniel for always smiling and laughing, being a beast on the bike and reviving the journal club. Jannis Anstatt for a fantastic (and still ongoing) science meme battle, great humor and making the slow transition of overtaking my bench place as subtle as possible. Kateryna Yarova for her spreading of good vibes right next to my desk, having the most honest chats and trying to establish the phrase "what's poppin'" but also realizing that won't happen. Jan Niklas Dohrke for showing the greatest passion and joy for science (especially robots, PCRs and PENELOPE homology models I have ever witnessed, while also making amazing Pizza and having ruling on the beach court. Fredi for joining every event that has happened since her start and nice fun fact contributions in the coffee corner. Anna (Anni/Shredder) Wittek for having the most infectious smile, being great to talk about everything and feeling the same joy for puppy reels I do. Kaushik Imander for sharing the same passion for Marvel and Jurassic Park/World movies as I do and telling very convincing red wine origin stories. Lynn-Marie Ostersehlt for always being in a great mood, chats about how every fluorescent dye ever does not do what its supposed to do and joining/organizing most events when they were possible to be organized. Julius Peter Bernhardt for bringing back the Happy Hour, kickstarting the Tower 2 Beachvolleyball team and his profound knowledge in german comedy classics. Henrik van der Emde for an unexpected night out in a music rehearsal room. Carina Bäte for being the 2nd most ambitious intern I have ever seen, getting me back on the tennis court and having remarkable chats about every topic. Tiberiu (Tibby) Mihaila for being the most ambitious intern I have ever seen and sharing a great time at discussing morality or just playing basketball or singing karaoke. Georgij for his fantastic support at the Aekta and nice chats during barbecues or on the hallway.

To the people who kept me going from day 1. Stefan Jakobs for convincing me to come here, giving me a ride to the train station after my introduction talk and still holding on to me after I had some deadline problems in the beginning of my PhD. Stefan Stoldt for nice chats, excellent sarcasm and great support at the few times I used the live imaging facility. Michael for countless scientific discussions and help with laser adjustments and misaligned beam paths. Hannah for a lot of laughs, a relaxing holiday and the best Halloween costume of 2018. Till Stephan for nice chats about everything in the cell culture, fun night outs and dealing well with the fact that a Halloween party led to a lot of joy for others at our costs. Jonas for teaching me most of my now decent basketball skills. Jan-Erik for jointly complaining about the closed gym room during Covid, table tennis sessions and helping me align laser beam paths I touched. Kamila for discussing differences between Poland and

Germany and always being in a good mood. Mark for amazing FIFA games despite technical difficulties, great poker nights and exhausting squash games. Christian for pointing out new haircuts to everyone, sharing the obsession for sports, a great past holiday and holiday to come as well as giving great advice. Peter for great continuous emotional support, the one or other ride to the institute, nice but way too early morning runs and fantastic evenings on his balcony. Isabelle for the great advice that a PhD is a marathon, not a sprint. Timo for being the prototype of a researcher and data kraken, while being simultaneously a great and funny guy who was always encouraging me to keep going with bacteriophytochrome RSFPs. Without you, there would be no PENELOPE. Florian for instructing me how to properly use the NIR-STED/RESOLFT microscope, great companionship and talks, the towel story and excellent emotional support. Felix for asking the real questions, remembering where I live, the most amazing Kiosk nights I ever had and will have and great general advice and emotional support. Sarah for being as honest as supportive and encouraging, laughing about my bad jokes, pushing it to the limits in the lab and always being down for every event you can imagine. Axel for being the best worst person I know, sharing the joy of writing a thesis at (almost exactly) the same time, stupid jokes and pranks but also great support in every way. Chris for being a great office neighbor/ work husband, F1 buddy, host, Capybara connoisseur while still listening to all the complaints on Fridays that sum up over the week.

Particular attention to Team RESOLFT/RSFP/PENELOPE, consisting of Sylvia Löbermann, Dr. Jan Keller-Findeisen and Dr. Nickels Jensen. Sylvia for being the best bench neighbor I or anyone could wish for while also being the true cloning queen and being supportive with protein names, SEC's or just talking about everything. Nice. Jan for being a data magician, while also encouraging me to 'revive' RESOLFT. For always being in a good mood despite working on 1000 projects in parallel, being able to make talking about fluorescent state models fun and in summary for being a great guy in general. Last but definitely not least to Nickels (a.k.a Pater Nicki), for guiding me through these 4 years on the highest level in professional and personal terms. Talking about RSFPs and RESOLFT as well as Gin, movies and what makes a good person. All this while taking care of every machine, microscope running and coworker being in this group. You definitely made it to my Top10 (despite the tendency to yell from time to time).

For proofreading this thesis, I would like to thank Nickels, Jan, Chris, Lynn, Florian and Sylvia.

The same thankfulness and appreciation goes out to home and home home. To Rabea, Pauli and Hanna for being the best flatmates I could imagine, being always supportive, understanding and simply amazing. To Fabi, Tobi, Jana, Samuel, Tino, Mischa, Dominik, Carla, Carmen and Domi who never get tired of asking me how my glowing proteins are doing and managed every year to make it for THE visit to Göttingen. Last but not least to my mom, dad and brother. Thank you for always being supportive and encouraging to my (sometimes-odd) ideas for the last 28 years. .